MEDIUM RANGE ORDER IN HIGH ALUMINUM CONTENT AMORPHOUS ALLOYS MEASURED BY FLUCTUATION ELECTRON MICROSCOPY

By

William Gregory Stratton

A dissertation submitted in partial fulfillment
of the requirements for the degree of

Doctor of Philosophy

(Materials Science)

at the

UNIVERSITY OF WISCONSIN – MADISON

2007

To my wife Elisabeth

Acknowledgements

This work could not have been done alone. During my tenure as a graduate student, I had the opportunity to work with several encouraging, enlightening, and entertaining people. A big thanks to:

- The Perepezko Group at the University of Wisconsin, specifically Dr. John Perepezko, Seth Imhoff, and Joe Hamann for helpful discussions, nanocrystal counting statistics, DSC data, and providing me with high Al-content amorphous alloy samples.

- The Kelton Group at Washington University for high Al-content amorphous alloy samples and helpful discussions.

- Zhongyi Liu and Dean Miller for STEM support at Argonne National Laboratory.

- The Abelson Group at the University of Illinois, specifically Dr. John Abelson, Lakshminarayana Nittala, and Stephanie Bogle for STEM support and helpful discussions.

- Dr. Murray Gibson, Dr. Mike Treacy, and C.S. Webber for theoretical help with the development of the new FEM theory.

- The Materials Science Center staff; Alex Kvit, Rick Noll, Rich Casper, John Jacobs, and Don Savage for equipment training and support.

- Diana Rhoads for administrative support in the Materials Science Program. Whenever I had a question about the program, you always had an answer.

- My fellow Materials Science Program graduate students for being both supportive collaborators and friends.

- Members of the Voyles Group for always being ready to lend a hand and offer ideas.

- My thesis advisor, Paul Voyles. Thank you for your time, your enthusiasm, your humor, and your guidance. With your help, my time as a graduate student was more enlightening than I ever expected.

- Lastly, thank you to my wife Beth and my parents Ron and Gail for unwavering support and encouragement. I could not have accomplished this without your help.

This research was supported by the National Science Foundation under Grant DMR-0347746.

Abstract

High Al-content metallic amorphous alloys have an unusual devitrification behavior. Upon annealing, alloys made by a rapid quench develop a high density ($>10^{21}$ m^{-3}) of pure Al nanocrystals. These alloys show a steadily decreasing heat flow signal in isothermal calorimetry and a steadily decreasing nucleation rate, suggesting heterogeneous nucleation. This data implies that a high density of nanoscale structural precursor sites is needed to account for the large number of nucleation events.

One possible form of the precursor site in high Al-content amorphous alloys, and other amorphous materials, is atomic structure at the nanoscale (typically 1-3 nm), which is called medium-range order (MRO). This is to distinguish it from short-range order, typically first- and second-nearest neighbor atomic distances, and long-range order, typical of atomic spacing in crystals. MRO can be described as non-trivial three- or four-atom correlations or (in some cases) as small pockets of structural order in an otherwise disordered matrix. Fluctuation electron microscopy (FEM) is a quantitative electron microscopy technique that uses spatial fluctuations in diffraction from nanoscale volumes using the image variance to detect MRO in amorphous materials.

To aid in interpretation of FEM results, we developed a new phenomenological theory which uses the assumed structure of a nanocrystal / amorphous composite for various amorphous materials to explicitly calculate the image variance as a function of experimental parameters. This model therefore connects the FEM signal to well-defined aspects of the material's structure,

enabling us to make statements on how a different FEM results relate to changes in the sample structure of high Al content amorphous alloys.

FEM on multiple high Al-content metallic amorphous alloys ($Al_{92}Sm_8$, $Al_{88}Y_7Fe_5$, and $Al_{88}Y_7Fe_4Cu_1$) found Al-like MRO present in the as quenched state of these materials. Experiments on the deformation induced alloy $Al_{92}Sm_8$ found a different type of MRO, which implies that the Al-like MRO in the as quenched material is associated with the devitrification reaction of high Al-content amorphous alloys. Using our FEM theory, we determined that the crystal Al-like volume fraction increases 60% when $Al_{88}Y_7Fe_5$ is alloyed with Cu. This is correlated with a measured increase in the crystal volume fraction in $Al_{88}Y_7Fe_5$ and $Al_{88}Y_7Fe_4Cu_1$ upon devitrification.

Taken together, this work supports the quenched-in nuclei hypothesis for high Al-content amorphous alloy devitrification. In this picture, small proto-crystals are frozen into the material during the rapid quench process and later act as nucleation sites for the high density of Al nanocrystals that form upon devitrification. It is these proto-crystals that we measure with FEM. This is a crystal growth mechanism rather than a grain coarsening mechanism. As seen by the FEM results, these proto-crystals can be modified by alloying or processing to tailor the macroscale properties of the material.

Table of Contents

List of Figures

List of Tables

Chapter 1.

Introduction

Amorphous materials are materials without a well defined crystal lattice, meaning that these materials contain short range order (SRO), but not the long range order (LRO) typical of crystalline materials. Both organic and inorganic materials can be made amorphous. Organic amorphous materials include polystyrene, polymethylmetacrylate, and other polymers. Inorganic amorphous materials include amorphous semiconductors (e.g. Si), silicate glasses (e.g. SiO_2), and amorphous metals (e.g. $Al_{88}Y_7Fe_5$).

Structurally amorphous materials may also be glassy, in which case they undergo the glass transition at a temperature T_g. T_g can be defined many ways, but ultimately it is the temperature below which the glass ceases to flow like a liquid [1-4]. This can be measured thermodynamically using differential scanning calorimetry (DSC), physically by measuring the shear viscosity (an amorphous solid is considered to have a viscosity over 10^{12} Pa s) [1], or by measuring changes in physical properties like the specific heat or specific volume [1,5-8]. Representative examples of these measures can be seen in Figure 1.1. Table 1.1 gives T_g for

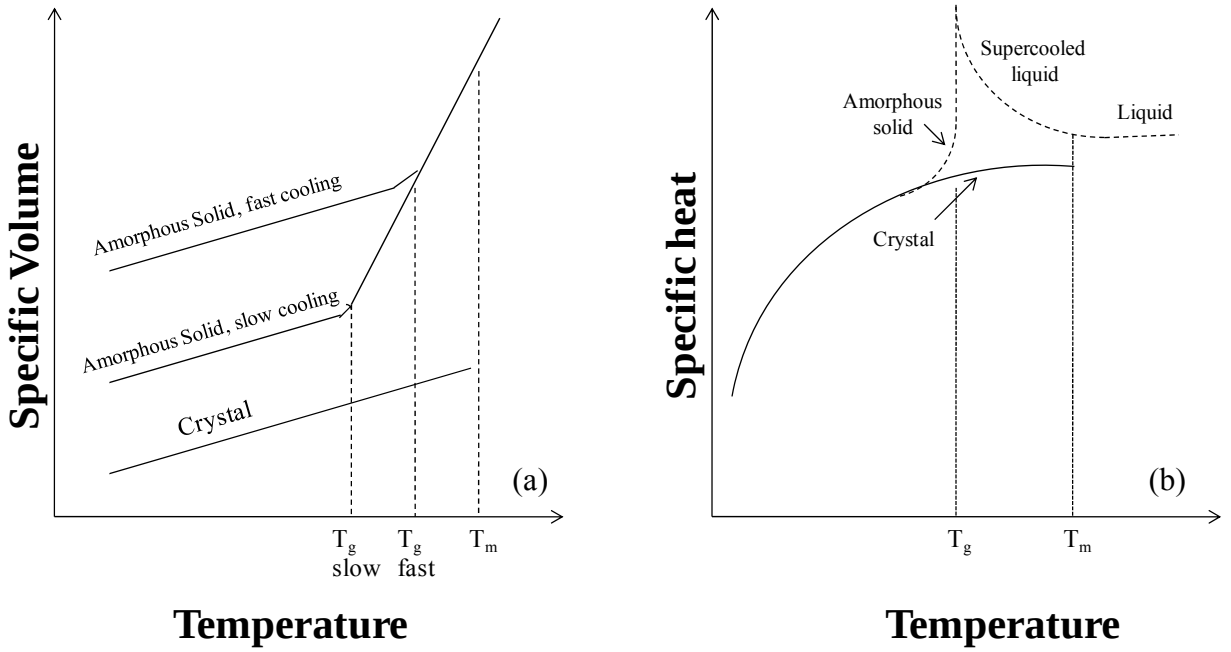

Figure 1.1: Schematic plots of physical changes associated with T_g. T_g depends on the cooling rate of the solid, with a faster cooling rate leading to a higher T_g than a slower cooling rate. The continuous change of the (a) specific volume (first derivative of the Gibbs free energy) and the discontinuous change of the (b) specific heat (second derivative of the Gibbs free energy) show that T_g is a second order phase transformation. Between the melting temperature T_m and T_g the amorphous material is a supercooled liquid, meaning it is below the melting point of the material but can still flow. Figures adapted from (a) [9] and (b) [10].

various organic and inorganic materials. T_g is not a fixed material property, as it can change with the cooling rate [9] or the thermal history of the material [11,12].

Material	Type	Tg (^{o}C)	Reference
Polystyrene	Polymer	100	Reference 4
Polycarbonate	Polymer	150	Reference 4
Amorphous Si	Semiconductor	1200	Reference 29
Amorphous Ge	Semiconductor	700	Reference 29
$Al_{92}Sm_8$	Amorphous metal - marginal	170	Reference 31
$Al_{88}Y_7Fe_5$	Amorphous metal - marginal	270	This work, Chapter 5
$Al_{88}Y_7Fe_4Cu_1$	Amorphous metal - marginal	220	This work, Chapter 5
$Zr_{59}Ti_3Ni_8Cu_{20}Al_{10}$	Amorphous metal - bulk	382	Reference 21
$Fe_{56}Co_7Ni_7Zr_{10}B_{20}$	Amorphous metal - bulk	541	Reference 14

Table 1.1 T_g for various organic and inorganic amorphous materials. The Al amorphous metals do not have a true T_g, the noted temperatures are the onset of primary crystallization.

1.01 Amorphous Metals

Amorphous metals [3,8,12-19] are disordered materials that contain mostly metallic elements (Al, Zr, Cu, etc.) along with other elements like rare earth (RE) or transition metal (TM) elements. The ability of these alloys to form an amorphous state is defined by the glass forming ability (GFA) of the compound. Turnbull suggested that for an alloy to have a high GFA the reduced glass transition temperature T_{rg}, which is the ratio of the glass transition temperature and the melting temperature ($T_{rg} = T_g/T_m$) should be equal or lager to 2/3 [20]. Other explanations for GFA have been also been proposed [21-23], although practically a good GFA refers to alloys that can be made easily in the lab at a low cooling rate without any crystallization.

Amorphous metals are divided into bulk metallic glasses (BMGs) and marginal glass formers. BMGs are alloys that require relatively low cooling rates (~ 10^2 K/s) to preserve the disordered structure [14,15]. Examples of BMGs are seen in Table 1.1, but the best known BMG is

probably the commercially available Vitreloy alloy ($Zr_{41.2}Ti_{13.8}Cu_{12.5}Ni_{10}Be_{22.5}$). Vitreloy is marketed as having excellent impact and wear mechanical properties along with high biocompatibility [24], so this material is used in sporting equipment, electronics casings, and bioimplants. Marginal glass formers do not form the amorphous structure so readily, so they require a much higher cooling rate than BMGs (~ 10^5 K/s) [25]. High Al and Fe-content amorphous alloys are examples of marginal glass formers. At this point the only commercially available marginal glass former is Metglass ($Fe_{80}B_{20}$) [26] a high Fe-content amorphous alloy, which is used in low-loss power distribution transformers because of its excellent magnetic properties [27,28].

Metals can be made amorphous either by nucleation control or growth control. Experimentally, calorimetry is typically used to tell the difference between these two mechanisms. Calorimetry measures the energy loss or gain associated with a phase transformation from a sample with temperature changes [6,29]. There are different types of calorimetry experiments. Isothermal calorimetry holds the temperature constant while measuring the energy change, thus measuring the energy difference measured as a function of time. DSC increases the temperature at a constant heating rate, therefore measuring the energy difference as a function of temperature. The DSC and isothermal calorimetry signal for growth controlled amorphous alloys are different than those for a nucleation controlled. Nucleation controlled amorphous alloys should show a distinct T_g below the onset of primary crystallization (T_x) in the DSC trace, and the isothermal trace should show an increasing and then decreasing signal indicating first the formation of nuclei (increase dH/dT), then their subsequent growth (decrease in dH/dT) [25,30]. Growth controlled amorphous alloys should not show a distinct T_g in

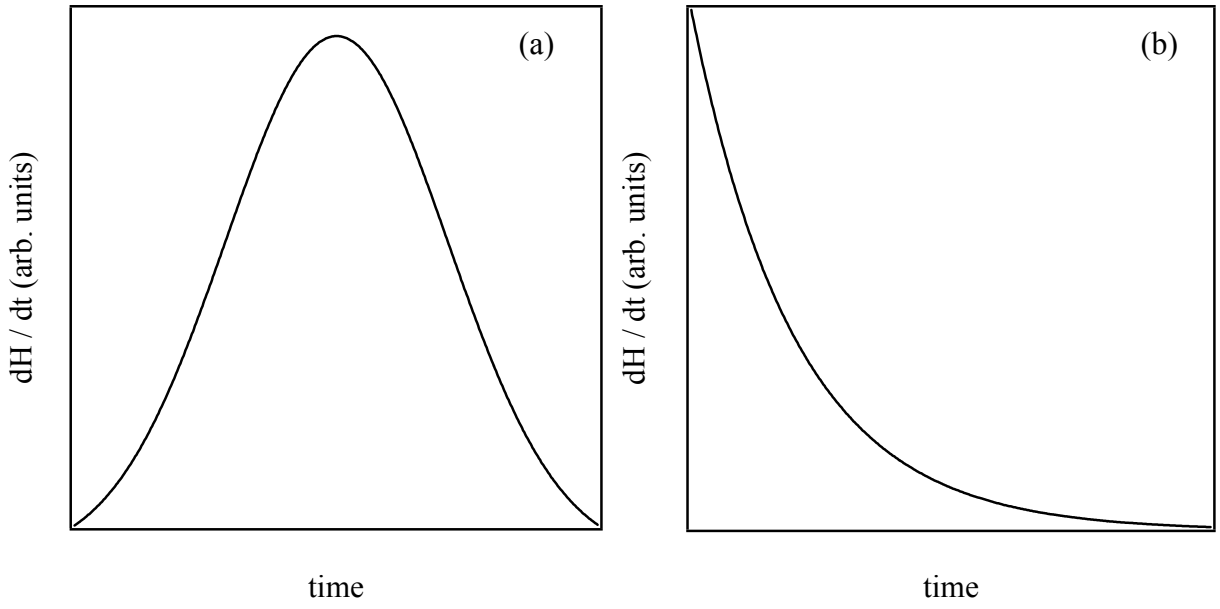

Figure 1.2 : Isothermal calorimetry traces for a nucleation (a) versus growth control glass (b). Since energy is first needed to form then grow nuclei in a nucleation controlled material, the isothermal signal first increases and decreases. Since nuclei already exist in a growth controlled material, the isothermal signal only decreases. Figure adapted from [30].

DSC, rather it will be at the same temperature as T_x [25]. Also, the isothermal trace will only show a steadily decreasing evolved heat, indicating that nuclei already existed in the material, and we are only seeing their subsequent growth [30]. A schematic isothermal calorimetry trace for these two mechanisms is seen in Figure 1.2.

To explain these differences in DSC and isothermal calorimetry results requires using a time-temperature-transition diagram (TTT). A TTT diagram plots the change in structure (e.g. nucleation onset) as a transformation curve on axes of time versus temperature. This

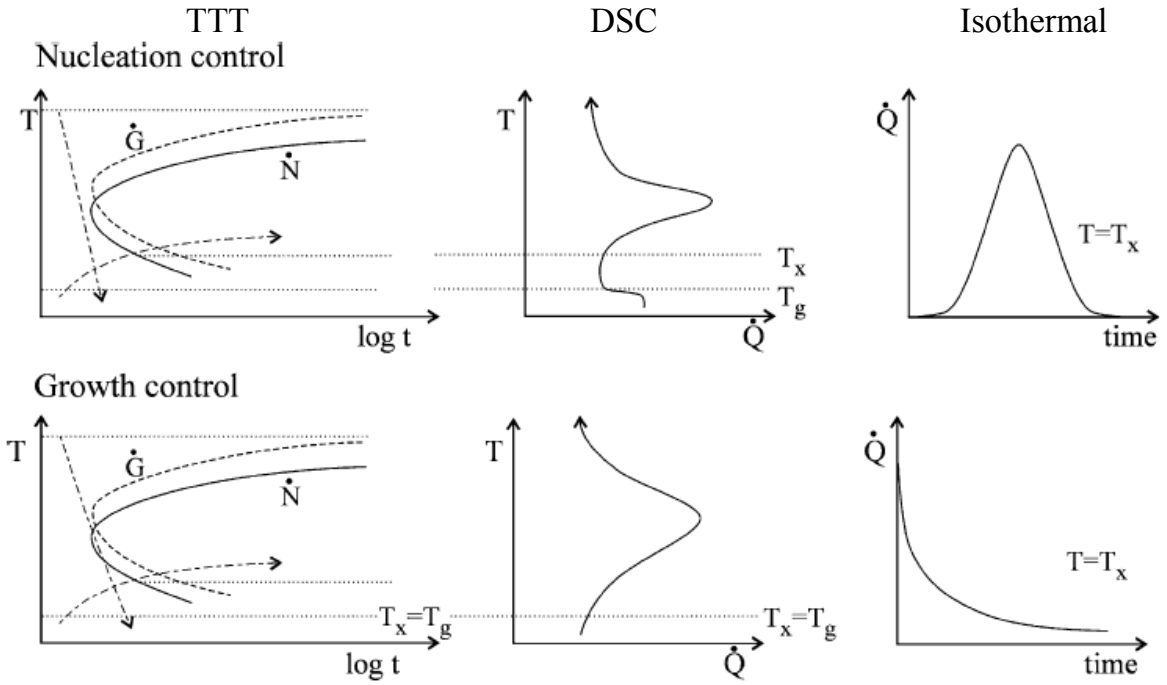

Figure 1.3: Representative TTT, DSC and isothermal calorimetry for nucleation control versus growth control. Nucleation control amorphous alloys will show a distinct T_g in DSC, while growth control amorphous alloys do not. Figure from [31].

transformation curve is nose shaped, with the fastest transformation kinetics occurring at the apex. Figure 1.3 compares representative TTT, DSC, and isothermal curves for a nucleation versus a growth controlled material [31]. When we form a rapidly quenched amorphous alloy, we are following a decreasing temperature versus time (cooling) contour line on the TTT diagram. If the cooling contour line does not intersect the transformation curve, the disordered liquid structure will be preserved in the solid state. This is because the material was quenched rapidly

enough to avoid any nucleation onset or crystal growth during solidification. Therefore, if heated, this sample would crystallize by homogeneous nucleation, since there were no phases formed during the quench to act as nucleation sites for crystal growth. The DSC would show a distinct T_g and the isothermal trace would first increase then decrease [25,30].

On the other hand, if the cooling contour did intersect the transformation contour, then a fraction of our quenched material would have undergone crystallization. These small proto-crystals, formed by the rapid quench, would not grow because of the rapidly rising viscosity of the material due to the high cooling rate [9,14,25]. Proto-crystals could then act as nucleation sites for crystal growth on post-quench annealing. The DSC would not show a distinct T_g and the isothermal calorimetry trace would be monotonically decreasing [25,30].

Based on DSC and isothermal calorimetry results, typically BMGs are nucleation controlled materials [14,15], while marginal glass formers are typically growth controlled amorphous materials [11,12,19,25,31-33]. Since marginal glass formers are growth controlled, this leads to a very special type of devitrification reaction which improves the mechanical properties of the material.

1.02 High Al-Content Amorphous Alloys

High Al-content amorphous alloys [16,34] are amorphous alloys that contain greater than 80 atomic percent Al. These amorphous alloys are marginal glass formers which require an RE element, a TM element, or both to solidify to an amorphous state [15]. The amorphous structure is metastable, with the eutectic concentration of the alloy usually having the highest glass forming

ability [35] because it results in the highest T_{rg} [20,35,36]. Probably the most attractive property of these amorphous alloys is their high tensile strengths [16,34] for their weight. Melt-spun ribbons of these alloys have tensile strengths approaching 1000 MPa [37], but this can easily increase to 1500 MPa [25] when the material is brought through partial crystallization and becomes a nanocrystal / amorphous composite. A similar phenomena is seen in Fe glasses (e.g. Metglass), where the devitrification reaction creates α-Fe nanocrystals resulting in excellent soft magnetic properties [17,26,28].

High Al-content amorphous alloys can be formed by rapid quenching (melt-spinning) [38] or by severe plastic deformation (cold-rolling) [19,39]. In melt-spinning a master ingot is melted and ejected under high pressure onto a cold wheel spinning at a high speed in an inert atmosphere, producing a thin ribbon of amorphous alloy at cooling rates up to 10^5 K/s. Cold-rolling is deformation by rolling and folding (> 100 times) of a multilayer sandwich of high purity metallic foils, increasing the total strain, defect density, and interfacial volume until an amorphous state is achieved [12,19,40]. The intense deformation process can also be accomplished by ball milling which makes an amorphous powder [41].

When annealed below T_g, high Al-content amorphous alloys exhibit an interesting devitrification behavior. Upon annealing of the rapidly quenched material, α-Al nanocrystals form at very high concentrations (> 10^{20} m^{-3}) in the amorphous material [12,19]. These nanocrystals form from the amorphous material with a higher solute concentration than the eutectic alloy [15], unlike the eutectic favored by other systems. During devitrification these nanocrystals quickly grow to tens of nm, and then stop growing due to an increase in the diffusion barrier for Al caused by the ejection of RE or TM from the nanocrystal into the amorphous matrix [12,19]. These

nanocrystals are thermally stable up to the point of full crystallization where the final microstructure usually becomes a mix of intermetallic phases [25].

The attractive mechanical properties achieved from the high density of nanocrystals formed from the rapidly quenched alloy leads to a key question: *what are these nucleation sites and how are they formed?* These alloys show a steadily decreasing heat flow signal in isothermal calorimetry [12,19,42] and a steadily decreasing nucleation rate [11], suggesting heterogeneous nucleation [43] and therefore devitrification via a growth controlled mechanism. So what are the nucleation sites? Classic heterogeneous nucleation sites are not present, as large impurity concentrations can be avoided with appropriate processing [44] and x-ray diffraction (XRD) experiments show no second-phase crystals. Therefore there must be a structural precursor to nanocrystal formation in the high Al-content amorphous alloys.

This structural precursor to crystallization has a processing dependence, as the high density of α-Al nanocrystals is unique to amorphous alloys made by rapid quenching [12]. When alloys of the same nominal bulk composition are made amorphous by a deformation induced mechanism (cold-rolling) devitrification does not proceed by primary Al-crystallization [12], rather little to no crystallization is observed. Furthermore, annealing experiments on the rapidly quenched material below T_g have found a thermal history dependence for the devitrification behavior [33]. Some high Al-content amorphous alloys devitrified after annealing treatments below T_g showed a decrease in both the nucleation and growth rate of Al crystallites, implying the as-quenched matrix undergoes a relaxation that exhausts catalytic nucleation [33].

In addition to having a thermal dependence, precursors to primary crystallization can also be influenced by small amounts ($\leq$ 1 atomic %) of microalloying elements. Substitution of 0.5%

Ti for Al [45] in $Al_{88}Y_7Fe_5$ has been shown to change the amorphous structure [46] and drastically reduce the number density of Al nanocrystals upon devitrification while increasing the onset temperature of primary crystallization. On the other hand, substitutions of 1% Cu for Ni in $Al_{88}N_7Sm_5$ [47] and 1% Cu for Al or Ni in $Al_{88}Y_4Ni_8$ [48] drastically increases the number of Al nanocrystals and decreases their size, while depressing the onset of primary crystallization. To exploit this primary crystallization reaction and the resulting favorable mechanical properties, we need to have a working understanding of the material and the precursors to crystallization.

1.03 High Al-Content Amorphous Alloy Nucleation Sites

Given that the nucleation sites for the high number of α-Al nanocrystals are some type of structural precursor to crystallization that cause the material to devitrify by growth only, there are two major hypotheses: quenched-in nuclei and grain coarsening. Perepezko proposes that the precursor of these nucleation events is quenched-in nuclei [19,42], or small subcritical nuclei quenched into the material from the metallic melt during the rapid quench process [19,42] causing the material to devitrify by a growth mechanism [19,25,30,31,33,42]. On the other hand, Xing *et al.* have taken the same heat flow studies and suggested that some high Al-content amorphous alloys are not glasses, but instead amorphous-nanocrystal composites, and that primary crystallization is grain coarsening, not a phase transition [45]. This stems from calculations showing that the volume fraction of quenched-in nuclei must be unrealistically high to obtain the final density of nanocrystals after devitrification [45].

The structural difference between these two hypotheses is how the crystalline volume fraction evolves with annealing. With quenched-in nuclei, the crystalline volume fraction increases through devitrification since each of the quenched-in nuclei grow by converting material from the amorphous matrix. If the material is a nanophase composite, the crystalline volume fraction should not change with devitrification since crystal growth is via grain coarsening.

Regardless of the mechanism occurring, because of the lack of visible precursor sites using conventional TEM or XRD, we know the size of these precursor sites are on the nanoscale (~1-3 nm in size). How to characterize these nanoscale precursor sites is nontrivial, as it requires a technique that can detect the important structure in an amorphous material which has eluded standard characterization techniques.

1.04 Structural Characterization Techniques for Amorphous Materials

When characterizing crystalline materials, we typically check the composition, crystal structure, defects, and other nanoscale features to help understand macroscale properties. The atomic structure of amorphous materials does not have the LRO of a crystal, making the interpretation of the structure difficult. This brings the question, what part of the amorphous structure should we pay attention to? More specifically for high Al-content amorphous alloys, what part of the amorphous structure influences the devitrification reaction?

Most of our structural information about amorphous materials comes from diffraction experiments, which yield a PDF [36,49]. The PDF, linked to the structure factor by a Fourier

transform, gives the number of atoms that sit a distance *r* away from the average atom in the sample weighted by the scattering factor. For a crystalline material each atom is locked into a lattice site so, ignoring defects and thermal effects, the PDF would show an appropriate number of neighbors at the relative lattice spacings. In polyatomic materials the PDF still gives the average atomic neighbor distances, but not the type of atoms separated by those distances. The partial pair distribution functions (PPDFs) help determine what atomic species are present at each neighbor distance within an amorphous material. The number of PPDFs in an amorphous material increases with the number of atomic components; a binary atomic system has three PPDFs, a ternary atomic system has six PPDFs, and so on. For example the three PPDFs in a binary atomic system AB can be described as: A-A, B-B, and A-B. These PPDFs are obtained by comparing PDF magnitudes from different scattering experiments (electron, neutron, x-ray, or resonant x-ray), since the PDF magnitude from the scattering experiment is dependent on the interaction between each atomic species and the radiation. Therefore, determining the PPDFs of a system requires the same number of unique scattering experiments as PPDFs [1,50].

Due to the large number of experiments required, few PPDFs for metallic glass systems have been determined. PPDFs for $Al_{75}Cu_{15}V_{10}$ [51], along with $Al_{56}Si_{30}Mn_{14}$ [52] and $Al_{77.5}Mn_{22.5}$ [52], show that Al-TM bond is shortened compared to the sum of metallic radii, indicating some non-metallic character to the bond [51-56], which may hinder the crystallization process. If this strong Al-TM chemical affinity is not present, each atomic species forms a structure similar to what is observed with their elementally pure amorphous state [52]. Though differences in detected amorphous material bond lengths compared to crystalline bond lengths could be due to the techniques used to deconvolve overlapping peaks in the PDF experiments [57].

Structures for various metallic glasses have been proposed based on results from diffraction experiments. Using the PDF from amorphous metals [58-60] along with reverse Monte Carlo simulations [61-63], several researchers found icosahedral SRO present in the amorphous structure. Specifically, Cervinka [64] proposed icosahedral clustering in a $Ti_{61}Cu_{16}Ni_{23}$ glass. This structure consists of five pasted icosahedra build of 49 atoms. Miracle and Senkov [57] proposed four efficient packing atomic clusters that might exist randomly throughout the amorphous matrix of Al-Y and Al-Y-Ni glasses [57].

Yet these diffraction results only give information on nearest neighbors and do not reach an intermediate range length scale of 1-3 nm [65-67]. This is a problem given that the interesting features responsible for the devitrification behavior of the high Al-content amorphous alloys are within this intermediate range. To stress the importance for structural information in amorphous materials at this length scale, there is significant and growing evidence that atomic structure at a length scale of 1-3 nm, influences electronic properties [68], vibrational modes [69], plastic deformation [70,71], and crystallization reactions [40] in amorphous materials.

In amorphous materials, atomic structure at the nanoscale of this range (1-3 nm) is called medium-range order (MRO). MRO sits between SRO, typically first- and second-nearest neighbors, and LRO, typical of crystals. MRO can be described as non-trivial three- or four-atom correlations, g_3 and g_4 respectively, [72] or (in some cases) as small pockets of structural order in an otherwise disordered matrix. Although MRO includes physical structure below the length scale that yields Bragg peaks in the structure factor, but beyond the length scale that produces peaks in the PDF [73], so there are many possible physical representations of MRO beyond the pockets of order definition.

1.05 Fluctuation Electron Microscopy

FEM uses spatial fluctuations in diffraction from nanoscale volumes to detect MRO in amorphous materials [66,74] using a TEM or STEM. In amorphous materials, homogeneous atomic structure means homogeneously random or maximally disordered and heterogeneous means more ordered. If the structure is homogeneous, the spatial fluctuations in diffraction will be small. If the structure is heterogeneous, the spatial fluctuations in diffraction will be large. At the other extreme of order, a homogeneous single crystal will show essentially zero fluctuations. To date, FEM has shown fundamentally new medium-range structure information in several different amorphous systems. Initially FEM was used to study amorphous semiconductors [72,73,75], but recently it has been used to study amorphous oxides [76,77], amorphous carbon films [78], and amorphous metals [40,79].

FEM is done by systematically varying k to find conditions that excite Bragg-like diffraction from regions with ordered atomic structure. The diffracted intensity from an ordered region scales as the square of the number of atoms in the region, leading to a particularly bright spot in the image. If the beam falls between strong diffracting conditions, the ordered regions will be particularly dark. All of the images, however, consist of speckle - random patterns of black and white dots, the intensity and position of which change with k - so a quantitative measurement of "bright" and "dark" is required. In order to distinguish meaningful MRO from random structural fluctuations, Treacy and Gibson [74] defined the normalized image variance,

$$V(k,Q) = \frac{\left\langle I^2(\mathbf{r},k,Q)\right\rangle - \left\langle I(\mathbf{r},k,Q)\right\rangle^2}{\left\langle I(\mathbf{r},k,Q)\right\rangle^2}, \quad (1.1)$$

where $I(\mathbf{r}, k, Q)$ is the diffracted intensity as a function of position $\mathbf{r}$ on the sample, scattering vector magnitude k, and the resolution of the experiment $R = 0.61 / Q$. Q is the radius of the objective aperture in reciprocal space. The brackets $\langle\rangle$ indicate averaging over $\mathbf{r}$. Qualitatively, $V(k, Q)$ is a measure of the structural heterogeneity of the sample at the length scale of the resolution R: if the sample structure is homogeneous, V will be small. If it is heterogeneous, V will be large. If V is large for some k, there must be some pseudo-planar arrangements of atoms causing diffraction in the direction defined by k, and those pseudo-planes must have spatial extent limited to 1-3 nm. Formally, V, through $\langle I^2\rangle$, is connected to the three- and four-body atom position distribution functions [80]. Figure 1.4 shows that $V(k)$ measures the degree of speckle in dark-field images: the dark-field image at $k = 0.45$ Å^{-1}, the peak in the $V(k)$, has more speckle (brighter bright features and darker dark features) than the image at the minimum of $V(k)$, at $k = 0.60$ Å^{-1}.

$V(k)$ gives information on the type and degree of MRO based on the peak location and magnitude respectively [66]. Since changes in V with k come from changes in diffraction from ordered regions, the peak position tells us about the pseudo-interplanar spacings within those regions, and since the intensity of the diffraction depends on the region's size, the magnitude of $V(k)$ peaks tells us something about their size and density. Other factors, including orientational anisotropy and non-spherical regions can also influence $V(k)$ [81].

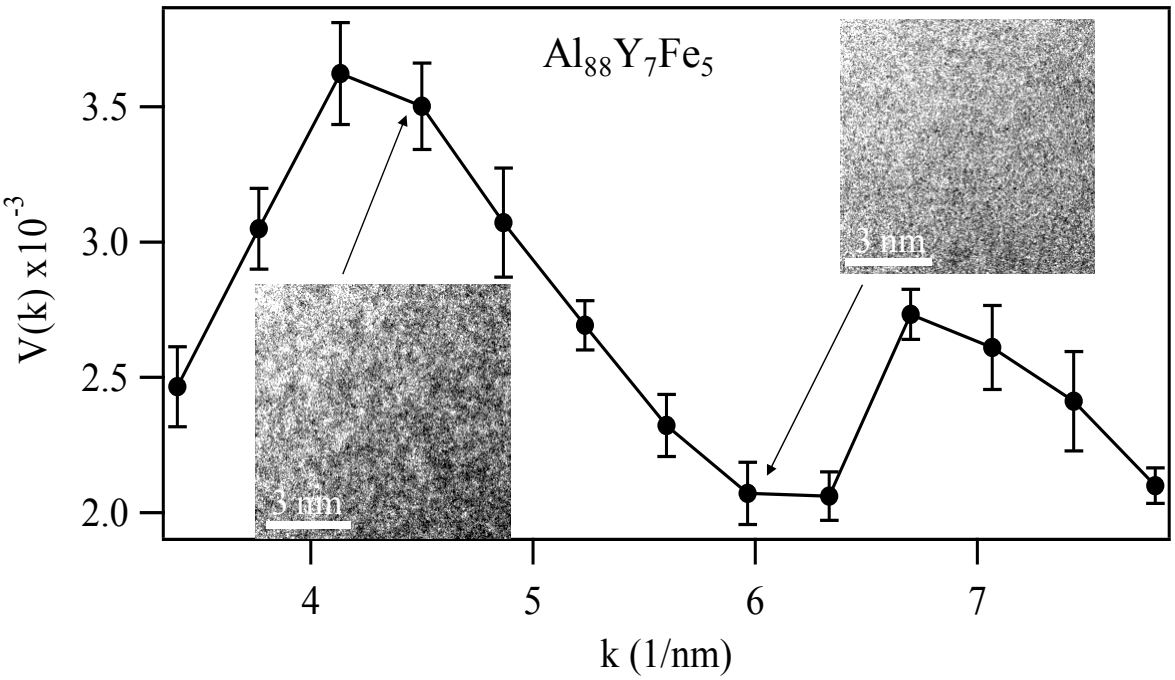

Figure 1.4: $V(k)$ with representative images. Higher V with more speckled images means more MRO compared to images with fewer speckles.

The speckle size is the minimum feature size in the micrograph, so the speckle size is also the spatial resolution of the images. The speckle size is the length scale at which we measure spatial fluctuations in diffraction, so the speckle size is also the length at which we probe MRO in a particular FEM experiment. That length should be chosen to match the length-scale of the MRO. If the resolution is too large, it will depress the signal to noise ratio of the MRO diffraction compared to diffraction from the disordered background, giving a lower $V(k)$. If the resolution is too small, it will again depress the signal to noise ratio by emphasizing random structural fluctuations, giving a smaller and noisier $V(k)$. Practically, a spatial resolution

of 1-3 nm is readily achievable in most electron microscopes and corresponds to third- and fourth- atomic neighbor distances in inorganic materials, a typical length scale for MRO.

The FEM technique can be done experimentally with variable coherence or variable resolution [80]. To perform variable coherence (VC) FEM [74], we hold the resolution R of the experiment constant (0.61 / Q in a TEM) while varying the magnitude of the dark field scattering vector k. This is the type of experiment preformed for the data in Figure 1.4. Variable resolution (VR) FEM [67] on the other hand is done by holding k constant and varying R.

VC FEM is typically done in a TEM with a fixed Q in hollow-cone dark field mode. We vary k by increasing the width of the hollow cone. Real space images at varying k are used to calculate V. VR FEM is typically done in a STEM given the ease in changing the resolution via the probe size [67]. In this case we use nanodiffraction images at varying R to calculate V. Although, either microscope can be used to perform VC or VR FEM as seen in Figure 1.5, since these two modes are formally identical by the reciprocity theorem as applied to electron imaging [82,83]. Although experimentally identical, FEM on a TEM (TEM FEM) and FEM on a STEM (STEM FEM) usually results in different absolute magnitudes for V.

1.06 Results from TEM FEM versus STEM FEM

This section contains material published as
Stratton, W. G. & Voyles, P. M., J. Phys: Cond. Mat. ***19*** *(2007).*

When comparing data from identical samples gathered by STEM FEM versus TEM FEM, peaks in V are usually preserved yet TEM FEM V are typically an order of magnitude less

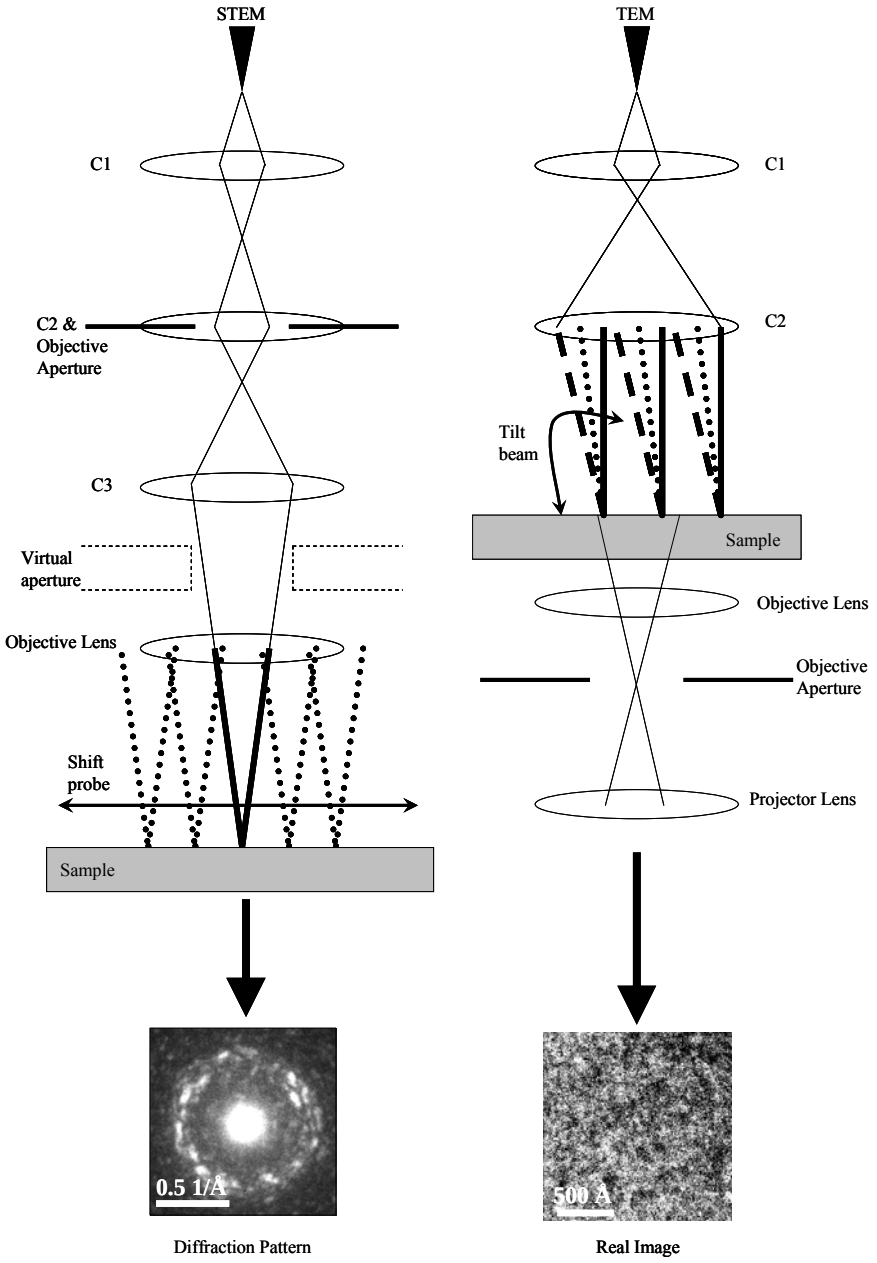

Figure 1.5: Schematic difference between STEM FEM and TEM FEM. STEM FEM with a STEM translates the probe to acquire multiple nanodiffraction patterns while TEM FEM with a TEM tilts the beam to obtain a real space image. TEM FEM with usually covers multiple more sample area in the *V* calculation compared to STEM FEM. Figure from [84].

than the STEM FEM V [66,67,84]. This is seen in Figure 1.6. Furthermore, simulated FEM data has a similar absolute V as STEM FEM, which is still higher than TEM FEM. This difference is caused by the coherence of the imaging mode for each microscope.

STEM experiments require a coherent electron beam for the acquisition of data. Likewise, all computer simulations are done with a simulated coherent electron beam [40,81,85]. Yet, TEM FEM experiments are done on a TEM with a small objective aperture size Q, and a large convergence angle. For our past experiments [40,86,87] with a LEO 912 EFTEM at 120 kV we use a 0.6 mrad objective aperture and a 4 mrad convergence angle. This configuration in a TEM creates a partially coherent imaging mode [83].

The partially coherent imaging mode will not be as sensitive to spatial fluctuations in the sample as a coherent beam. If the imaging mode is not fully coherent, not all of the MRO in the sample at or near a Bragg condition will generate coherent diffraction. This artificially decreases $V(k)$ by some coherency factor, regardless of k. Since the difference is instrumental rather than structural, it explains why peak locations and relative heights are conserved between TEM FEM and STEM FEM while the absolute V is orders of magnitude different. To create a more coherent imaging mode in the TEM, one only needs to run at a lower convergence angle while keeping the objective aperture size small. This is not usually done, as it will drastically increase the time required to acquire a FEM series, which can be particularly detrimental by causing beam induced crystallization when working with beam sensitive materials.

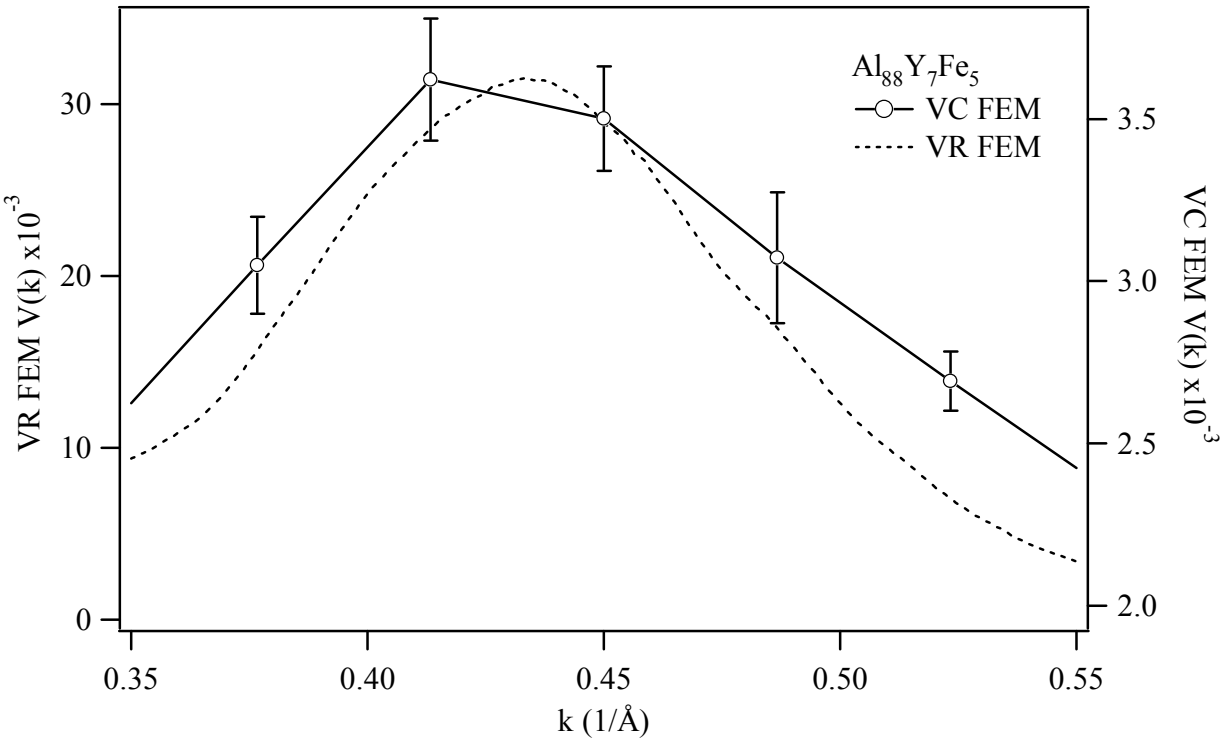

Figure 1.6: $V(k)$ for $Al_{88}Y_7Fe_5$ by TEM and STEM FEM. TEM FEM was at 1.6 nm spatial resolution; STEM FEM was at 2.8 nm spatial resolution. While the peak position is conserved between the techniques, STEM FEM has values of V that are ten times those of TEM FEM. TEM data was acquired at the University of Wisconsin – Madison while STEM data was acquired at Argonne National Labs with the aid of Dr. Liu. Figure modified from [84].

1.07 Summary

Amorphous materials, including amorphous metals, have different material properties than their crystalline counterparts. High Al-content amorphous metallic alloys demonstrate

interesting behavior upon devitrification, in which a high density of pure Al nanocrystals is formed at densities of 10^{20} m^{-3}. Processing, microalloying, and calorimetry experiments point to the presence of structural precursors in the medium-range structure to crystallization formed during the rapid quench process.

Detecting the nanoscale structures like these precursors within these materials is difficult. Standard XRD (and the PDF) is insensitive to structure at this medium-range length scale. FEM is a quantitative electron microscopy technique that measures spatial heterogeneities in amorphous materials to detect the type and degree of MRO present. We will use FEM to detect MRO associated with the devitrification reaction in multiple high Al-content amorphous metals, and use a new theory to help interpret this FEM data.

Chapter 2.

FEM Theory

This chapter contains material submitted for publication as
W.G. Stratton and P.M. Voyles, Ultramicroscopy, accepted for publication

While V is useful in determining the type and degree of MRO in a specimen, extracting quantitative information about the MRO size or density in amorphous samples has proven difficult. Treacy and Gibson [74] and later Gibson, Treacy, and Voyles [80] developed a theory of FEM which connected $V(k, Q)$ to the samples' three- and four- body atom position correlation functions, g_3 and g_4 respectively. These functions hold more subtle, longer length-scale information about the amorphous structure than the two-body correlation function g_2 that is measured by conventional diffraction, explaining why $V(k, Q)$ is sensitive to MRO. By assuming g_4 exhibits a Gaussian decay with a decay length Λ, Gibson et al. [80] arrived at the expression

$$V\left(k,Q\right)=\frac{\Lambda^3 Q^2}{1+4\pi^2 Q^2\Lambda^2}P\left(k\right). \qquad (2.1).$$

Λ is a characteristic ordering length scale of the sample, which can be extracted from the slope of a line of Q^2 / V versus Q^2, and all the other details of the structure are subsumed into $P(k)$ [80]. Equation (2.1) is reasonably well-followed by simulated diffraction from molecular dynamics models of amorphous silicon [80] .

Unfortunately, interpreting Λ and $P(k)$ in terms of specific sample structure remains challenging. Is Λ a particle size? What role does the density of MRO structural motifs play? $P(k)$ contains information about pseudo-planer spacings, but how do those "planes" interact with changes in Λ? Without a clear physical understanding of g_3 and g_4, interpretation of FEM results has rested primarily on simulation [40,72,81], like much of the other work on amorphous materials.

Finally, to use this theory to extract Λ requires systematically varying Q done with VR FEM, usually involving a STEM [66,67,80]. The majority of FEM data gathered to date has been VC FEM using a TEM at fixed resolution [40,72,75,77,86,88-91] which creates a need for a FEM theory that will extract more information about the sample structure from VC FEM data.

2.01 New Phenomenological FEM Theory

In this section we take the approach of explicitly assuming an easily parameterized sample structure, then working out $V(k, R)$ as a function of those parameters. Current work with computer simulations [40,81], amorphous semiconductors [73,75,92-94], $Ge_2Sb_2Te_5$ thin films [95], and my work in amorphous metal alloys [40,86,91] (discussed in detail in Chapters 4 and 5) point to an "amorphous" structure consisting of small pockets of crystal-like order in an otherwise

disordered matrix. We therefore calculate V for a nanocrystal / amorphous composite as a function of nanocrystal size, nanocrystal volume fraction, the thickness of our specimen, and the parameters of the FEM measurement k and R. Compared to the previous work, this theory is less general, but makes more specific connections between V and well-understood aspects of the sample structure.

2.02 Sample Geometry

We assume that the sample is a composite made up of an amorphous matrix with nanocrystals, analogous to MRO, randomly distributed throughout. The number and size of these crystals is defined by the crystalline volume fraction of the sample, Φ, and the diameter of each crystal, d. We assume the crystals are all spherical and the same size. This is an idealization of the paracrystalline Si structural model [72,88,92-94], in that the crystals are perfect, not strained. Because we idealize ht MRO as perfect crystals, the structure factor of this sample geometry will show crystalline peaks for larger crystals. Yet, within the constraints of this model of dilute and small nanocrystals, this will not strongly influence results from this analysis.

As shown in Figure 2.1, the sample has dimensions l x l x t set by the size of micrographs in FEM experiments, l x l, and the thickness of TEM samples, t. We further divide the sample into columns with dimensions of R x R x t. Within the column approximation [96], each column is independent and has lateral dimensions of the resolution of the experiment, R. Each column is

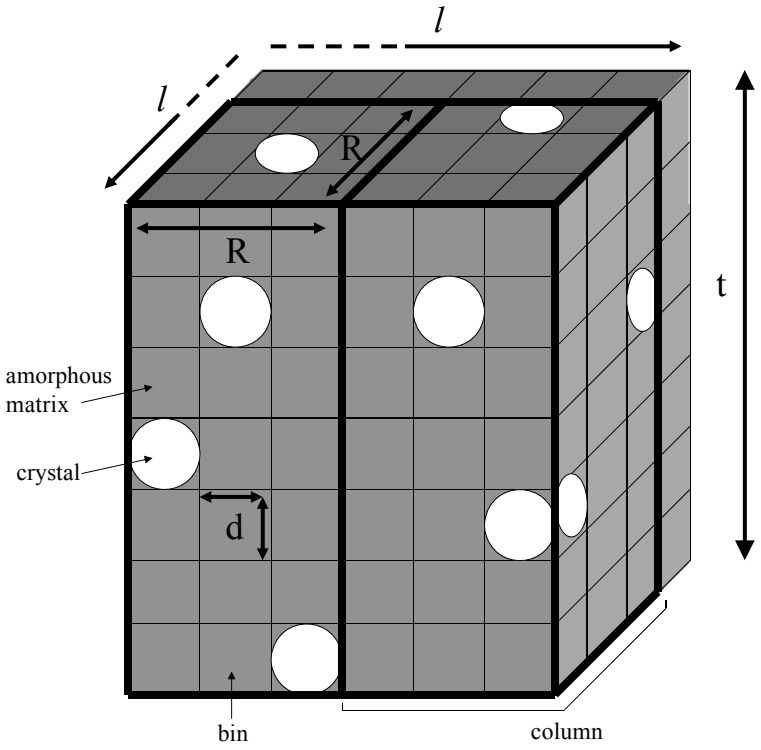

Figure 2.1: Sample definition for FEM theory. The sample has dimensions of *l* x *l* x *t*. The sample is broken into columns with the dimensions *R* x *R* x *t*, which are further divided into bins of dimensions *d* x *d* x *d*. Crystals of diameter *d* are randomly distributed throughout the sample, with each bin able to hold only a single crystal. Figure from [87].

further divided into crystal-size bins with dimensions *d* x *d* x *d*. Due to these dimensions, this theory will only be valid when $d < R$. $N_c = l^2/R^2$ is the number of columns in the image and $N_b = R^2 t/d^3$ is the number of bins per column.

2.03 Calculation of the Diffracted Intensity

The derivation of V proceeds as follows: first, we consider the intensity from a single bin, which may or may not contain one crystal. Then we sum over the bins in a column to obtain the intensity from that column, I_i, which involves the projection through the samples thickness. Next, we sum over I_i's to obtain $\langle I \rangle$ and $\langle I^2 \rangle$. We shall see that these last two sums depend mainly on the distribution of crystals in the bins, which we will assume is random. $\langle I \rangle$ and $\langle I^2 \rangle$ are defined as

$$\langle I \rangle \equiv \frac{1}{N_c} \sum_{i=1}^{N_c} I_i \text{ , and} \tag{2.2}$$

$$\langle I^2 \rangle \equiv \frac{1}{N_c} \sum_{i=1}^{N_c} I_i^2 \text{ .} \tag{2.3}$$

The intensity from a bin can be calculated from a modified intensity equation for the dark-field TEM image intensity from an arbitrary set of atoms in an monoatomic system derived previously [74],

$$I(\mathbf{k}) = \gamma \sum_{j}^{N_{atoms}} \sum_{l}^{N_{atoms}} A_{jl}(Q) \exp\left\{-2\pi i \left(\mathbf{k} \cdot \mathbf{r}_{jl}\right)\right\}, \tag{2.4}$$

$$\gamma \equiv \lambda^2 f^2(\mathbf{k}).$$

A_{jl} is the Airy function evaluated at r_{jl}, Q is the radius of the objective aperture in reciprocal space, $\mathbf{r}_{jl}$ is the distance between atoms j and l, λ is the wavelength of the imaging electron, and $\mathbf{k}$ is the dark field scattering vector. The intensity prefactor γ is a function of the atomic scattering factor $f(\mathbf{k})$ for a monoatomic system. The intensity expression for a polyatomic system would have the atomic scattering factors inside the sums, not in γ. $I(\mathbf{k})$ in equation (2.4) is unitless.

For a crystal oriented to a Bragg condition, the double sum of j and l scales as the number of atoms in the crystalline planes squared, which we define as D^2, making equation (2.4) $I(k) \approx \gamma D^2$. For spherical nanocrystals, $D = \pi d^3 \rho / 6$, where ρ is the atom volume density of the crystal.

Whether or not a bin contains a crystal, each bin will also have some structurally random amorphous matrix. Amorphous regions have no crystallographic planes; therefore we assume the intensity from amorphous regions scales as the number of atoms, not the number of atoms squared. This approximation is strictly true only for atoms in a gas, so we are assuming a matrix that is more disordered than in reality. A bin without a crystal therefore has an intensity $I_i = \gamma W$, where $W = d^3 \rho$ is the number of atoms in the bin. When a bin contains a crystal the background intensity is $\gamma(W - D)$. These definitions make the intensity from for a single bin

$$I_{bin} = \begin{cases} \gamma\left(D^2 + W - D\right) & \text{if the bin contains a crystal} \\ \gamma W & \text{if the bin does not contain a crystal.} \end{cases} \tag{2.5}$$

For simplicity, we will not write out the functional dependencies of D and W.

Next we assume that the scattering from different crystals through the thickness of the sample is incoherent, so it adds as intensities, not amplitudes. This is reasonable, especially for hollow-cone dark-field FEM, given that the vertical extent of the coherence volume for hollow-cone FEM is ~1 nm [97,98], which is similar to the crystal size and less than the probable distance between crystals at low to moderate volume fraction. The possibility of coherent effects between laterally adjacent crystals we simply neglect. Under this assumption, the intensity from column i depends only on the number of crystals, c_i, and the number of bins in a column, N_b. Substituting (2.5) into (2.2) and (2.3) gives

$$\langle I \rangle = \frac{1}{N_c} \sum_{i=1}^{N_c} \gamma \left(D(D-1) c_i + N_b W \right) \tag{2.6}$$

$$\langle I^2 \rangle = \frac{1}{N_c} \sum_{i=1}^{N_c} \left[\gamma \left(D(D-1) c_i + N_b W \right) \right]^2 , \tag{2.7}$$

where only c_i depends on i. If we define

$$\langle c \rangle = \frac{1}{N_c} \sum_{i=1}^{N_c} c_i \text{ , and} \tag{2.8}$$

$$\langle c^2 \rangle = \frac{1}{N_c} \sum_{i=1}^{N_c} c_i^2 \tag{2.9}$$

analogously to $\langle I \rangle$ and $\langle I^2 \rangle$, then

$$\langle I \rangle = \gamma \left[D(D-1) \langle c \rangle + N_b W \right] \text{, and} \tag{2.10}$$

$$\langle I^2 \rangle = \gamma^2 \left[D^2 (D-1)^2 \langle c^2 \rangle + 2D(D-1) \langle c \rangle N_b W + N_b^2 W^2 \right]. \tag{2.11}$$

2.04 Crystal Distribution and Expectation Values

To evaluate $\langle c \rangle$ and $\langle c^2 \rangle$, we assume that the crystals are randomly distributed on the discrete lattice of bins: each bin may have either one or zero crystals with constant probability P. P is set by Φ and d,

$$P = \frac{d^3 \Phi}{\pi / 6 \, d^3} = \frac{6\Phi}{\pi} . \tag{2.12}$$

We must avoid cases that give more crystals than bins, leading to $P > 1$, which means that the maximum possible Φ is one crystal for each box, $\Phi_{ult} = \pi / 6$. Under these assumptions, the

number of crystals in a column will follow the binomial distribution, $B(v)$, for v crystals in N_b bins [99], which is

$$B(v) = \frac{N_b!}{v!(N_b - v)!} P^v \left(1 - P\right)^{N_b - v}. \tag{2.13}$$

If the number of columns N_c, is large, $\langle c \rangle$ and $\langle c^2 \rangle$ can be evaluated by sums over the binomial distribution as

$$\left\langle c \right\rangle \approx \sum_{c_i=1}^{N_b} c_i \cdot B\left(c_i\right) \tag{2.14}$$

$$\left\langle c^2 \right\rangle \approx \sum_{c_i=1}^{N_b} c_i^2 \cdot B\left(c_i\right). \tag{2.15}$$

The expectation values of the binomial distribution can be computed numerically from (2.14) and (2.15), but when N_b is large and P has an intermediate value, the binomial distribution tends to a Gaussian distribution with a mean μ, and a standard deviation σ^2 [99],

$$\mu = nP = \frac{6R^2 \Phi t}{\pi d^3}, \tag{2.16}$$

$$\sigma^2 = nP\left(1 - P\right) = \frac{6R^2 \Phi t}{\pi d^3}\left(1 - \frac{6\Phi}{\pi}\right). \tag{2.17}$$

The expectation values for a Gaussian equivalent to (2.14) and (2.15) are [99],

$$\left\langle c \right\rangle = \int cP\left(c\right) dc = \mu, \tag{2.18}$$

$$\left\langle c^2 \right\rangle = \int c^2 P\left(c\right) dc = \mu^2 + \sigma^2. \tag{2.19}$$

The Gaussian approximation to the binomial distribution breaks down when the number of trials (N_b in our case) is small or when P is near 0 or 1, so it is only valid over a restricted range of Φ. Figure 2.2 shows a comparison between the binomial distribution and the

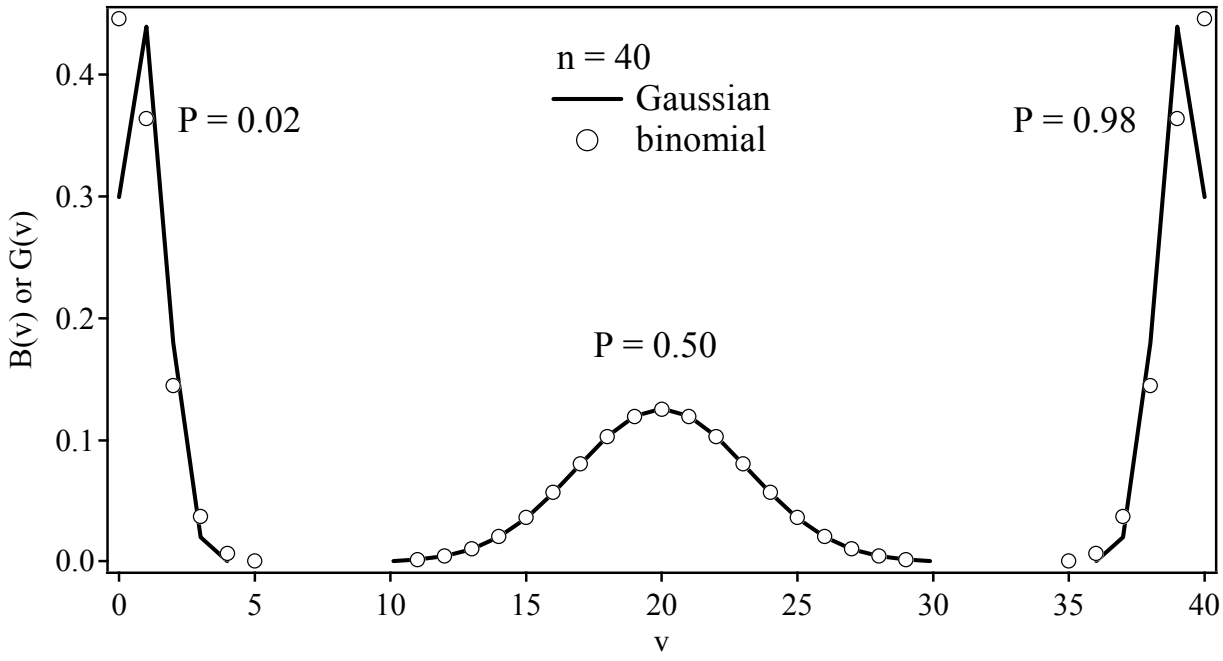

Figure 2.2 : Comparison of Gaussian approximation to binomial distribution. For *n* trials = 40 (similar to N_b in our theory), the Gaussian approximation is almost identical to the probability away from $P = 0$ and 1. Near $P = 0$ or 1, the deviation becomes large, showing why we need to set limits on Φ (related to P) in our theory. Figure from [87].

associated Gaussian approximation. The number of trials similar to our experiment (typically $N_b = 40$) is high enough, but we need minimum and maximum thresholds on Φ that keep P away from 0 and 1. Φ_{min} is set by the probability of finding zero crystals in a column, $B(0)$ below some threshold value Z_{min} (usually 10%). Φ_{max} is set by the probability of finding 1 crystal in every bin in the column, $B(N_b)$ below some threshold value Z_{max} (again usually 10%):

$$\Phi_{\min} = \frac{\pi}{6}\left(1 - Z_{\min}^{\frac{d^3}{R^2 t}}\right). \qquad (2.20)$$

$$\Phi_{\max} = \frac{\pi}{6} Z_{\max}^{\frac{d^3}{R^2 t}}. \tag{2.21}$$

As seen in Figure 2.2, within these limits Equations (2.18) and (2.19) are a good approximation to (2.14) and (2.15). Substituting Equations (2.18) and (2.19) into Equations (2.10) and (2.11) gives

$$\langle I \rangle = \gamma \left[D(D-1)\mu + N_b W \right] \tag{2.22}$$

$$\langle I^2 \rangle = \gamma^2 \left[D^2 (D-1)^2 (\mu^2 + \sigma^2) + 2D(D-1)\mu N_b W + N_b^2 W^2 \right]. \tag{2.23}$$

2.05 Fraction of Randomly-Oriented Crystals Near a Bragg Condition

The approximation in Equation (2.5) that the intensity from a crystal is proportional to the number of atoms squared implicitly assumes that **k** is fixed at a Bragg condition for the crystal. Therefore, if the crystals are randomly oriented, not all of the material's Φ ought to be included in the intensity calculation, since not all of the crystals will satisfy a given Bragg condition. We define the Bragg active fraction, A_{hkl}, as the fraction of crystals oriented so that there is strong diffraction into a particular family of reflections {hkl}, set by |**k**|. We follow the calculation of A_{hkl} by Freeman *et al.* [100], who considered this problem in the context of calculating the visibility of catalyst nanoparticles in a dark-field image.

A_{hkl} depends on the half angle $\Delta\theta$ through which a crystal can be rotated away from the exact Bragg condition but retain strong diffraction. Figure 2.3 shows the two types of contributions to $\Delta\theta$ in reciprocal space. One type is instrumental: the illumination convergence half angle α makes the Ewald sphere into a shell of finite thickness, and the objective aperture

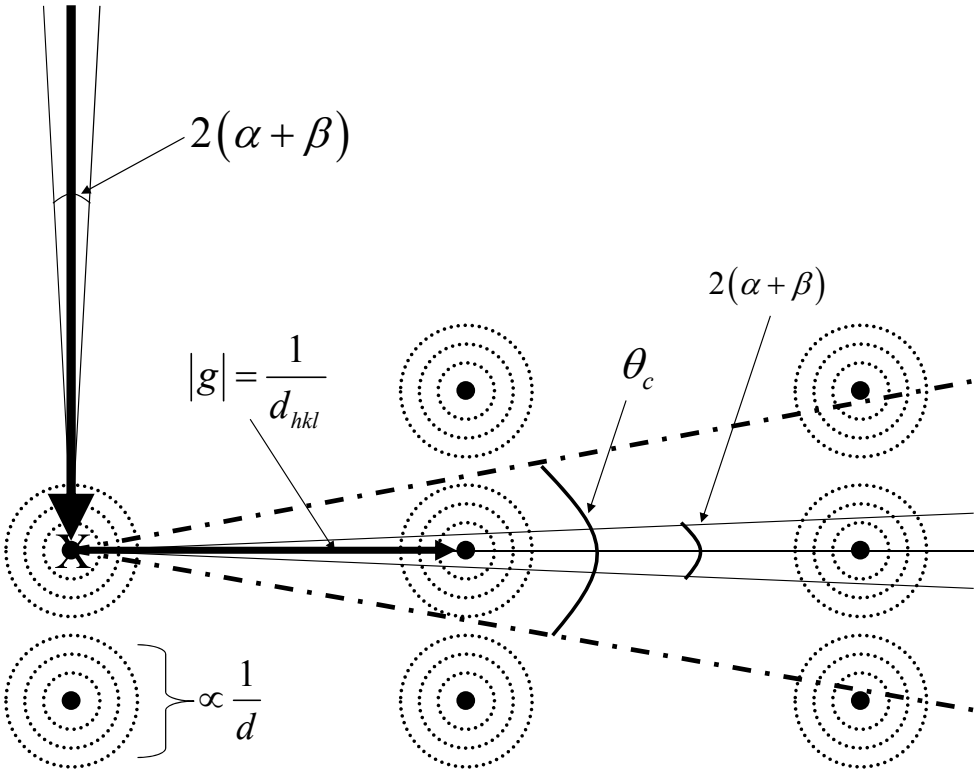

Figure 2.3: Reciprocal space representation of the contributions to $\Delta\theta$. α and β are the illumination convergence half angle and the objective aperture half angle respectively. θ_c is the acceptance angle of the Ewald sphere with the shape function of the lattice points which is proportional to $1/d$. θ_c is the dominant factor in the Bragg active function calculation. Figure from [87].

accepts rays with a half angle $\beta = Q\lambda$ with respect to the optic axis, effectively increasing the Ewald shell thickness. The second contribution comes from the small size of the nanocrystals. For a finite crystal, each reciprocal lattice point is replaced by a shape function, which for a spherical crystal is a series of concentric shells. The width of the first shell is $\sim 1/d$. For a

reciprocal lattice point $1/d_{hkl}$ away from the origin, where d_{hkl} is the plane spacing for $\{hkl\}$, the crystal can be rotated through an angle $\theta_c \approx d_{hkl}/d$ and still have the shape function in contact with the Ewald sphere. The total acceptance angle is just the sum of these contributions, $\Delta\theta = \theta_c + 2(\alpha + \beta)$ [100]. For our VC-FEM experiments on a TEM $\alpha = 4 \times 10^{-3}$ radians and $\beta = 6 \times 10^{-4}$ radians. For $d = 1$ nm and the {111} reflection of Al, $\theta_c = 0.2$ radians, so θ_c dominates $\Delta\theta$ and we will neglect α and β where convenient.

A_{hkl} also depends on the multiplicity and geometry of a family of reflections {hkl}. For a given reflection (hkl), the incoming beam directions that satisfy the Bragg condition will map out half of a great circle on the unit sphere; the corresponding $\left(\bar{h}\,\bar{k}\,\bar{l}\right)$ reflection maps out the other half. $\Delta\theta$ gives this great circle width, making it a "great ribbon". A_{hkl} is then the fraction of the unit sphere and surface area covered by all the ribbons from an {hkl} family. Figure 2.4 shows an example of A_{111} for a cubic crystal and $d = 2.0$ nm. The number of ribbons is the multiplicity of a family of planes, M_{hkl}, divided by two, and the fraction of the surface area occupied by the ribbons is approximately

$$A_{hkl} = \frac{2\pi\Delta\theta\left(M_{hkl}/2\right)}{4\pi} = \frac{1}{4} M_{hkl}\Delta\theta\,, \tag{2.24}$$

following Freeman *et al.* [100].

This is an overestimate for A_{hkl}, since it assumes that the great ribbons are flat and that there are no intersections of the great ribbons on the unit sphere. These approximations are acceptable when the width of the ribbons is small, but fail as they grow larger. We have also calculated A_{hkl} numerically including these effects, and compare the results as a function of $\Delta\theta$ to

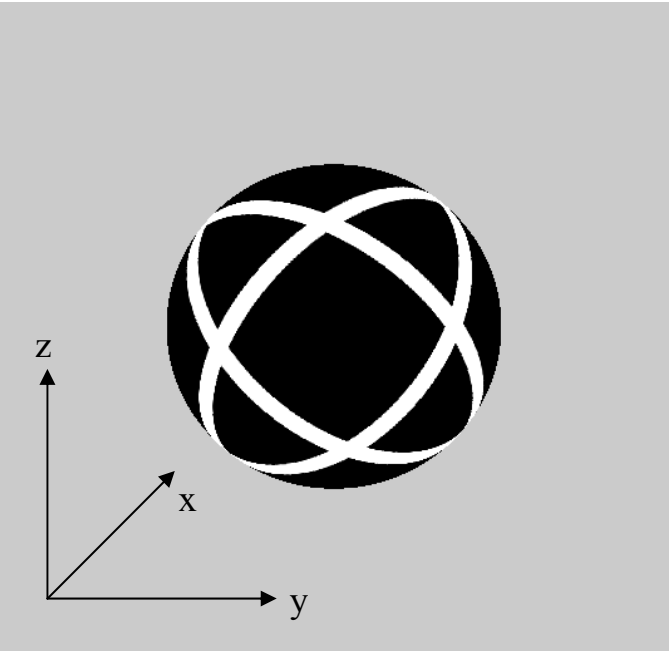

Figure 2.4: The unit sphere representation of A_{hkl} for an Al crystal for: a 1.0 nm (a) 3.0 nm (b) at a {111} reflection and a 1.0 nm (c) and 3.0 nm (d) at a {220} reflection. The great circle ribbons (shown in white) correspond to intersections with the respective planes, and their width is $\Delta\theta$. As seen, smaller crystals will have thicker great circle ribbons and therefore larger A_{hkl} values. Figure from [87].

Equation (2.24) in Figure 2.5 for different families of reflections of a cubic crystal. The discrepancy only becomes significant for $\Delta\theta > 0.15$ radians, which occurs only for the smallest crystals we consider ($d \sim 1$ nm).

Though the shape function, A_{hkl} is a function of one of our sample parameters d. To highlight this dependence, we introduce the Bragg active fraction constant, C_{hkl}. Since, for small

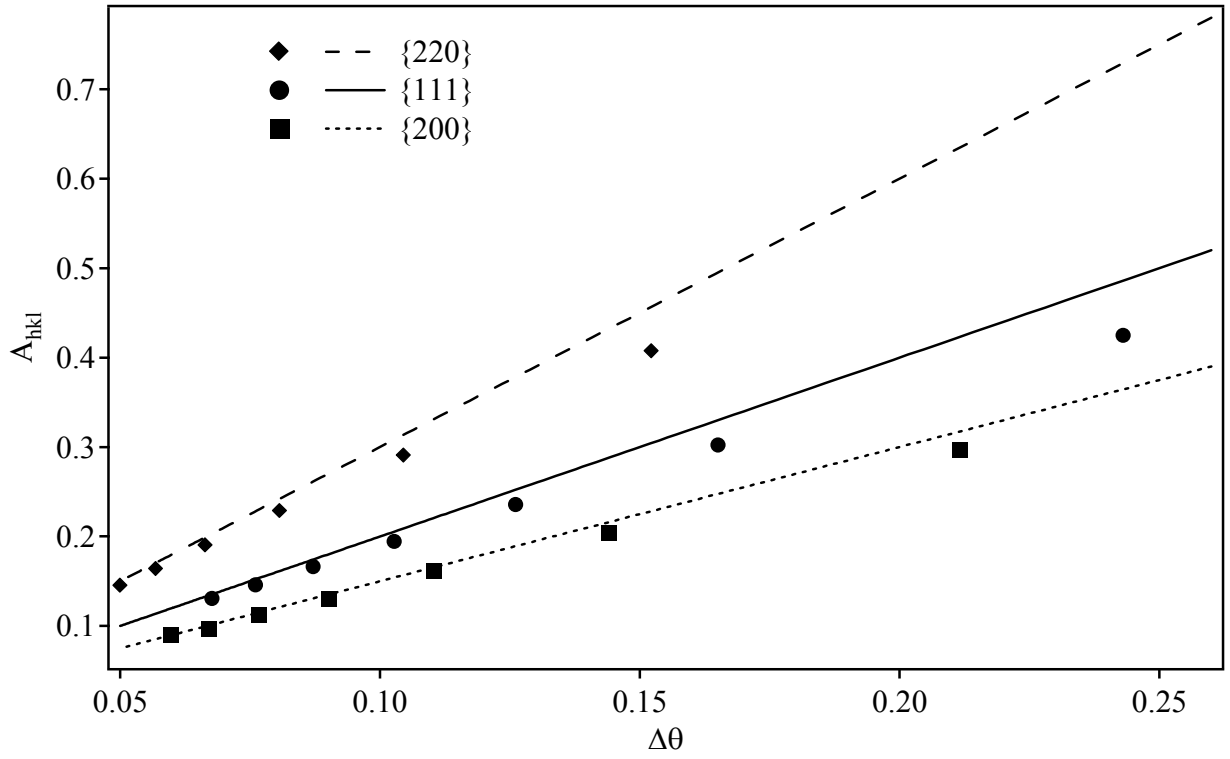

Figure 2.5: A_{hkl} versus $\Delta\theta$ for Al. Solid lines are Equation and the points are numerical results. Figure from [87].

crystals, the dominating factor of the $\Delta\theta$ calculation is the (d_{hkl} / d) term, we set $\Delta\theta \equiv d_{hkl} / d$. Therefore, the definition of A_{hkl} becomes

$$A_{hkl} \approx \frac{M_{hkl} d_{hkl}}{4d} = \frac{C_{hkl}}{d} \quad . \tag{2.25}$$

Correcting our previous expressions to include the Bragg active fraction effect like Equation (2.5) simply requires replacing Φ by $C_{hkl}\Phi / d$ everywhere. C_{hkl} is then the only place

in the calculation where **k** dependence is retained, which restricts the theory to treating only **k**'s that are crystal reflections.

2.06 Analytical Form of the Variance

Using the intensity expressions in Equations (2.22) and (2.23), Equation (1.1) for the variance becomes

$$V = \frac{D^2 \left(D-1\right)^2 \sigma^2}{\left[D\left(D-1\right)\mu + N_b W\right]^2}. \tag{2.26}$$

The intensity prefactor γ (which depends on the atomic scattering factor) has canceled, which would not happen for a polyatomic system. In terms of our sample parameters d, ρ, Φ, t, C_{hkl}, and the experimental resolution R, V is

$$V = \frac{\left(\frac{\pi}{6}\right) d^2 C_{hkl} \Phi \left(\frac{\pi}{6} d^3 \rho - 1\right)^2 \left(1 - \frac{6 C_{hkl} \Phi}{\pi d}\right)}{R^2 t \left[\frac{C_{hkl} \Phi}{d}\left(\frac{\pi}{6} d^3 \rho - 1\right) + 1\right]^2}. \tag{2.27}$$

The **k** dependence has been largely lost with the assumption that we are dealing only with Bragg scattering; different Bragg conditions can be compared by their C_{hkl}'s. C_{hkl} is dependent on the family of planes being measured and it can make V different for different reflections at fixed Φ and d. Therefore, in some cases, this change in of C_{hkl} with different families of planes provides insight into the relative peak heights in V at different scattering vectors.

Equation (2.27) only applies over a certain regime of its parameter space. The volume fraction of crystals must be between our limits of Φ_{min} and Φ_{max} for the Gaussian approximation of the expectation values of crystals to remain true, although it can be extended to $\Phi = 0$ to Φ_{ult}

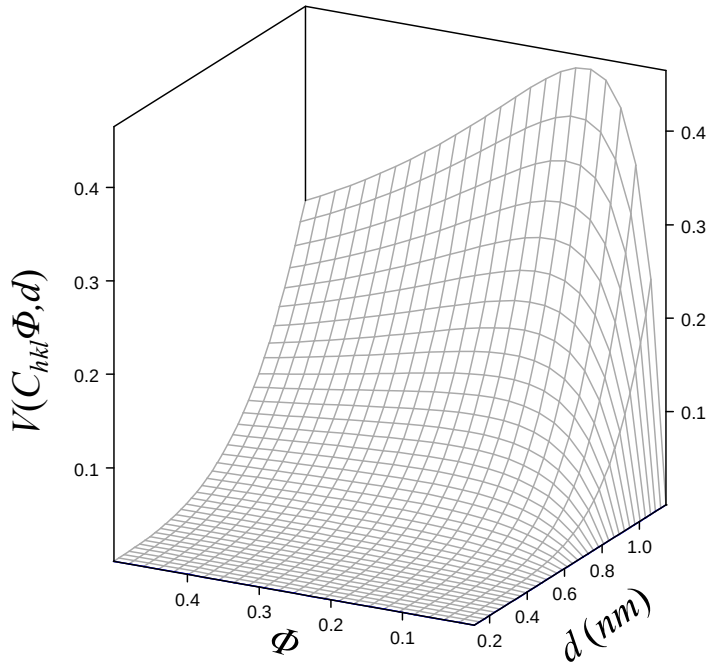

Figure 2.6: $V(d, C_{hkl}\Phi)$ using the binomial distribution. At low values of d and large values of Φ we show no values of V, because $\Phi > \Phi_{ult}$. Figure from [87].

by numerically evaluating $\langle c_i \rangle$ and $\langle c_i^2 \rangle$ from Equations (2.14) and (2.15) using the binomial distribution. The size of the crystal, d, must be less than the resolution of the experiment, R, or our expression for the number of diffracting atoms in the crystal, D, is incorrect. Lastly, the volume fraction of crystals must be less than Φ_{ult} to prevent the probability of finding a crystal within a bin from becoming greater than one.

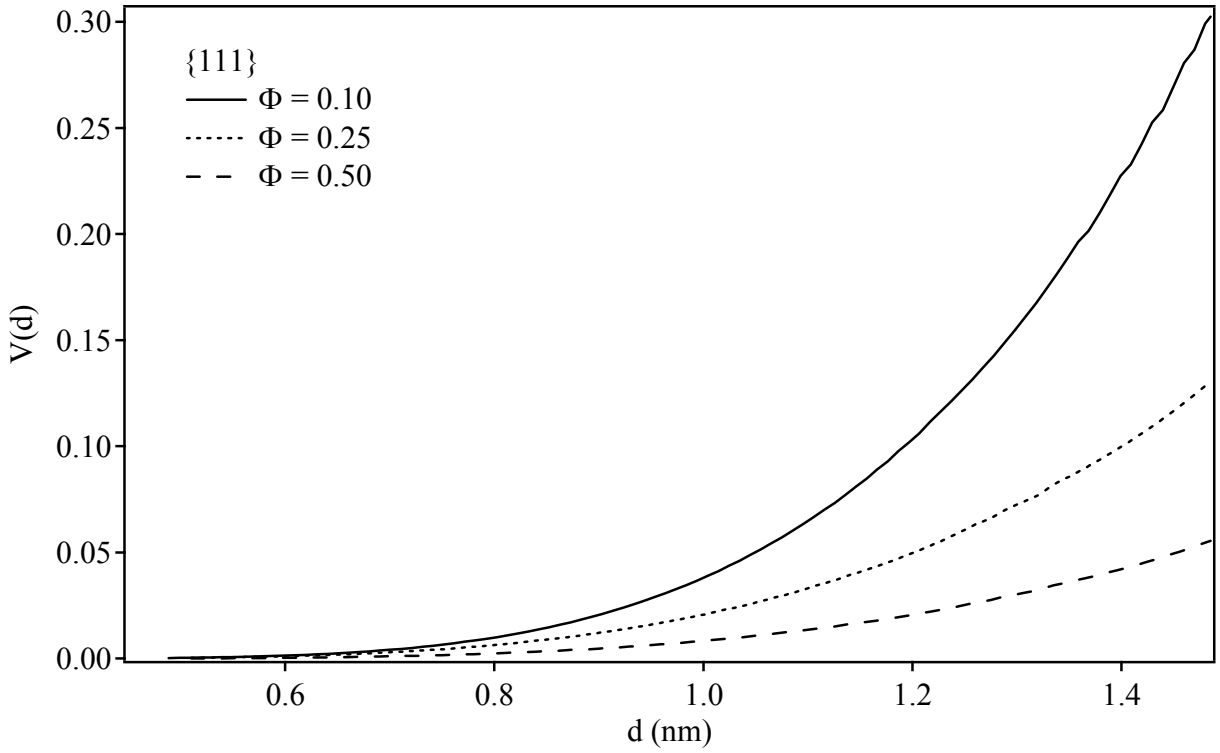

Figure 2.7: $V(d)$ at varying values of Φ for Al {111}. Generally, at a fixed Φ, as d increases, so does V. The other parameters are, R = 1.5 nm, ρ = 60 atoms/nm^3 and t = 40 nm. Figure from [87].

2.07 Discussion of the New FEM Theory

Figure 2.6 shows $V(d, C_{111}\Phi)$, calculated using the binomial distribution so $\Phi_{min} = 0$ and $\Phi_{max} = \Phi_{ult}$. Physical Φ is on the x-axis of the figure, yet since only a fraction of those crystals will be active at the {111} reflection we use $C_{111}\Phi$ in the variance calculation on the z-axis. We used parameters similar to our experimental values for amorphous Al-based alloy samples [40]: ρ of 60 atoms/nm^3 (Al atomic density), t of 40 nm, and R of 1.5 nm. Figure 2.7 shows $V(d)$ at

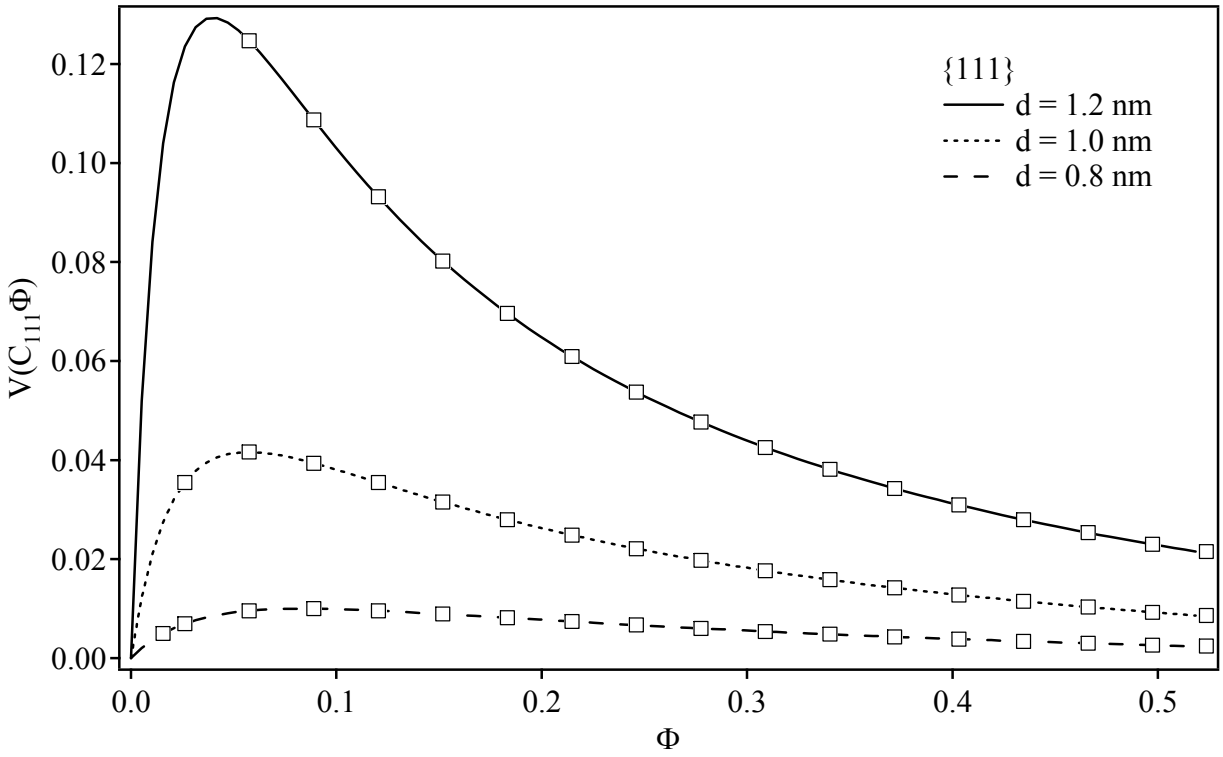

Figure 2.8: $V(\Phi)$ at varying values of d at the Al {111}. The lines represent the binomial calculated values, and the points are the Gaussian approximation. The Gaussian approximation is in good agreement with the binomial calculations within its range of applicability. However, that range does not include the maximum in $V(\Phi)$ for large d. The other parameters are, R = 1.5 nm, $\rho = 60\ ^{atoms}/_{nm^3}$ and t = 40 nm. Figure from [87].

fixed Φ, calculated with the binomial method. V increases monotonically with d, which is reasonable, since the intensity from each crystal is proportional to d^6, so at fixed Φ, larger crystals mean higher crystal scattering compared to the background, and larger fluctuations in diffraction.

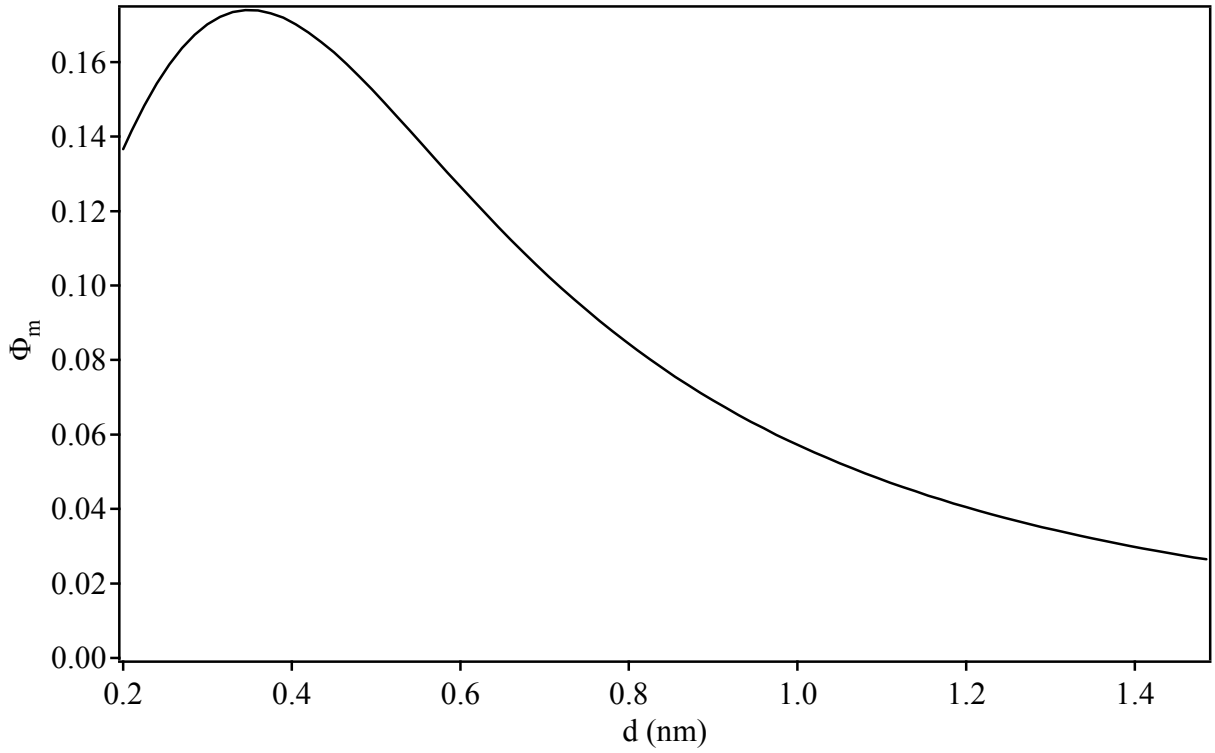

Figure 2.9: Φ_m versus d for {111} Al with ρ = 60 atoms/nm^3. The position of Φ_m changes with d and has a maximum value of 0.17. This is important to consider when doing comparisons between different FEM data sets, as the maximum in Φ will determine the in the trend of V with Φ. Figure from [87].

Figure 2.8 shows $V(C_{111}\Phi)$ at constant d, calculated both by the binomial method and the Gaussian approximation, which are in excellent agreement over the latter's range. This figure shows a maximum in $V(C_{111}\Phi)$ that increases and shifts to higher Φ with increasing d, indicating that V is most sensitive to a dilute crystal density (Φ on the order of 0.07). The location of the maximum is

$$\Phi_{\mathrm{m}} = \frac{6\pi d}{C_{hkl}\left(72 - 6\pi + \pi^2 d^3 \rho\right)}. \qquad (2.28)$$

Above this maximum, adding more crystals makes the sample more uniform, reducing V. Figure 2.9 shows Φ_m versus d at R = 1.5 nm for Al {111}, which itself has a maximum of Φ_m = 0.17. Knowing this maximum location is important to applying this theory, since it determines the trend in V versus Φ. Moreover, since Φ_m depends on C_{hkl}, different peaks in $V(k)$ might respond in different directions to a change in Φ.

How can a *decrease* in V correspond to an *increase* in Φ? There are two extremes of $C_{hkl}\Phi$. The first extreme is $C_{hkl}\Phi$ approaching 0, meaning no MRO in the system, only disordered material which we assume is structurally homogeneous. At $C_{hkl}\Phi = 0$, $V = 0$, which is expected since V measures structural heterogeneities in the material, and no order in the amorphous material means no structural heterogeneities and a minimal V. The other extreme is saturated MRO in the sample, for which $C_{hkl}\Phi = 1$. Because of the definition of the Bragg active fraction C_{hkl}, $C_{hkl}\Phi = 1$ not only requires that the system is saturated with nanocrystals, but also that all nanocrystals in the model are oriented in the same direction. At $C_{hkl}\Phi = 1$, $V = 0$, which is again expected since this is similar to a single crystal, again with little or no structural heterogeneities, meaning minimal V. This scenario is shown pictorially in Figure 2.10, where $C_{hkl}\Phi = 0$ or 1 corresponds to TEM images of either black or white, with no variability in the diffracted intensity. If we add some order to the disordered material, we increase the spatial heterogeneity of the material, thus increasing V. There is a combination of d, $C_{hkl}\Phi$, and other sample parameters at which V is a maximum; for higher Φ, $V(\Phi)$ decreases. For high Al-content amorphous alloys, we estimate the location of this maximum to be at $\Phi \sim 0.1$ [87]. From TEM

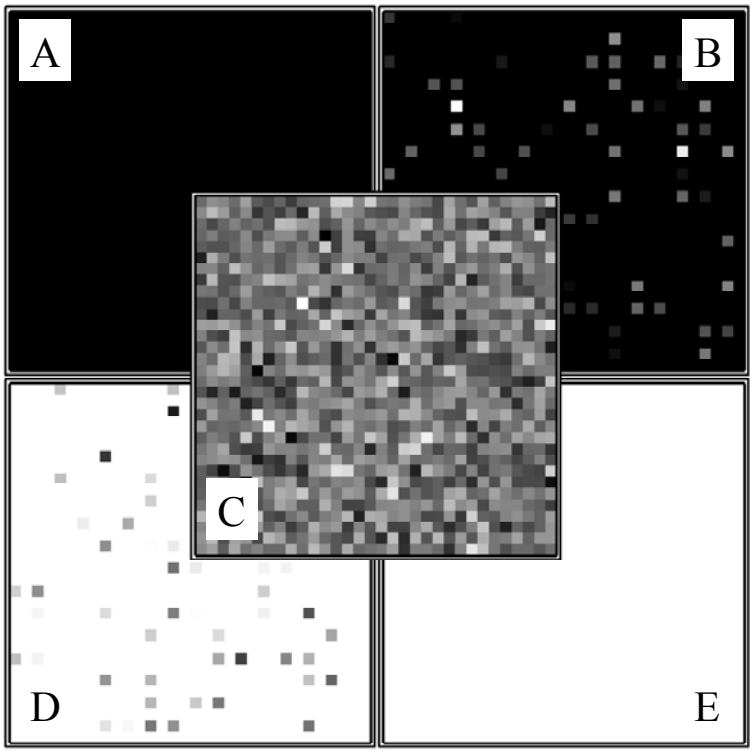

Figure 2.10: Representative illustrations of $V(C_{hkl}\Phi)$ as Φ increases. At $\Phi = 0$ (inset A) the sample is homogeneously disordered resulting in a minimal V. At $0 > \Phi > \Phi_{max}$ (inset B) the sample becomes spatially heterogeneous, increasing V. Once $\Phi = \Phi_{max}$ (inset C) the sample becomes maximally heterogeneous, maximizing V value. As more nanocrystals are added to the sample, $\Phi_{max} > \Phi > 1$ (inset D). While the sample is still spatially heterogeneous, it becomes more spatially uniform resulting in a decreased V. Finally, at $\Phi = 1$ (inset E) the sample is again homogeneous, but ordered, resulting in a minimal V once again.

dark field imaging of Al nanoparticles after primary crystallization, we estimate Φ at 0.20, higher than the maximum.

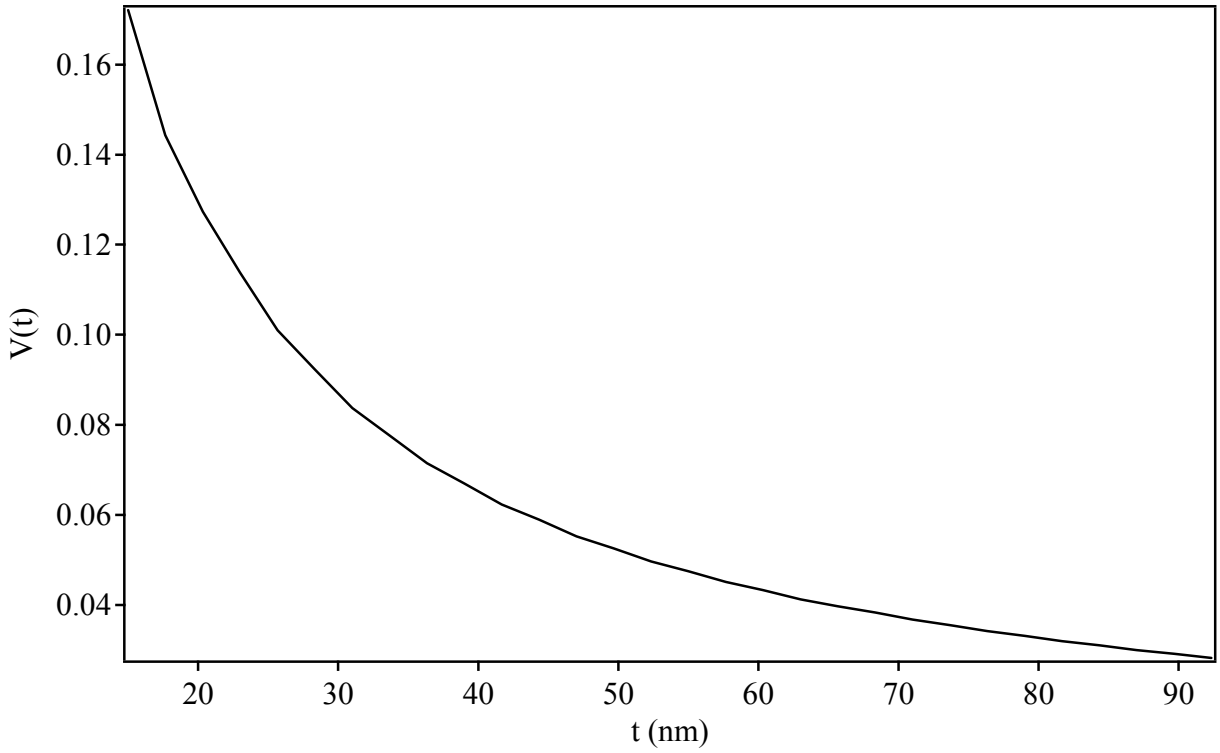

Figure 2.11: $V(t)$ for Al {111} with following parameters: d = 1.2 nm, Φ = 0.20, R = 1.5 nm, ρ = 60 $^{\text{atoms}}/_{\text{nm}^3}$ and t = 40 nm. Figure from [87].

Samples for FEM must be thin compared to the elastic mean free path to limit multiple scattering, but Equation (2.27) shows they must also be thin because $V(t)$ monotonically decreases with increasing t, as shown in Figure 2.11. As N_b increases (more bins through the thickness of the column) the structure of each column more closely reflects the average structure, and V decreases. The relevant length scale is then the average intercrystal spacing, and the sample should be < 10 units thick. Figure 2.11 also emphasizes to use samples that are the *same* thickness for FEM; otherwise quantitative comparisons between samples are not meaningful.

The thickness of amorphous samples can be conveniently measured using the bright-field transmittance through a small objective aperture [101], yet this only gives the thickness in terms of mean free path units, not absolute units.

For VR-FEM, Equation (2.27) predicts $V \propto 1/R^2$. This is consistent with the previous result [80] shown in Equation (2.1). In our terms, $Q = 0.61/R$ and $\Lambda \propto d$. For $Q \ll \Lambda/2\pi$, which ensures the requirement of our theory that $R>d$, Equation (2.1) reduces to $V \approx \Lambda^3 Q^2 P(k) \propto d^3/R^2$, similar to Equation (2.27).

Our theory predicts a more complicated proportionality constant between V and $1/R^2$ which depends on all the sample parameters: d, Φ, C_{hkl}, t, and ρ. To simplify things somewhat, we assume that the number of atoms in the crystal is much larger than one (which is true even for a 1 nm diameter crystal), so that in Equation (2.26) $D-1 \approx D$. We further assume that in Equation (2.27), $\left(1-\frac{6C_{hkl}\Phi}{\pi d}\right) \approx 1$. For our FEM experiments on Al-based amorphous metals discussed below, $\frac{6C_{hkl}\Phi}{\pi d} \approx 0.08$, and for amorphous silicon it is even smaller. The result is

$$V \approx \left\{ \frac{\frac{\pi}{6} C_{hkl} \Phi d^2 \left(\frac{\pi}{6} d^3 \rho \right)^2}{t\left[C_{hkl}\Phi \left(\frac{\pi}{6} d^2 \rho \right) + 1 \right]^2} \right\} \frac{1}{R^2}, \qquad (2.29)$$

where the term in {} is the slope of line of V vs. $1/R^2$, the output of a VR FEM experiment. If we denote that slope Ω and solve for d, we find as the only real positive root

$$d = \left(\sqrt{\frac{3}{2\pi} C_{hkl} \Phi t \Omega} + \left(1 + \sqrt{1 + \frac{4}{C_{hkl} \Phi t \Omega \rho} \sqrt{\frac{6t\Omega}{\pi C_{hkl} \Phi}}} \right) \right)^{1/2} . \qquad (2.30)$$

Ω, t, ρ, and C_{hkl} will generally be known for a given experiment, making Equation (2.30) a relationship between d and Φ. If Φ can be estimated independently, as is the case in the experiments discussed below, then d could be extracted from the results of a VR FEM experiment. The only published VR-FEM data is for two different resolutions on amorphous silicon [67]. Using the slope from those two points and an estimated $\Phi \sim 2.8 \times 10^{-4}$ for this system from dark field images of amorphous Si [87,92], we find $d = 1.17$ nm. From the same data, the correlation length theory of Equation (2.1) 3.5 nm [67]. Since the two lengths have different definitions, the lack of quantitative agreement is not meaningful, and only further experiments will determine whether or not the two analyses show the same behavior across different samples and a broader range of resolution.

This theory can also be used to extract sample parameters from VC FEM experiments with multiple Bragg peaks present. Two different V values at different Bragg reflections (with different C_{hkl} values) provide a situation with two equations and two unknowns (d and Φ). This will be discussed in detail in Chapter 5 to explain results on alloying $Al_{88}Y_7Fe_5$ with Cu.

2.08 Summary

Overall, this theory for V captures the thickness dependence via projection, the Φ dependence within limits, an approximate d dependence, and some information about relative peak heights in V through C_{hkl}. This theory does not treat scattering between crystal Bragg conditions, polyatomic systems, or subtle, non-crystal like MRO. Given the simplicity of the

sample structure and the scattering model, we stress that this theory should not be used to calculate absolute values of d from the absolute magnitude of fixed-resolution VC-FEM data. Instead, this FEM theory is useful in identifying general trends in V with d and Φ, the MRO size and density.

Chapter 3.

Experimental Set-up

Preparing samples and operating the TEM correctly for FEM experiments is nontrivial. Not only must care be taken to ensure information gathered is intrinsic to the sample and not a sample preparation artifact, but the microscope and recording device can also influence *V*. In this chapter I describe a step-by-step process of sample preparation, TEM operation, and image processing that will guard against imaging and sample artifacts and to ensure reproducible data.

3.01 Sample Preparation

High Al-content amorphous alloys are made by cooling a liquid form of the proper atomic composition rapidly enough so no crystallization occurs. As discussed in Chapter 1, for a marginal glass system like ours, to maintain a disordered structure by quenching of the liquid metal requires extremely high cooling rates (order of 10^5 K/s), which we achieve by melt-spinning.

Melt-spinning starts with a bulk ingot of the proper composition usually made by arc melting. This ingot is melted and injected onto a single wheel melt spinner spinning at a tangential wheel speed of 55 m/s in an inert atmosphere. The resulting amorphous ribbon is approximately 0.5 mm thick, 3 mm wide, and roughly a meter long. Even with this aggressive cooling, the ribbon is not amorphous over its entire length. Pieces of ribbon are checked initially for flexibility. High Al-content amorphous alloys are much more ductile than the crystallized material, so amorphous ribbon can easily bend through 180^{o}, while a crystalline ribbon will usually break. A quick bending test can quickly determine a good batch of amorphous ribbon from a bad batch, and save instrument time. The as-quenched ribbon will slowly crystallize at room temperature, so all samples were kept in a freezer at -30 ^{o}C when not in use.

Prior to TEM sample preparation, all amorphous ribbons were checked by XRD for crystal peaks using a Siemens High Star XRD with a two-dimensional detector. This step is only looking for sharp crystal peaks in the diffraction pattern. Representative diffraction patterns from amorphous and crystalline materials are seen in Figure 3.1. Samples with sharp diffraction peaks are discarded.

Samples were then prepared for the TEM. Prior to any thinning, each sample was degreased using a 25 vol % solution of commercial degreaser (Orange Clean) and 75 vol. % distilled water. Next, the oxide layer was removed from the bulk samples with a 30 second soak in as purchased orthophosphoric acid. Immediately following the oxide etch, samples were electropolished to electron transmittance. All TEM samples are made by electropolishing only, as ion milling has been shown to introduce spurious peaks into V [91]. Electropolishing is done on a Struers Tenopul 5 twin jet electropolisher at a fixed voltage. The electrolyte used for all high

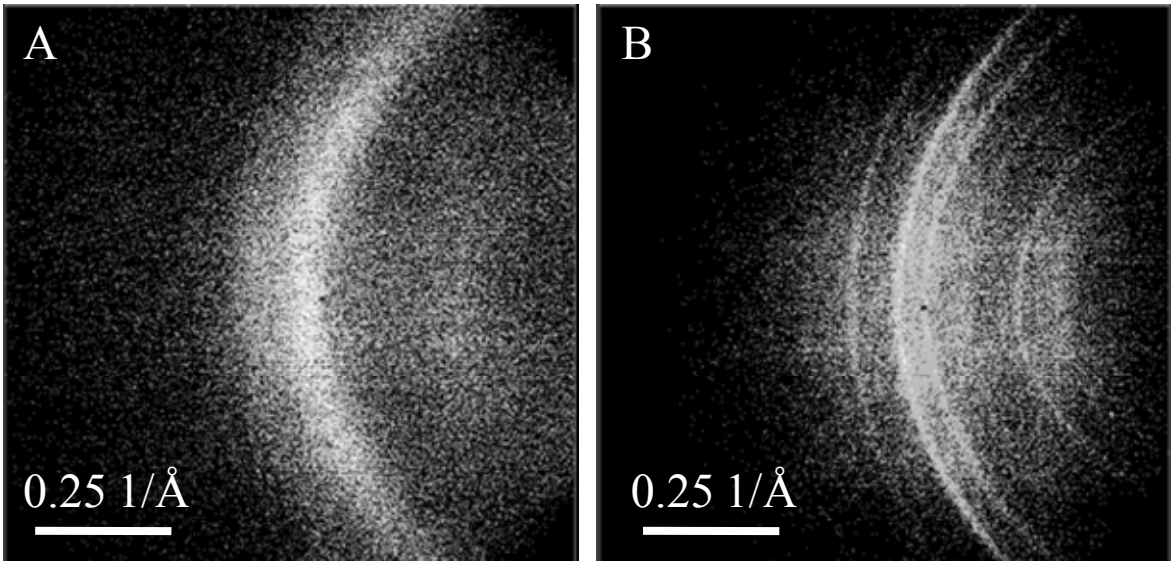

Figure 3.1: Representative 2D XRD traces from high Al-content amorphous alloys. Sample A is amorphous, while sample B has Bragg peaks and is considered crystalline.

Al-content amorphous alloys is 25 vol. % nitric acid 75 vol. % methanol at approximately -40 ^{o}C for 10 – 30 seconds. After the initial electropolish, each sample is viewed under a light microscope to check for forming holes. Samples with no electropolished holes were put back into the electropolisher for further thinning. Initial FEM work showed that the MRO of a thinned TEM sample may change over time when the TEM sample is left at room temperature. To ensure that there were no environmental influences to the MRO of our samples, all thinned TEM samples were viewed within 48 hours of thinning and were kept in a freezer at -30 ^{o}C when not in use.

3.02 TEM Operation for VC FEM

Unless otherwise stated, all FEM work was done on a LEO 912 EFTEM with a ProScan 14 bit cooled CCD camera at the Materials Science Center at the University of Wisconsin – Madison. The objective aperture diameter used was 0.038 1/Å resulting in a 1.6 nm spatial resolution for FEM experiments (0.61 / OA diameter = real space resolution). FEM work on this instrument was of the VC FEM flavor, meaning data was acquired by running the TEM in hollow-cone dark field mode (discussed in detail in Chapter 1). Additional information specific to individual experiments will be discussed in detail in the corresponding chapter.

Images were acquired at k ranging from 0.34 to 0.78 1/Å. Since FEM is a statistical technique to measure the MRO of the sample, all reported V is the average of at least 10 individual areas of the sample. Error bars reported are the standard deviation of the mean. Given that we are measuring V, which is a ratio of intensities, it is important to gather images at the same average number of counts. We need a short enough exposure time to minimize sample drift, which is the limiting factor when acquiring images at high k, but a long enough exposure time to have good statistical signal to noise. We collected FEM data at a variety of average counts per image, and found that 700 average image counts on our equipment is a good compromise between these two factors which gave reproducible FEM results.

As seen in Chapter 2, the FEM theory [87] shows that V is sensitive to the thickness of the sample. Therefore it is important that we not only have thin samples, but also samples that are the same thickness. To calculate the thickness of the sample, we used the electron transmittance [101]. The electron transmittance is the ratio of the average bright field intensity of the sample

$\langle I_{BF} \rangle$, to the bright field intensity of no sample (a hole in the sample with $\langle I_o \rangle$). The transmittance for a thin area is [102]

$$\frac{\langle I_{BF} \rangle}{\langle I_O \rangle} = \exp\left\{-\frac{t}{\Lambda}\right\}, \tag{3.1}$$

where t is the thickness and Λ is the elastic scattering mean free path. To calculate the transmittance on the TEM, first insert the objective aperture used in FEM experiments. Then, take a bright field image of the sample followed by a bright field image of a hole. The transmittance is the ratio of the average number of counts of the two images. We achieved electron transmittance values of 70-75% for FEM experiments on these amorphous Al-alloys. Assuming Λ for crystalline Al of 130 nm [103], we estimate that these samples were 40 - 45 nm thick.

Whenever doing any type of TEM work, prior to taking an image, the sample needs to be in focus. *How do we focus a HCDF image of an amorphous material*? Defocus changes in the microscope blurs the resulting image. Any blurring of the image will reduce the measured V. Therefore, we need to find the defocus value that maximizes V, but this procedure will only be true with diffraction-contrast, dark-field TEM images. For phase contrast, large-aperture bright-field TEM images exact focus is zero contrast meaning $V = 0$. The peaks in $V(k)$ tend to follow peaks in $I(k)$ as seen in Figure 3.2, so we set k in HCDF at the first fuzzy ring of our sample's diffraction pattern. Next we take a series of images a different defocus values Δf, plot $V(\Delta f)$ as shown in Figure 3.3, and set the focus to the maximum. This procedure is done before any FEM experiments to ensure we are focusing to the same "point" at each area of the sample.

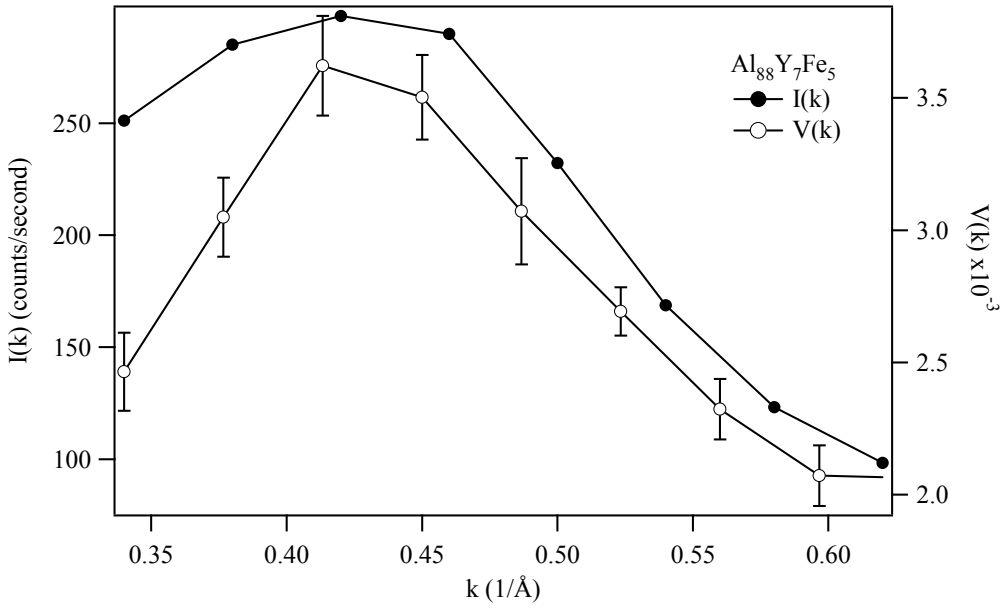

Figure 3.2: Average counts per second versus $V(k)$. Note the first peak position for $V(k)$ matches the first peak position in $I(k)$.

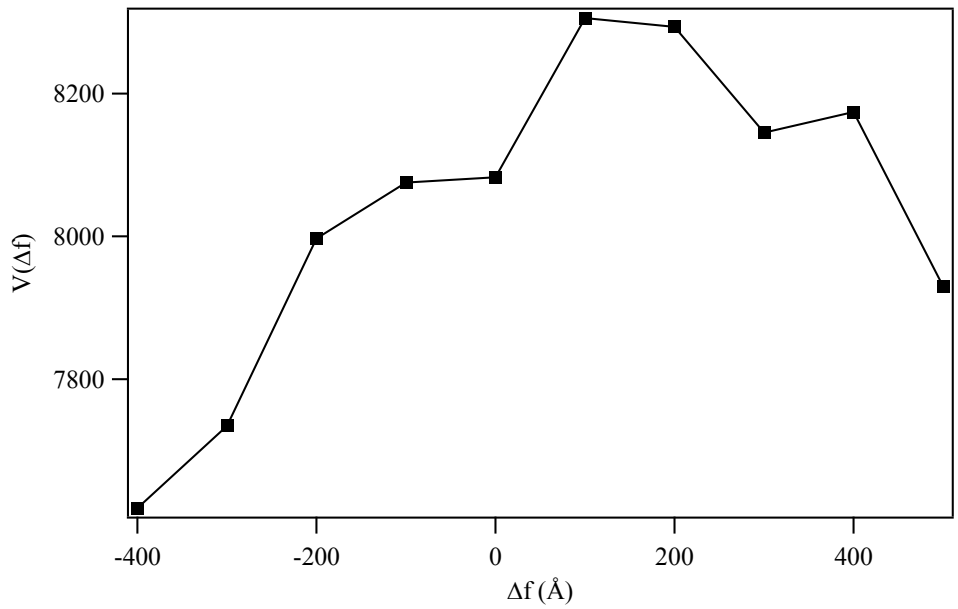

Figure 3.3: Example focal series for a high Al-content amorphous alloy at $k \sim 0.43$ 1/Å. The optimum defocus value in this case is $\Delta f = 100$ Å.

Once the relative thickness is known and the proper defocus value is set, we can acquire a FEM series. The flow chart for TEM operation to obtain a FEM series is shown in Figure 3.4. First obtain a selected area diffraction pattern (SADP), in order to have a record of the initial SRO of the sample area. Next, take a series of images at the same average number of counts at varying *k* tilt values. Images for a single FEM series usually come from a single area of the sample, although this is not required. To detect any effects the electron beam may have on the amorphous samples, different FEM series should alternate from low to high *k* and from high to low *k*. Once the series is acquired, take a final SADP. If the initial SADP and final SADP do not match, the SRO of the sample changed during the FEM series acquisition. If the SRO changes significantly, the MRO has definitely changed and that data set should be discarded. Small changes in the relative intensity can be ignored; but not more drastic peak changes or shifts. Acquisition of focal and tilt series has been automated on the UW LEO 912 TEM.

Lastly, check all images to see they have been acquired correctly. They need to have the proper file format (TIFF), bit depth (16 bit), and average number of counts. One typical problem is that the FEM automation does not capture a HCDF image within 15% of the set average number of image counts. Images that have not been acquired correctly should be discarded and new images should be taken.

3.03 Imaging Instrumental Effects

To properly analyze a FEM series we need to remove instrumental effects intrinsic to imaging with a TEM and CCD camera including the modulation transfer function (MTF) of the CCD camera, the shot noise of the electron beam, and the gain and dark counts of the CCD.

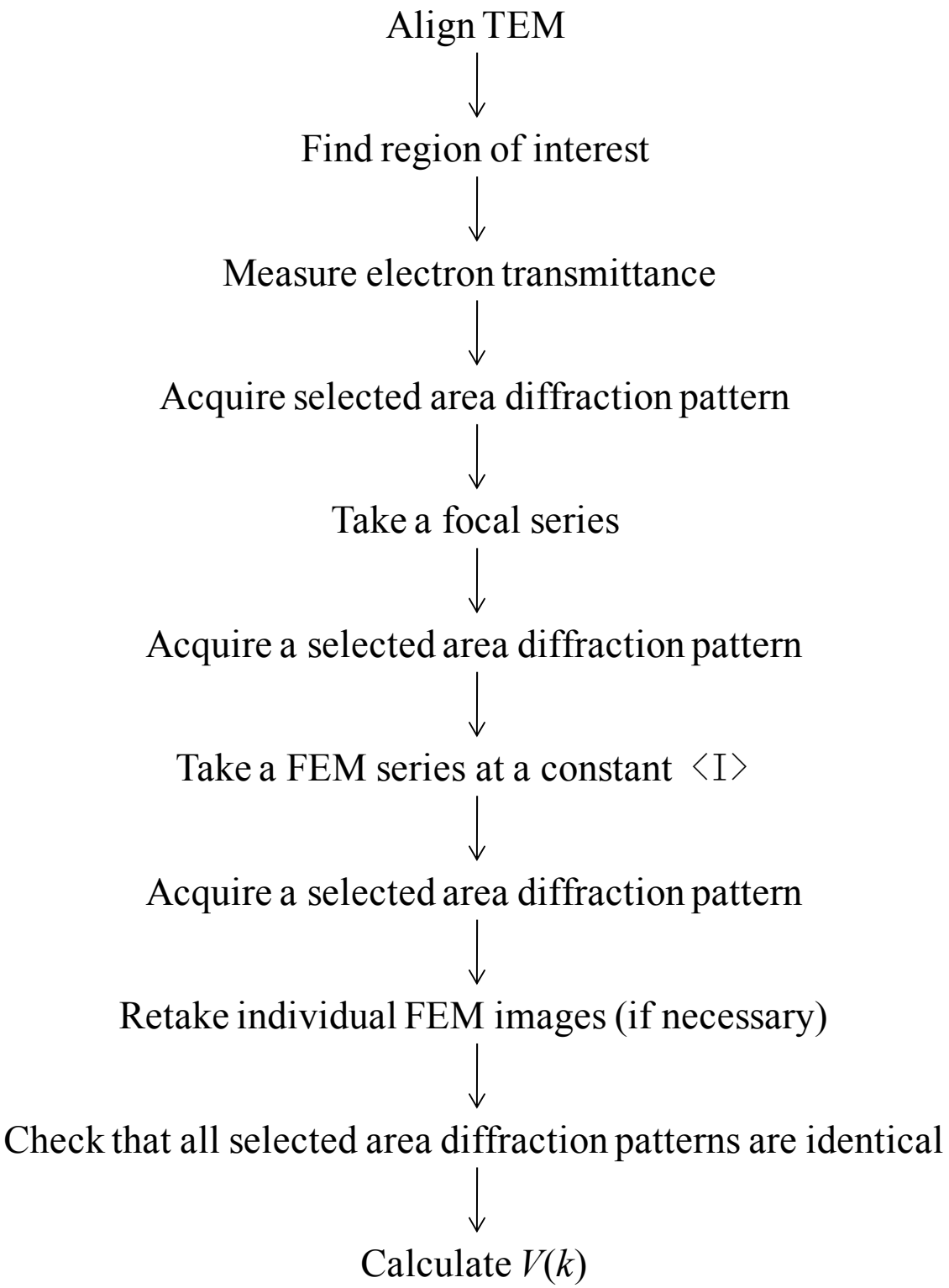

Figure 3.4: Flow chart for a FEM series acquisition

Given that FEM is a quantitative electron microscopy technique, we must remove these factors from our TEM micrographs to ensure we are measuring properties of the sample with as little instrumental influence as possible.

Gain normalization and dark count subtraction are done automatically in the AnalySIS acquisition software. To acquire the gain image, we take several images of the electron beam with no sample. The resulting images will show non-uniformities in the scintillator, fiber optic transfer plate, and CCD chip. These images are averaged into the gain normalization image. Dark counts are inherent to all CCD cameras and are due to thermally induced false current readings in the CCD, meaning the dark counts increase with CCD chip temperature. To minimize dark counts we cool the CCD camera, but even with a cooled CCD there will be a small amount of dark current. The dark current is linear with exposure time, so it can be measured and removed. These two contributions to the images are removed using [104]

$$I_{image} = \frac{I_{raw} - I_{dark}\left(\frac{t_{raw}}{t_{dark}}\right)}{I_{gain}} \tag{3.2}$$

where the quantities are with the corrected TEM image I_{image}, the raw data image I_{raw}, the dark count image I_{dark}, the gain normalization image I_{gain}, the raw image exposure time t_{raw}, and the dark image exposure time t_{dark}.

The MTF is Fourier transform of the point spread function (PSF) of the CCD camera [105]. The PSF is the inherent spread of the electron signal within the CCD camera. Once the imaging electron strikes the scintillator, the signal is changed from an electron to a photon. The photons created by a single beam electron spread as they propagate through the scintillator. The

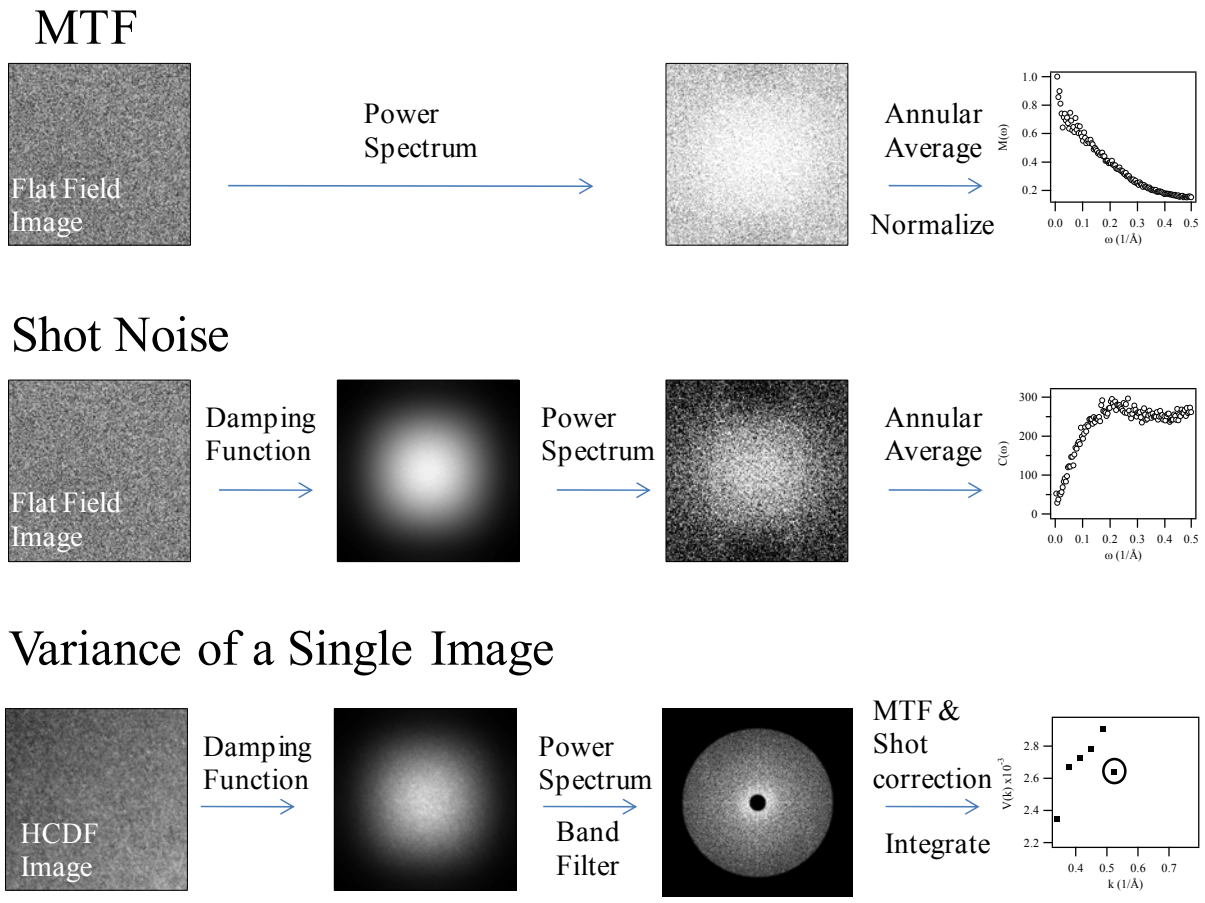

Figure 3.5: Flow chart for obtaining the MTF, shot noise, or a single $V(k)$ point.

spreading occurs the same distance in all directions, so the PSF is rotationally symmetric. This effect is then convolved with each image acquired on our CCD camera.

To measure the MTF, $M(\omega)$, we follow the schematic in Figure 3.5 [105]. First we take 10 flat field electron images at the same average number of counts used in FEM experiments immediately after the gain and dark count corrections. These are images of the only electron

beam at a uniform intensity across the CCD. Next, we obtain the power spectrum, the modulus squared of the Fourier transform, of each image. Then we take the annular average of the power spectrum and normalize the 1-D plot by the zero pixel intensity of the power spectrum. The resulting plot is the MTF of the CCD camera, an example of which is seen in Figure 3.6.

The shot noise $C(\omega)$ of the electron beam is measured almost the identical way, again seen in Figure 3.5. We acquire flat field electron beam image at the same average number of counts we do the FEM experiments. Except now we apply a damping function to the image prior to obtaining the power spectrum. The damping function used is the Hamming function [106]

$$w(n) = 0.54 - 0.46\cos\left(\frac{2\pi n}{L-1}\right), \tag{3.3}$$

with the number of pixels L and the index pixel n. This damps out the edges of the images to zero and minimizes the aliasing effects of the discrete Fourier transform of the image, which is also used in processing FEM images. Next, we calculate the annular average of the power spectrum and the resulting plot is the shot noise, shown in Figure 3.7.

Non-idealities in the sample can cause spurious peaks in V that may be mistaken for MRO signal. This includes surface roughness of our sample or inhomogeneous electron beam illumination. Doing a simple band pass filter on the data images helps minimize the effects of these artifacts. To determine the proper limits for our filter, we make a large table of filtered images at varying filter limits, as seen in

. We visually inspect the table to find the image that maximizes speckle from the sample while minimizing other effects. In the listed FEM experiments reported in Chapters 4 and 5, we used the limits 0.005 to 0.04 1/Å.

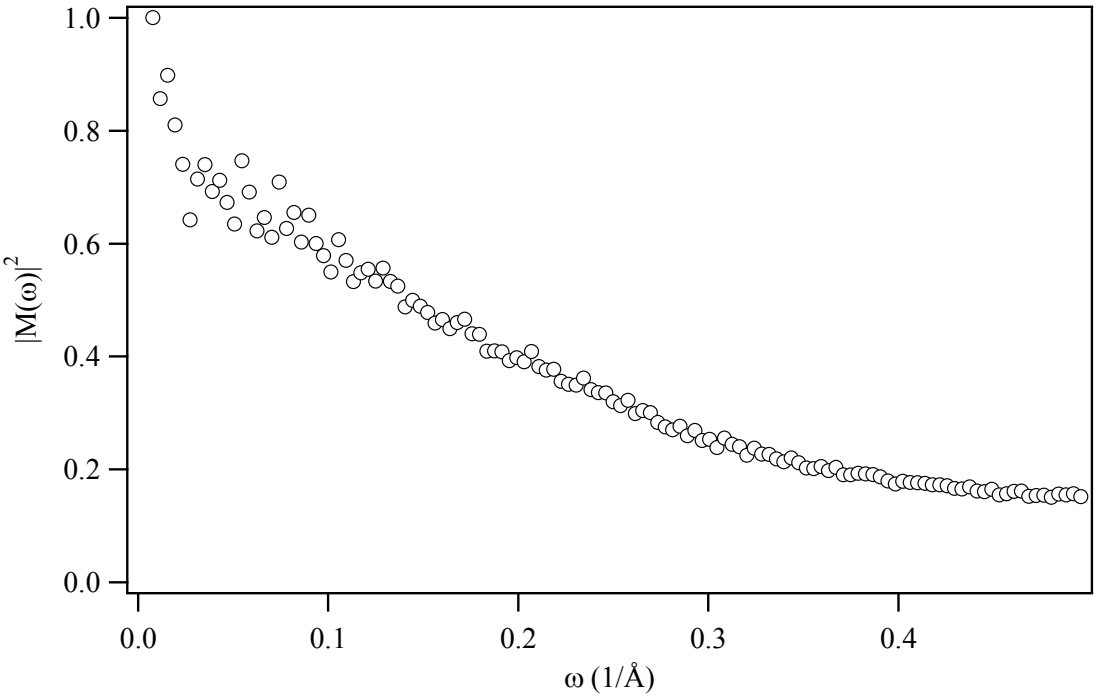

Figure 3.6 MTF for the ProScan CCD camera on the LEO 912 EFTEM at 80 kx.

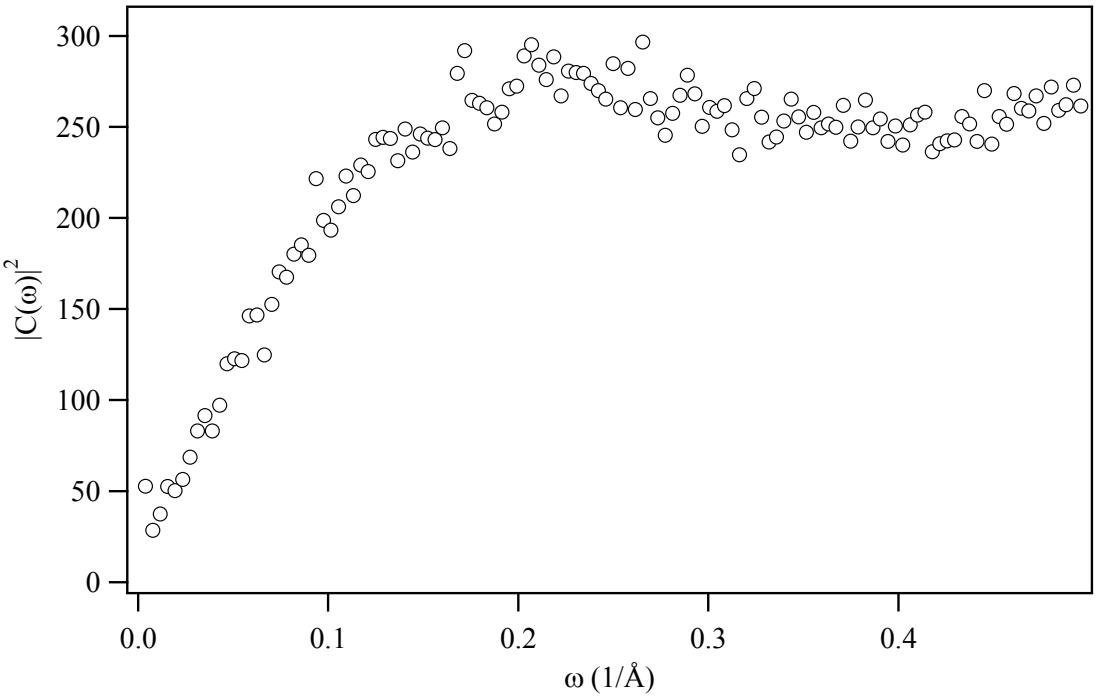

Figure 3.7: Shot noise for the LEO 912 EFTEM at 80 kx measured on a ProScan CCD camera.

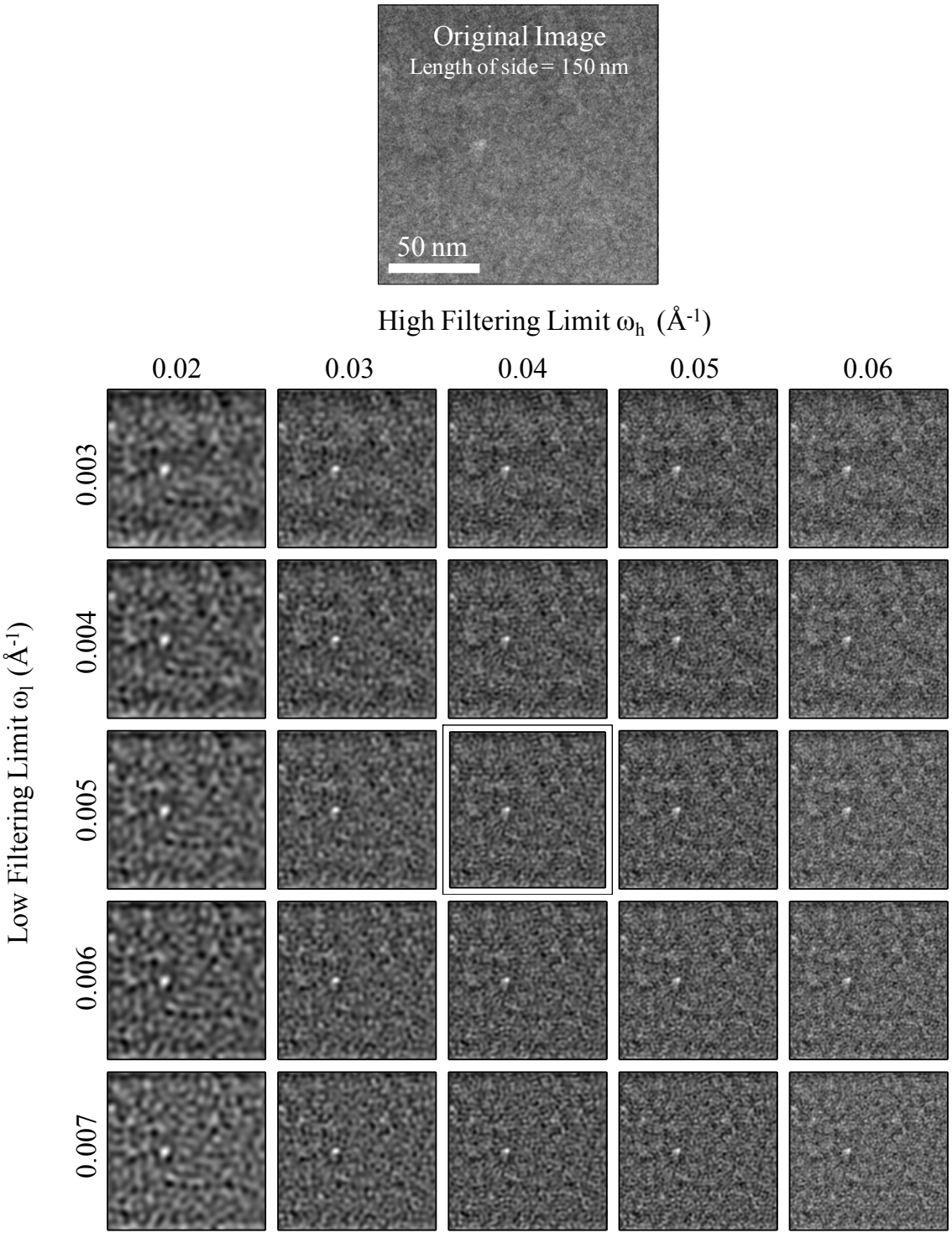

Figure 3.8: Table of Fourier filtering limit effects. Based on this table, we choose limits of 0.005 – 0.04 Å^{-1} for the FEM experiments at 80 kx.

3.04 Image Analysis

Once we have calculated M(ω) and C(ω), we remove these artifacts and calculate *V* from our gain normalized and dark current corrected data images. Since the deconvolution corrections for M(ω) and C(ω) are done in Fourier space, we will calculate *V* in Fourier space using Parseval's theorem [104]. We define the annular average of the Fourier transform of the image intensity as

$$\tilde{I}(\omega) = \int_0^{2\pi} \tilde{I}(\omega, \omega\cos\theta_w)\, d\theta_w \,, \tag{3.4}$$

where θ_ω is the polar angle in Fourier space. If we did not worry about M(ω) and C(ω) removal,

$$V = \int_0^{2\pi} \left|\tilde{I}(\omega)\right|^2 d\omega \tag{3.5}$$

To properly remove M(ω) and C(ω) and to utilize our Fourier filtering, *V* becomes,

$$V = \int_{\omega_l}^{\omega_h} \frac{\left|\tilde{I}(\omega)\right|^2 - \left|C(\omega)\right|^2 \dfrac{\langle I\rangle}{\langle C\rangle}}{\left|M(\omega)\right|^2} d\omega \,, \tag{3.6}$$

where ω_h and ω_l are the high and low frequency limits of the Fourier filtering, $\langle I\rangle$ is the average number of counts in the FEM image, and $\langle C\rangle$ is the average number of counts in the shot noise image. A schematic step-by-step of image variance calculation is seen with the steps for calculation of M(ω) and C(ω) in Figure 3.5.

The last step of image processing involves the incoherent variance, V_o. V_o is variance that is caused by artifacts in the image that produce *V* that is not associated with any MRO in the

sample [101]. Much of the influence of these artifacts is removed by Fourier filtering, but sample features like holes, thickness variations, or roughness may still increase V. Since these artifacts' contrast arises primarily from mass-thickness rather than diffraction, it does not change with k, and they will simply add signal such that

$$V(k) = V_{MRO}(k) + V_O \,, \tag{3.7}$$

where V_{MRO} is V from MRO in the material.

Therefore to measure V_o, we take an image at high k where there is little to no MRO signal [101]. The resulting image can be processed like other FEM images to determine the approximate V_o. Practically, the last image taken in a data set is approximately V_o (at approximately k = 0.78 - 1 1/Å) since there is usually little detectable MRO at higher k due to a decreasing signal to noise ratio at long exposure time.

3.05 Sample Preparation Artifacts

The eternal struggle with TEM work is sample preparation. We cannot have quality data without quality samples. Given that we work with sensitive amorphous materials, we need to give special care to the thinning, storage, and imaging of these samples. During the course of my research I have studied several compositions of high Al-content amorphous alloys. Examining multiple different compositions micrographs and related diffraction patterns brought to light the existence of artifacts.

Diffraction patterns are a simple way to check initially for artifacts. What we look for when comparing diffraction patterns is peak position and relative peak heights (since the

absolute peak height depends on instrumentation rather than sample properties). When doing a quantitative comparison of diffraction patterns, first the patterns must all be 1D. Next, fit Gaussian curves to the broad diffraction peaks. Since these materials are mostly Al, we fix the centers of the Gaussians at the Al Bragg peak position. Lastly, we compare the relative peak heights between XRD and ED patterns. Since the scattering cross-sections are different between x-rays and electrons, the patterns will not match identically. We look more for consistency. Are the relative peak heights similar? Is the {111} peak always higher than the {200}? If there is a glaring inconsistency between the XRD and ED patterns (like peaks missing or backward peak intensity ratios), then we look into the possibility of sample preparation induced artifacts.

3.06 Experiment Addendum for Sample Preparation Artifacts

We have studied $Al_{88}Ni_8Sm_4$, $Al_{90}Ni_7Ce_5$, and $Al_{88}Y_7Fe_5$, prepared by electropolishing as described previously. We also prepared samples by acid etching in 25 vol. % sulphuric acid, 70 vol. % orthophosphoric acid, and 5 vol. % nitric acid [107]. Samples were soaked in the acid etch at 5 minute intervals and investigated with an optical microscope. This process was continued until small holes could be seen in the sample. Any ion milling was done on a Fischione model 1010 ion mill at 9^o milling angle, 4 kV, 3.5 mA, at a maximum temperature of -50 ^oC for a maximum time of 20 minutes. Samples were then cleaned with methanol and ethanol and attached to a copper grid. The x-ray diffraction in this section was carried out on a STOE x-ray diffractometer with a FWHM divergence angle of approximately 0.3 degrees in 2-theta.

3.07 Thickness Dependant Thinning Artifacts

Generally, ED patterns for amorphous alloys containing Ni ($Al_{88}Ni_8Sm_4$ and $Al_{90}Ni_7Ce_3$ in Figure 3.9 and Figure 3.10 respectively) showed a forked diffraction pattern with peaks corresponding to {111} and {200} Al and the {220} and {221} Al_3Ni Bragg reflection positions. Non Ni containing alloys ($Al_{88}Y_7Fe_5$and $Al_{92}Sm_8$ [40]) showed a single broad peak in the electron diffraction pattern corresponding to Al Bragg peaks.

A closer look at the annular averaged electron diffraction data for Ni containing alloys shows a thickness dependence of the relative weighting of the two peaks in the diffraction pattern. Thinner regions (> 70% electron transmittance) of the alloys show a higher second peak relative to the first peak, while thicker specimens (< 70% electron transmittance) show relative peak heights that are similar to each other.

X-ray diffraction patterns for $Al_{88}Ni_8Sm_4$ and $Al_{90}Ni_7Ce_3$ do not readily show this forked peak at the {111} and {200} reflections, Figure 3.9 and Figure 3.10 show those x-ray data with a single broad peak. Residuals from peak fitting using either Gaussian or Lorentzian curves, in Figure 3.11, show this first broad x-ray peak is most likely the summation of two peaks with centers at or near the {111} and {200} Al Bragg reflection positions. Therefore we conclude the evenly forked ED from thicker areas matches the XRD and therefore is representative of the majority of the specimen.

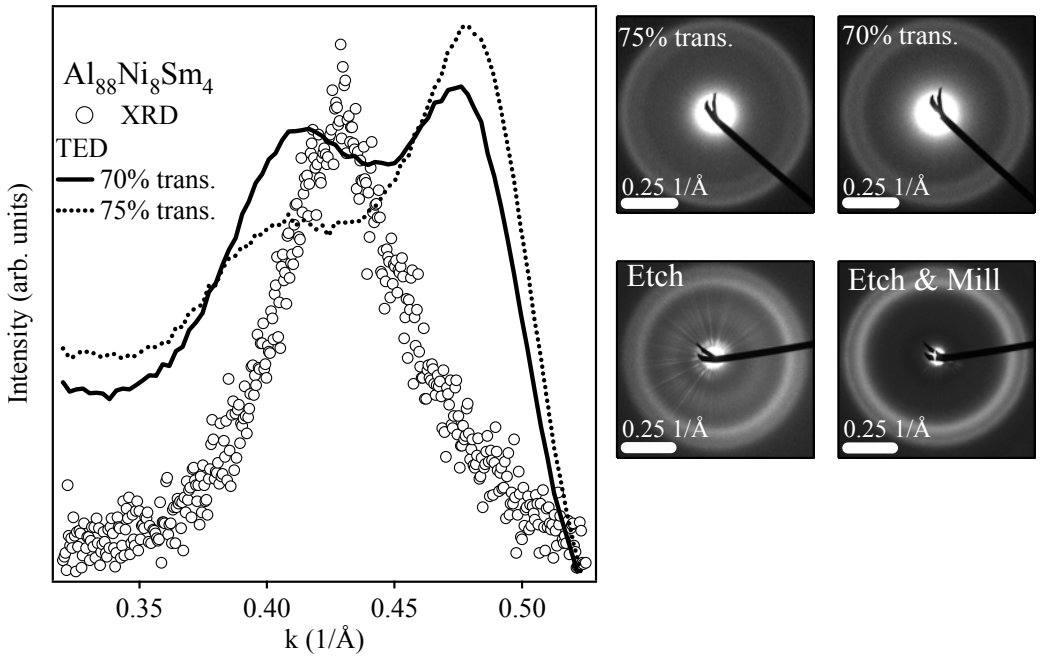

Figure 3.9: Electron and x-ray diffraction patterns for $Al_{88}Ni_8Sm_4$. Changes in the diffraction pattern correspond to sample thickness.

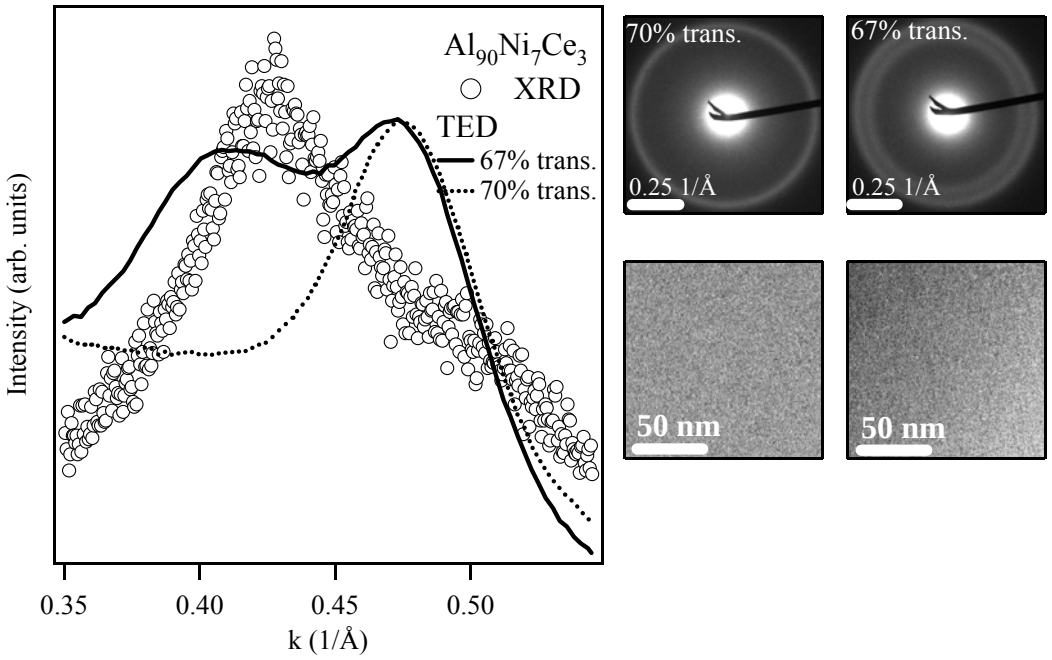

Figure 3.10: Electron, x-ray diffraction patterns, and bright field TEM images for $Al_{90}Ni_7Ce_3$.

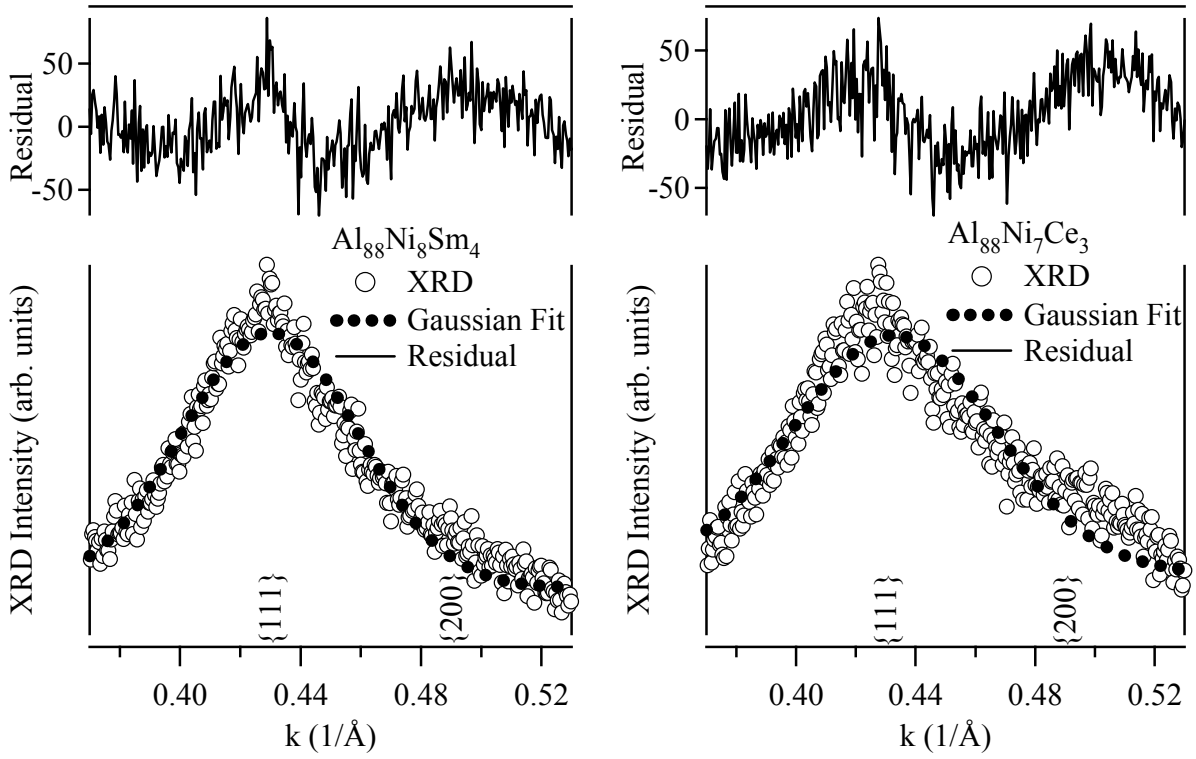

Figure 3.11: Residual fits for a single Gaussian to XRD patterns for $Al_{88}Ni_8Sm_4$ and $Al_{90}Ni_7Ce_3$. The residual matches the Al{111} and {200} Bragg positions, which are noted in the figure.

Investigation of $Al_{88}Ni_8Sm_4$ shows that this change in the SRO is particular to samples prepared via electropolishing only. We compared diffraction patterns from specimens prepared via acid etching, and via acid etching with further ion milling. Figure 3.9 shows representative acid etching and acid etching with ion milling electron diffraction patterns. While these specimens were much thicker than those prepared by electropolishing, we did not see any change

in the ratios of the first two peaks. This same trend is observed with $Al_{90}Ni_7Ce_3$, and shown in Figure 3.10.

This thickness dependant ED phenomenon was not seen in the as prepared material of a non Ni containing alloy, $Al_{88}Y_7Fe_5$. Yet, as seen in Figure 3.12, specimens of $Al_{88}Y_7Fe_5$ that were annealed for 6 hours at 200 ^oC, did show a thickness dependant diffraction pattern. Annular averaged patterns clearly show that thinner regions have a much more diffuse diffraction pattern when compared with the thicker and unannealed counterparts. Figure 3.13 shows the corresponding bright field for the $Al_{88}Y_7Fe_5$ ED patterns. Figure 3.13, and bright field images from the $Al_{88}Ni_8Sm_4$ and $Al_{90}Ni_7Ce_3$ samples (Figure 3.10), were uniform in contrast, so this diffraction phenomena is not from phase separation or a related process, as suggested by [108,109].

What is causing this change in the SRO? We can eliminate some possibilities; we do not think this electron diffraction phenomenon is caused by multiple scattering in the electron diffraction patterns. Since the samples are quite thin, estimated to be ~ 40 nm thick, the small change between 65 % and 70% electron transmittance correspond to only a 17 % change in thickness. Given that these diffraction patterns are amorphous, we do not attribute this phenomenon to any type of crystallization caused either before or after sample thinning. Also, since we see this change in the diffraction pattern on the same samples at close proximity, this issue is not caused by contamination within the column.

We therefore think this change in the diffraction pattern represents a change in the sample SRO in the form of structural changes, chemical changes, or a combination of both. Since the

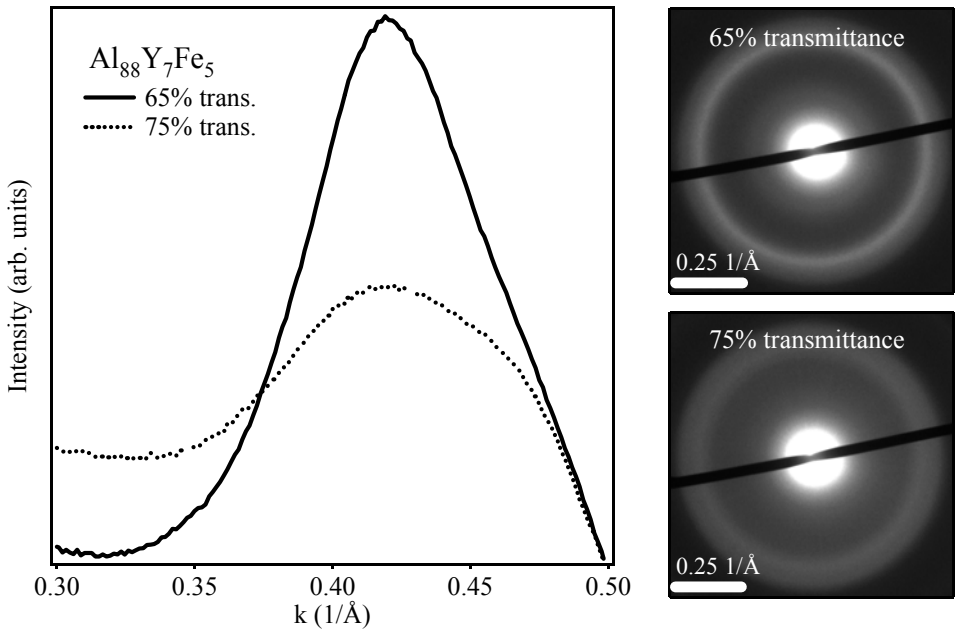

Figure 3.12 Electron and x-ray diffraction patterns for $Al_{88}Y_7Fe_5$ annealed for 1 hour at 200 ^oC

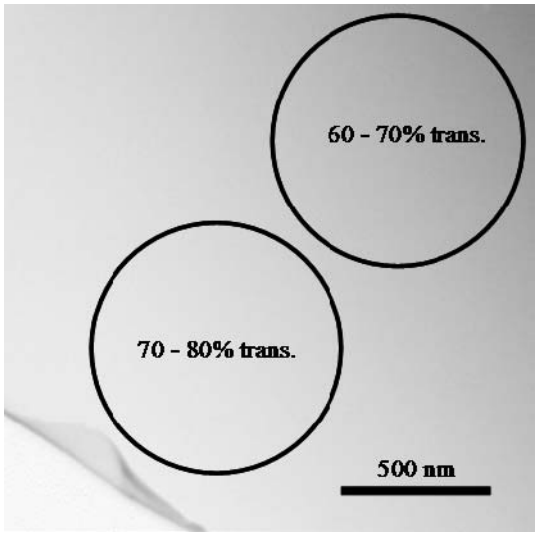

Figure 3.13: Bright field image for ED patterns in Figure 3.11 of $Al_{88}Y_7Fe_5$ annealed for 1 hour at 200 ^oC

XRD data is consistent with the electron diffraction patterns from thicker samples, we further conclude that this artifact is only seen in thinner regions of electropolished thinned TEM samples. Overall, we conclude that this phenomenon is an electropolishing preparation artifact and is not consistent with the bulk structure of these alloys.

Similar ED and XRD patterns between the thinned sample and the bulk material are a necessary, but not sufficient condition, to prove there are no thinning artifacts. If the diffraction patterns are different, obviously there must be an artifact. However, since diffraction patterns only measure the SRO, there may be subtle changes to the MRO by sample preparation that are not obvious. That is why it is important to view multiple areas of the sample to try and obtain a full picture of the sample, if measured $V(k)$ peaks averaged from several samples are statistically different, we have additional confidence that we are measuring the inherent structure of the material.

The easiest way to avoid these artifacts in the TEM is to compare ED and XRD patterns. If the SRO of the material being measured in the TEM is identical to the bulk material, the diffraction patterns should match or be very similar. The annular average of the electron diffraction pattern is required so that even small changes to the relative intensity of the diffraction pattern can easily be seen. Then we can ensure that the area of the specimen we are analyzing has a structure that is consistent with the bulk material of the sample.

3.08 Beam Induced Crystallization of Amorphous Samples

This section contains material that was previously published as
Stratton et al., Intermetallics, 2006. 14, p. 1061

These materials may also change structurally with prolonged electron beam exposure. If the ED pattern changes with exposure to the electron beam, this means the experiment has fundamentally changed the structure of the material and the FEM results are meaningless.

Beam-induced changes to the specimen structure are always a concern for electron microscopy, particularly of amorphous materials. If our sample changes with electron beam exposure, we may be measuring that mechanism rather than properties intrinsic to our material. To measure beam sensitivity, we measure the SRO and MRO of our samples as a function of beam exposure time. One of the high Al-content amorphous alloys we studied, $Al_{92}Sm_8$, showed changes in the ED patterns in Figure 3.14, and therefore the SRO, in less than 10 minutes of beam time. The crystalline Al {200} peak grows rapidly, and a {111} peak starts to appear on the right-hand side of the broad maxima at low *k*, both indicating that these samples are undergoing primary Al crystallization under the electron beam. The maximum exposure time for limited damage to the diffraction pattern is 7 minutes.

This beam induced crystallization is probably not caused by heat generated from the beam. Al has high thermal conductivity (230 $Wm^{-1}K^{-1}$ at 300 K [110]), so heat generated from the electron beam is quickly dissipated to heat sinks within the TEM (i.e. the metal sample rod) and the temperature increase in the sample is minimal. Instead, we believe that crystallization is due to atomic displacements caused by the electron beam (knock-on collisions) [82]. When the energy transfer between the imaging electron and sample atomic nuclei are greater than the nuclei

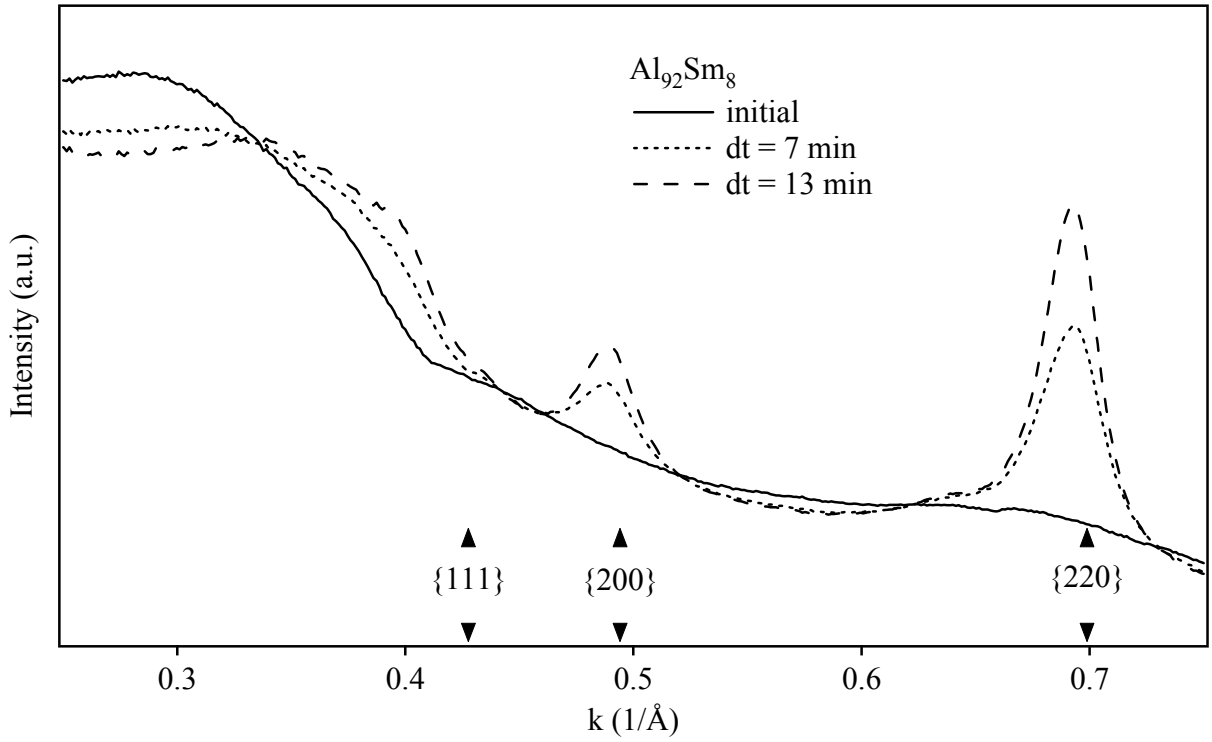

Figure 3.14: Annular average of $Al_{92}Sm_8$ electron diffraction patterns. The loss of the broad peak and the growth of sharp peaks indicate the amorphous sample is crystallizing from prolonged electron beam exposure. The sharp features in the diffraction pattern correspond to FCC Al Bragg reflections, noted as arrows in the figure. Figure modified from [86].

displacement energy, sample atoms can be displaced from their sites. If they are near the exit surface of the sample, the sample atoms can be ejected entirely. The scattering cross-sections for a knock-on displacement is orders of magnitude lower than for elastic scattering [82], which is why we can perform our experiments prior to the sample falling apart under the electron beam.

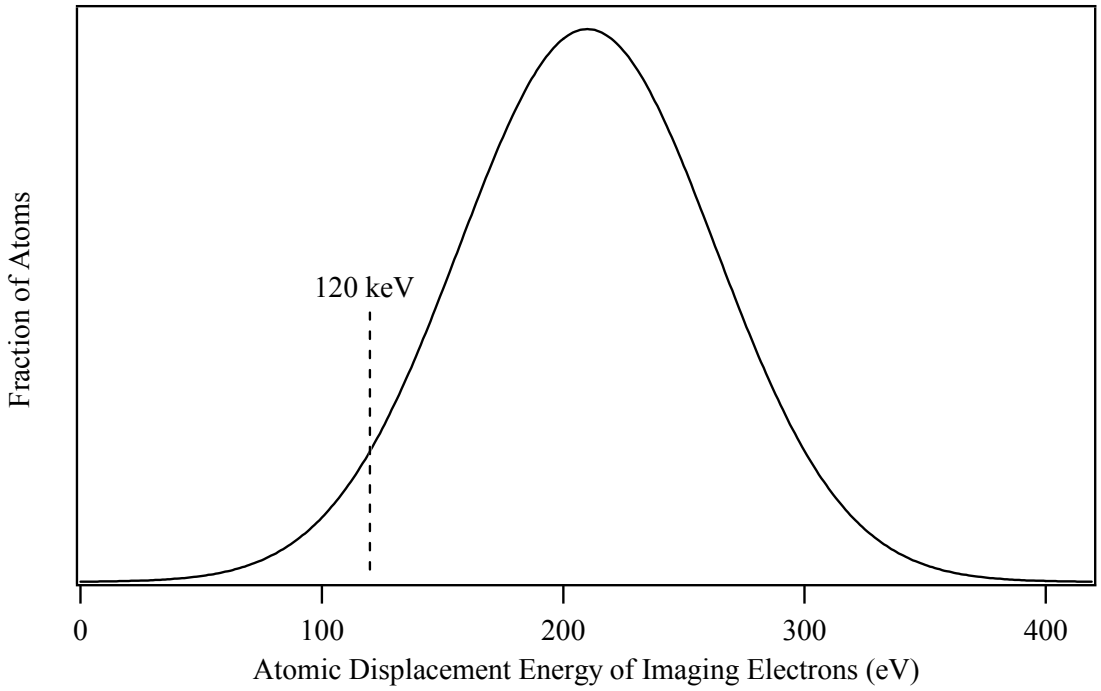

Figure 3.15: Schematic diagram of atomic displacement energies in an amorphous Al alloy. The majority of atoms should have the crystalline displacement energy of imaging electrons of 210 eV, although since this is a disordered material there will be a spectrum of displacement energies. Some of these displacement energies will be less than the energy of our electron beam (120 keV) and therefore can be ejected from the material by knock-on collisions.

Our samples should have similar, but weaker, electron beam robustness as their crystalline counterparts. The displacement energy for crystalline Al is 19 eV [111,112], which makes the corresponding displacement threshold energy of the imaging electrons of 210 kV (calculated from [112]). This is greater than the 120 kV we use to run FEM experiments, but in an amorphous

material there will be a spectrum of displacement energies due to the differing local environments of the atoms, shown schematically in Figure 3.15. In this case since Al is the lightest species in these alloys, it the most likely to be displaced. The low end of the displacement energy range may be several eV lower shifting the threshold to below our beam energy. At 120 kV the corresponding Al displacement energy is 10 eV (calculated from [112]). Unlike damage from other inelastic scattering, knock-on damage is increased at higher beam voltages, such as those routinely employed for high-resolution TEM.

An atomic displacement, especially if the atom is ejected from the sample entirely, will create open space, increasing free volume [113] thus inducing localized mixing in the sample. Only a small amount of free volume is needed to see this effect. A displacement of only 1% of sample atoms is more than enough to induce mixing. Either effect leads to crystallization, since we are increasing open space in the material and therefore lowering the barrier to diffusion.

3.09 FEM Results and Beam Induced Crystallization Limitations

Figure 3.16 shows that $V(k)$ changes on the same time frame as the changes in the diffraction patterns. In $Al_{92}Sm_8$ the MRO first increases, then decreases at longer times. The initial increase can be attributed to beam-induced crystallization. The decrease in $V(k)$ is due to the structure of the material becoming more homogeneous as crystallization proceeds: the image is becoming saturated with crystals, where the average structure begins to resemble more of a single crystal than a disordered material, as in Section 2.07

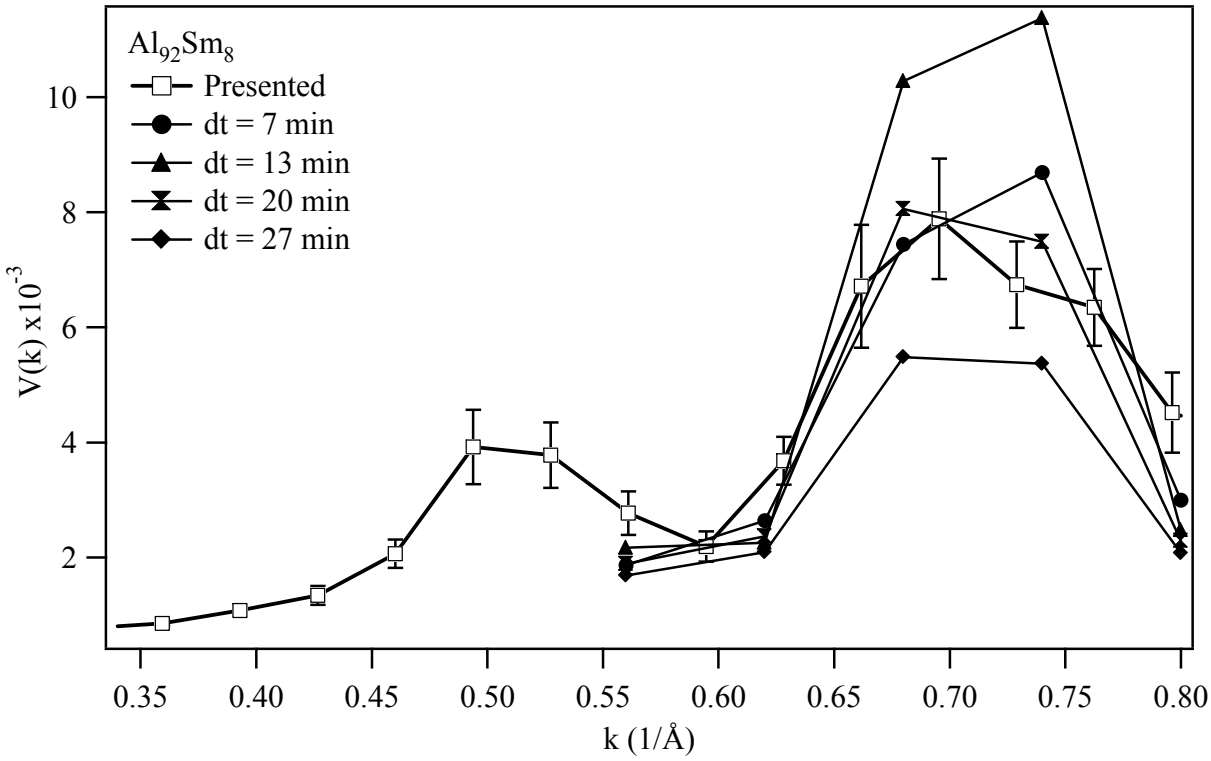

Figure 3.16: $V(k)$ for a single area of $Al_{92}Sm_8$ with beam induced MRO changes. As indicated by the changing $V(k)$, the MRO increases then *decreases* with prolonged beam exposure time. Figure taken from [86].

The acquisition of the $Al_{92}Sm_8$ FEM data (Figure 3.16 and [40]), from low to high k took approximately 20 minutes. The data in Figure 3.14 and Figure 3.16 show that points at greater than approximately 10 minutes of beam exposure time (> 0.65 $Å^{-1}$) will reflect some beam induced changes to the amorphous structure. However, the second peak in the $V(k)$ data was

reproduced in only four minutes of beam time, so we can safely conclude that this peak is intrinsic to the material.

Still, we should modify our FEM technique to ensure no beam induced changes to our material occurs. Based on the data in Figure 3.14 and Figure 3.16, we have only 7 minutes to measure the un-modified structure of $Al_{92}Sm_8$. To reduce the dose to below this threshold, we can divide the relevant *k* range of 0.34 to 0.78 $Å^{-1}$ into four subsections (0.34-0.49, 0.49-0.60, 0.60-0.71, and 0.71-0.78 $Å^{-1}$) each of which can be acquired in less than 7 minutes. The exposure times per *k* point become much longer at higher *k*, so the high-*k* intervals contain fewer data points. To further check against beam induced crystallization being recorded in our FEM measurements, half of the areas in each subsection should be acquired stepping from low to high *k*, and the other half should be acquired from high to low *k*.

This low to high and high to low acquisition step is to compensate for the different information obtained with our diffraction pattern dose measurement and the FEM measurement. The average from low to high *k* and the average from high to low *k* should fall within each other's error bars. As stated earlier, FEM measures more subtle order than diffraction. Therefore just because the diffraction pattern is not changing does not mean the MRO is not changing. Since FEM is a statistical measurement, the averaging together of points with no and minimal beam exposure should preserve the MRO measurement of the material (within the error bars of the results).

This kind of low-dose measurement is possible because the goal of FEM is to statistically characterize the structure of the sample as a whole, rather than to characterize a single microstructural feature as in HRTEM. Essentially, a certain total number of electrons is required

to produce an accurate FEM data set, and the only limit to spreading that dose across an arbitrarily large amount of material is that each individual image must contain enough counts to be above the noise of the detector [67]. Our current measurements are at 3-4 times that level per image, and we still acquire several images from each area of the specimen, so we are far from reaching the low-dose limits to FEM.

3.10 Summary

FEM is a powerful technique to measure the MRO in an amorphous material. We take a lot of care to ensure we are measuring only the structure of the bulk material. Changes to the FEM signal from the instrument and sample are removed with image processing. Sample preparation can also introduce incorrect signals, which can be detected by comparing bulk XRD and thin-sample electron diffraction patterns. Lastly, since these samples crystallize under the electron beam, we developed low dose FEM to measure the amorphous structure while minimizing beam induced structural changes.

Chapter 4.

$Al_{92}Sm_8$

This section contains material previously published as
Stratton et al, Appl. Phys. Lett., 2005. 86(14).

In this chapter we offer an explanation for the difference in devitrification behavior between rapidly-quenched and deformation induced high Al-content amorphous alloys. As discussed in Chapter 1, devitrification of rapidly-quenched high Al-content amorphous alloys below T_g produces pure Al nanocrystals at concentrations $>10^{21}$ m^{-3} [12,19]. This behavior is not seen in the deformation amorphized alloy [12]. This difference is obvious when comparing the TEM micrographs for the high Al-content amorphous alloy $Al_{92}Sm_8$ in Figure 4.1. Both alloys in the as prepared state are amorphous, shown by the ED pattern. When the deformation amorphized $Al_{92}Sm_8$ is annealed at 150 ^oC for 60 minutes, the material remains amorphous, yet when rapidly-quenched $Al_{92}Sm_8$ is annealed at the same temperature for one sixth of the time, a large density of Al nanocrystals form with dendrites. This requires that there must be a structural precursor to primary crystallization present in the rapidly quenched material that is not present in the deformation induced $Al_{92}Sm_8$. As discussed in Chapter 1, various experimental results imply

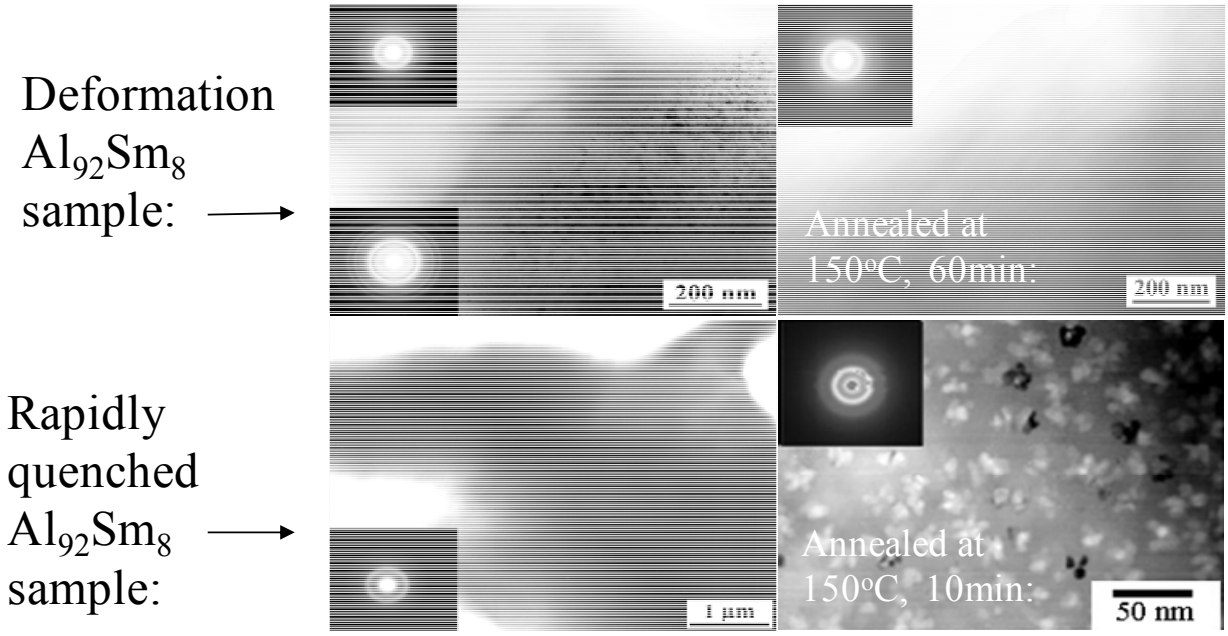

Figure 4.1: Micrographs of $Al_{92}Sm_8$ made by melt-spinning and cold-rolling. Figure from [25].

that the presence of this structural precursor causes $Al_{92}Sm_8$ to devitrify by heterogeneous nucleation [11,114].

As discussed in Section 1.03, the heterogeneous nucleation site had eluded structural or chemical detection, ruling out common sites like second phase interfaces or large impurity clusters. This structure is difficult to detect in amorphous materials using conventional techniques such as XRD [115], given the estimated size of the nucleation site is approximately 1 nm [40]. One possible form of the heterogeneous nucleation site are small proto-crystals that are formed by the rapid quenching of the melt to form amorphous ribbon [12]. Since these proto-crystals are formed at high temperature, they would not be present in amorphous material formed by extreme deformation.

To help differentiate the starting heterogeneous nucleation site, which is some structural difference in the nanoscale structure of the amorphous alloy, we used FEM [66,74] to compare the MRO between rapidly-quenched and deformation induced $Al_{92}Sm_8$. If the hypothesis of quenched-in nuclei is correct, we would expect to see a different type of MRO in the as-quenched material versus the deformation induced material, offering insight into the different devitrification reactions.

4.01 Experiment Addendum for $Al_{92}Sm_8$

Samples of amorphous $Al_{92}Sm_8$ were prepared by rapid-quenching via melt-spinning. Deformation induced amorphous samples were made by cold-rolling, done by deforming elemental foil multilayers at the proper bulk composition with an automatic roller. Samples were rolled and folded until the material showed an amorphous XRD pattern. The overall strain rate was approximately 0.003 s^{-1}, calculated by dividing the total engineering strain (final thickness versus initial thickness) by total rolling time

Annealing experiments were carried out on the melt-spun ribbon in a vacuum oven at 0.3 kPa of air and a temperature of 130 °C (<T_g of 170 °C [12,25]) for 6 and 12 hours. TEM samples were prepared by electropolishing only, and all FEM measurements were done at 1.6 nm resolution. Each $V(k)$ data set is the mean of measurements from at least seven areas of the sample, quoted with one standard deviation of the mean error bars.

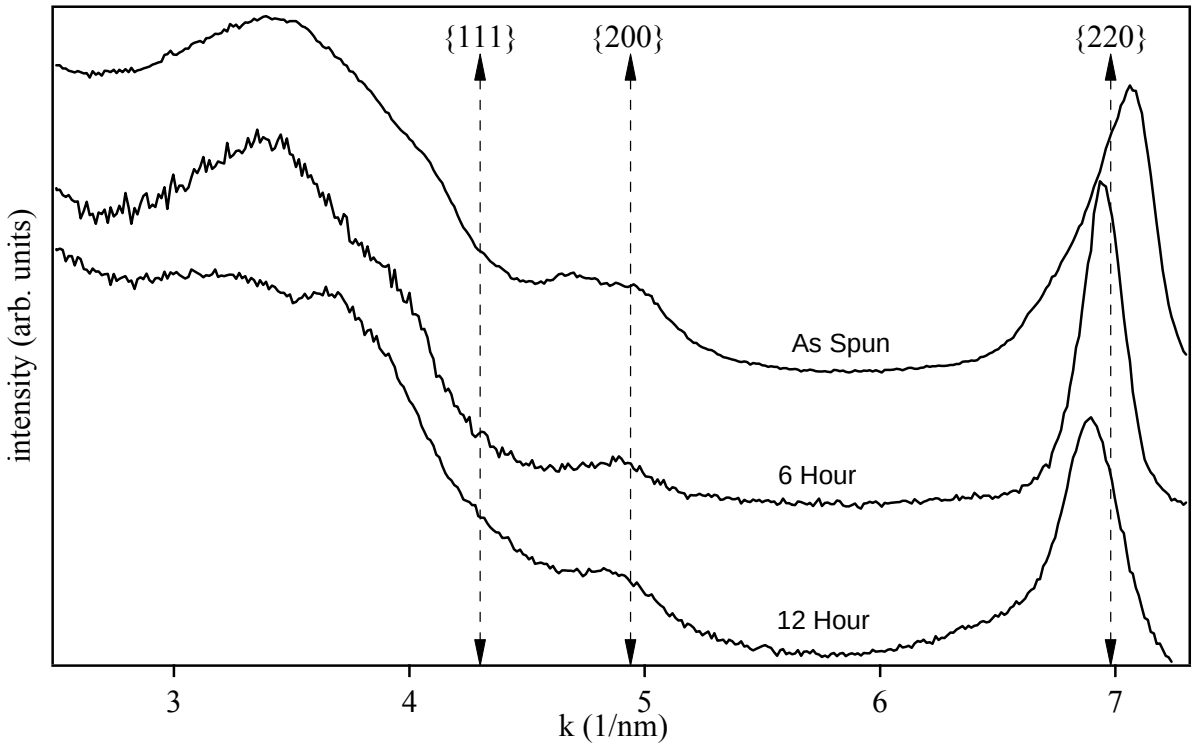

Figure 4.2: The annular average of electron diffraction patterns from melt-spun $Al_{92}Sm_8$ samples as spun and after 6 and 12 hour anneals. The patterns have been shifted vertically for clarity, and the vertical lines indicate the FCC Al {111}, {200}, and {220} reflections. Figure from [40].

4.02 FEM Results for Different Processing of $Al_{92}Sm_8$

Figure 4.2 shows the annular average of electron diffraction patterns from the melt-spun ribbons as a function of annealing. Peaks occur at the Al {200} and {220} positions, but not the {111}. The shifts in the {220} peak could be due to ~1 % strains, but they are probably due to

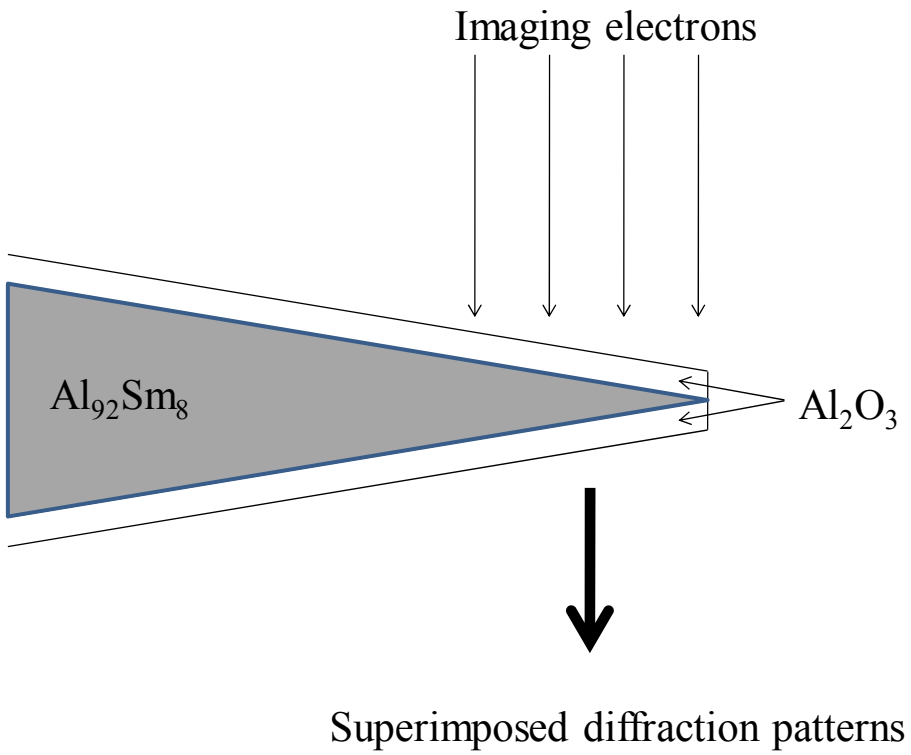

Figure 4.3: Schematic of the thinned $Al_{92}Sm_8$ samples which causes the ED/XRD pattern discrepancy.

drift in the TEM camera length calibration. The change in shape of the low *k* peak after 12 hours of annealing is more likely to be meaningful and may indicate some structural relaxation of MRO back into the amorphous matrix.

The ED patterns in Figure 4.2 do not match the bulk XRD diffraction patterns. The $Al_{92}Sm_8$ XRD pattern matches the $Al_{88}Y_7Fe_5$ XRD pattern seen in the previous chapter. We associate this discrepancy to samples being very thin with Al_2O_3 forming on either side of the sample, as seen schematically in Figure 4.3. This layered sample results in the Al_2O_3 and

Al_2O_3		Al	
hkl	d (1/nm)	hkl	d (1/nm)
(012)	2.9	(111)	4.3
(104)	3.9	(200)	4.9
(110)	6.1	(220)	7.0
(113)	4.8		
(024)	5.7		
(116)	6.2		
(214)	7.1		
(300)	7.3		

Table 4.1: Bragg reflections for Al_2O_3 and FCC Al.

$Al_{92}Sm_8$ diffraction patterns being superimposed. We may be seeing some addition of Bragg peaks for the Al_2O_3 {012} at 2.9 nm^{-1} and the Al {111} at 4.3 nm^{-1}, causing the 3.5 nm^{-1} peak in the recorded diffraction pattern. Table 4.1 gives a full listing of the Al_2O_3 and Al Bragg reflections. However, we know that we are measuring $Al_{92}Sm_8$ rather than an oxide with FEM layer for three reasons. First, published FEM data on amorphous Al_2O_3 [77] does not match our $Al_{92}Sm_8$ data, indicating a different sample structure. Second, we see the all of the Al Bragg reflections with beam induced crystallization. Third, as discussed later in this chapter, our experimental results are similar with FEM simulations of FCC Al spheres.

FEM results on the amorphous melt-spun and cold rolled $Al_{92}Sm_8$ are shown in Figure 4.4. The melt spun material has peaks at 4.9 and 6.9 nm^{-1} corresponding to the Al {200} and {220} reflections. The second peak also covers the Al {311} at 8.2 nm^{-1}. The peak locations in the melt-spun $V(k)$ alone imply the presence of nanoscale order with similar atomic spacings to FCC Al. The cold-rolled material has a totally different $V(k)$ when compared to the melt-spun material meaning the cold-rolled material has a different type of MRO. The cold-rolled data has

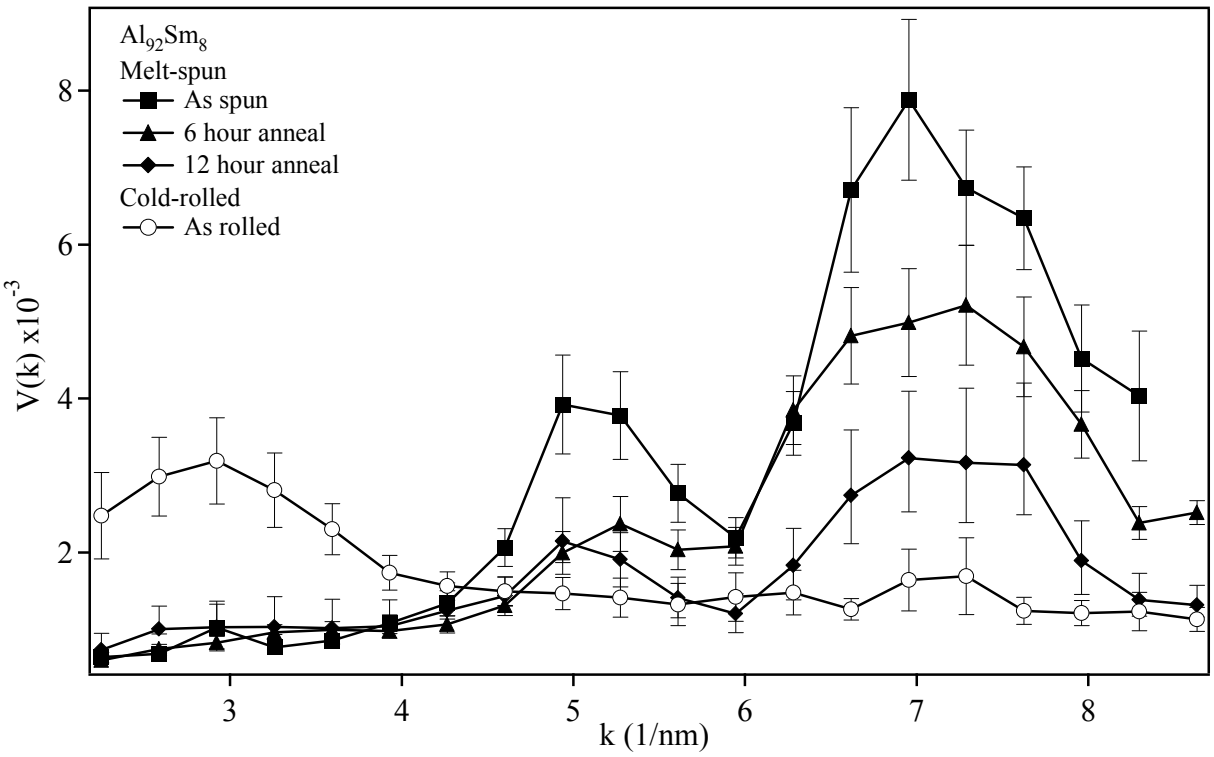

Figure 4.4: Fluctuation microscopy data $V(k)$ for melt-spun as spun, 6, and 12 hour annealed, and cold-rolled $Al_{92}Sm_8$. Figure from [40].

only a single peak at 3 nm^{-1}, which does not correspond to any FCC Al Bragg reflections, but which may correspond to various intermetallic compounds.

As with most TEM measurements on amorphous materials, we must be concerned with electron beam damage to our samples. As discussed in Section 3.08, diffraction and $V(k)$ both show discernable changes after 10 minutes exposure under our experimental conditions. The FEM data in Figure 4.4 took ~20 minutes to acquire scanning from low to high k, so the points at $k > 6.5$ nm^{-1} will have some beam damage. We believe our conclusions remain valid for three

reasons. First, the as-spun $V(k)$ for k = 6-8 nm^{-1} has been reproduced with 4 minutes exposure. Second, the beam-induced change in $V(k)$ is similar in magnitude to the area-to-area variability represented by the errors bars in Figure 4.4. Third, the exposures for each data set are similar, so differences in $V(k)$ on annealing are not beam-damaged induced.

4.03 Identifying the MRO in $Al_{92}Sm_8$

Using computer simulations, we tested several determine possible types of MRO which might be present in the melt-spun material. We found that $V(k)$ simulated for small crystalline Al spheres (2 or 3 nm in diameter) fit the experimental data well. The simulation used an extension of the Dash *et al.* method [85] to binary systems [81] , which is purely a kinematic calculation. Figure 4.5 shows how a simulated 3 nm diameter Al sphere and an icosahedra of 12 Al atoms surrounding a Sm atom [64] compare to the experimental data. The 3 nm simulated Al sphere reproduces both the peak positions and the relative peak heights in the melt-spun ribbon $V(k)$. Intermetallic ($Al_{11}Sm_3$ and Al_4Sm) sphere simulations (not shown) do not even produce the experimental peak positions.

Based on the melt-spun material's peak positions and similarity to a 3 nm Al sphere alone, we cannot call the MRO exactly Al order because these simulations are not a full atomistic model for the material. They involve only the atomic plane spacings that dominate $V(k)$ [81] without signal from the disordered matrix: the model only included a 3 nm Al sphere in a vacuum (no amorphous material). Nor is the 3 nm crystalline Al sphere is not unique in approximating the data; simulations for smaller crystalline Al spheres containing 1-2

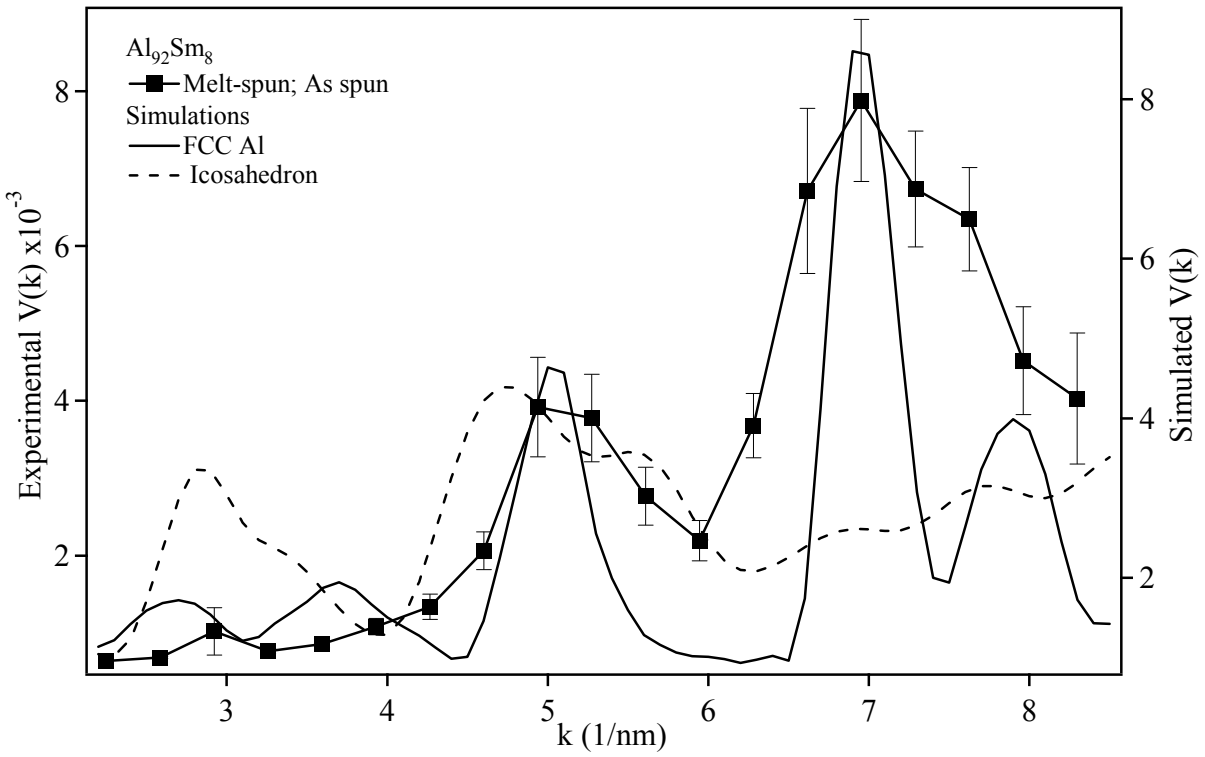

Figure 4.5 Measured $V(k)$ for melt-spun as spun and simulated $V(k)$ for a 30 Å Al sphere and a Sm-centered icosahedra. The Al sphere reproduces the peak positions and relative heights. The simulations have been multiplicatively scaled to match the data. Figure from [40].

substitutional Sm atoms match almost as well. This leads us to believe that slightly different crystal sizes, shapes, or orientation distributions are also likely to be broadly consistent with the data. The major requirement for the simulated $V(k)$ to be similar to the experimental $V(k)$ is for diffraction from some atomic spacing similar to FCC Al, which is spatially heterogeneous on a length scale of 1.6 nm, the spatial resolution of the imaging. The exact shape of the Al-like MRO is, to a first approximation, not as important as the interatomic planer spacing. This means

atoms locally organized into an FCC Al lattice should provide a similar $V(k)$, even if the structure is strained, distorted, or impure. Because of this distinction, we call this MRO "nanoscale Al-like order".

The structural origin of the peak at 3 nm^{-1} in the cold-rolled $V(k)$ is not clear. It is not an Al reflection, and while it could be an intermetallic or icosahedral reflection, simulations of those structures show peaks at higher k not seen in the data. Even if the type of MRO in the cold-rolled material is unknown, the fact that it is *drastically* different than the melt-spun MRO is important. The difference in the MRO and the devitrification results between these two processing techniques shows that the MRO measured is associated with primary crystallization.

4.04 MRO Changes in $Al_{92}Sm_8$ with Annealing

Our data support the model that primary crystallization in these alloys is driven by crystal-like Al clusters formed during the quench, then frozen into the structure [12,19,42]. As seen in Figure 4.4 with annealing at 40 ^{o}C below T_g, the melt-spun material shows a decrease in the degree of MRO ($V(k)$ peak magnitude decrease), while the type of MRO remains constant ($V(k)$ peak positions are unchanged). Even with annealing at this low temperature, some Al nanocrystals grow from the amorphous material [11,12]. A single large crystal in the field of view will dominate the $V(k)$ signal from the surrounding material, so we avoid them when making FEM measurements. That means that in the annealed samples, we measure the remaining population of nuclei, not the crystallized material.

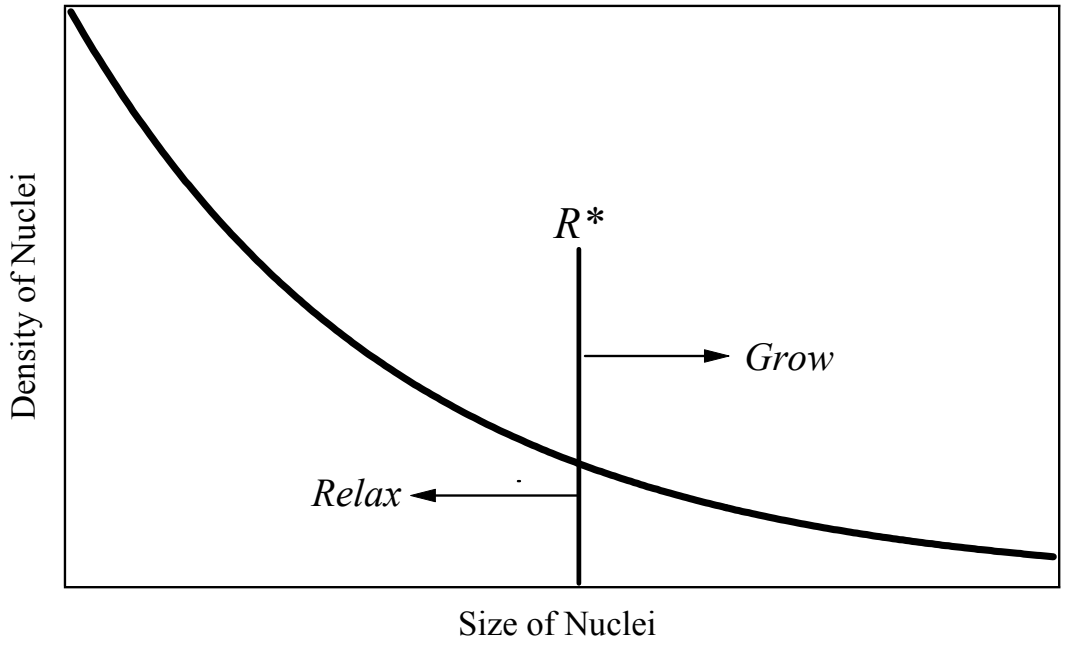

Figure 4.6: Schematic representation of biasing the FEM experiment upon annealing. When annealed, quenched-in nuclei smaller than the critical size (R*) will relax back into the amorphous matrix while those larger than R* will grow into visible crystals. Visible crystals are avoided with FEM experiments, therefore the FEM annealing experiments measure the subcritical nuclei relaxing back into the matrix.

Since we are avoiding the devitrified nanocrystals, we are biasing our sample for the nuclei that have yet to grow into noticeable crystals. Assuming a distribution of nuclei within the as quenched material, we are measuring the nuclei that are smaller than some critical size that grows into visible crystals with these annealing treatments. Since these sub-critical nuclei are below the critical size, they will relax back into the amorphous matrix. This is shown pictorially

in Figure 4.6. Still, this begs the question; If the sample is crystallizing, why do we measure *less* order?

We can model this change in $V(k)$ using the FEM theory [87] described in Chapter 2. Starting with nanocrystals aligned at the {220} Al Bragg reflection, we can see how the decreased $V(k)$ corresponds to the changed sample structure. Since we are biasing the sample by viewing a smaller number of nuclei by avoiding the crystals in the FEM measurements, the variables changing with the FEM theory are the size d and the volume fraction Φ.

Given that there is probably a distribution of nuclei in the melt-spun material, similar to what is seen in Figure 4.6, then as the subcritical nuclei relax back into the amorphous matrix, we could assume that both the size of the MRO is decreasing (decreasing d) and that the number of nuclei are decreasing both by the relaxing and by the biasing of the sample (decreasing Φ). This is seen schematically using the plots of $V(C_{220}\Phi)$ and $V(d)$ for Al spheres in Figure 4.7 and Figure 4.8.

Since there are two variables changing simultaneously, the interpretation of how the structure is changing complicated. As seen in Figure 4.7, decreasing Φ at constant d decreases V, if you are on the left of the relative maximum Φ_m. Recall from Section 2.07, we believe that the as quenched material has $\Phi \sim 0.2$, firmly to the right of Φ_m. The biasing of the sample could cause us to move to the other size of Φ_m, although, as Figure 4.9 demonstrates, it would take an order of magnitude decrease in the number density of nuclei (with a constant size of 1.6 nm) for this to occur. What is most likely occurring is since V is roughly proportional to d^6, the decreasing d will decrease V quite rapidly, as seen in Figure 4.8. Therefore the decreasing V is from a decrease in both Φ and d, with the decrease in d dominating the decreasing V. It may be

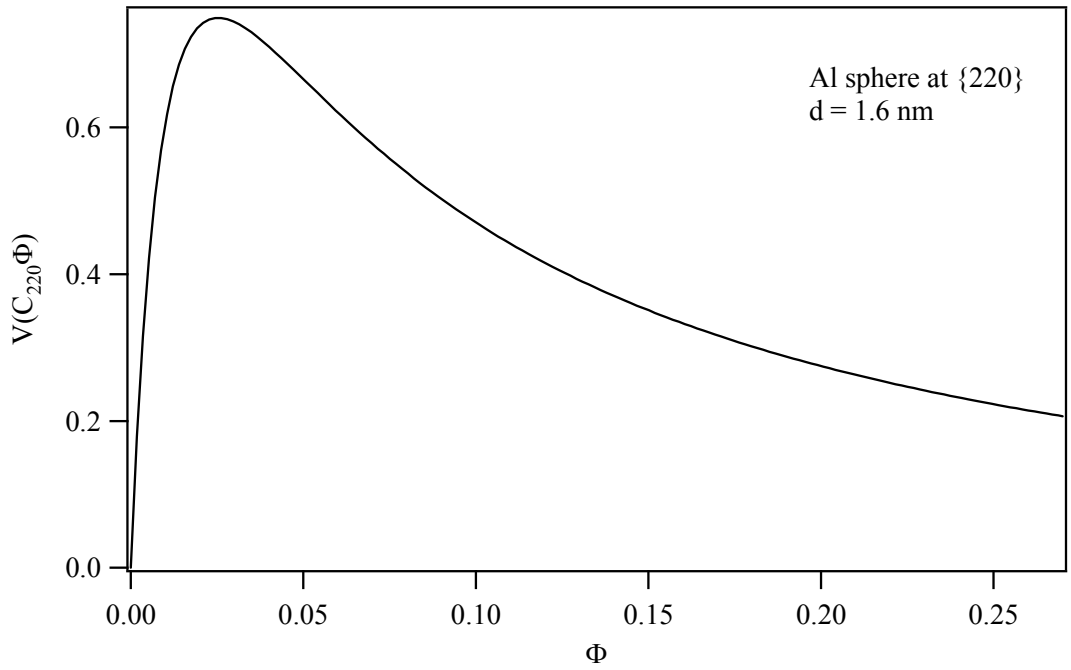

Figure 4.7 $V(A_{220}\Phi)$ for a 1.6 nm Al sphere using our FEM theory.

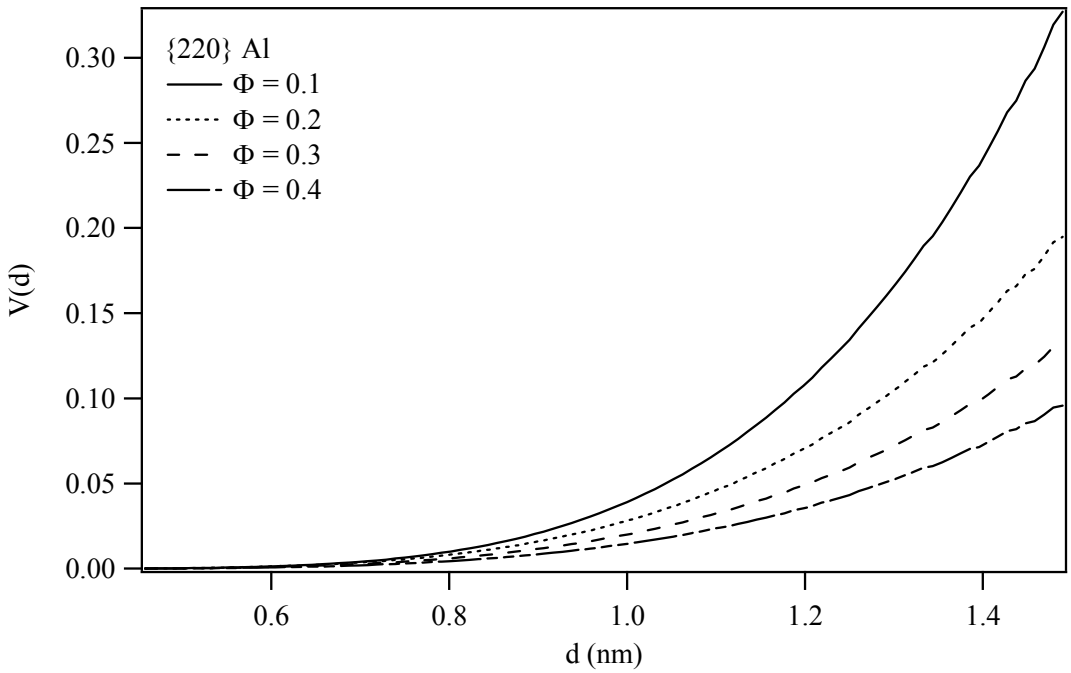

Figure 4.8 $V(d)$ for $\Phi = 0.2$ with a {220}Al sphere using the our FEM theory.

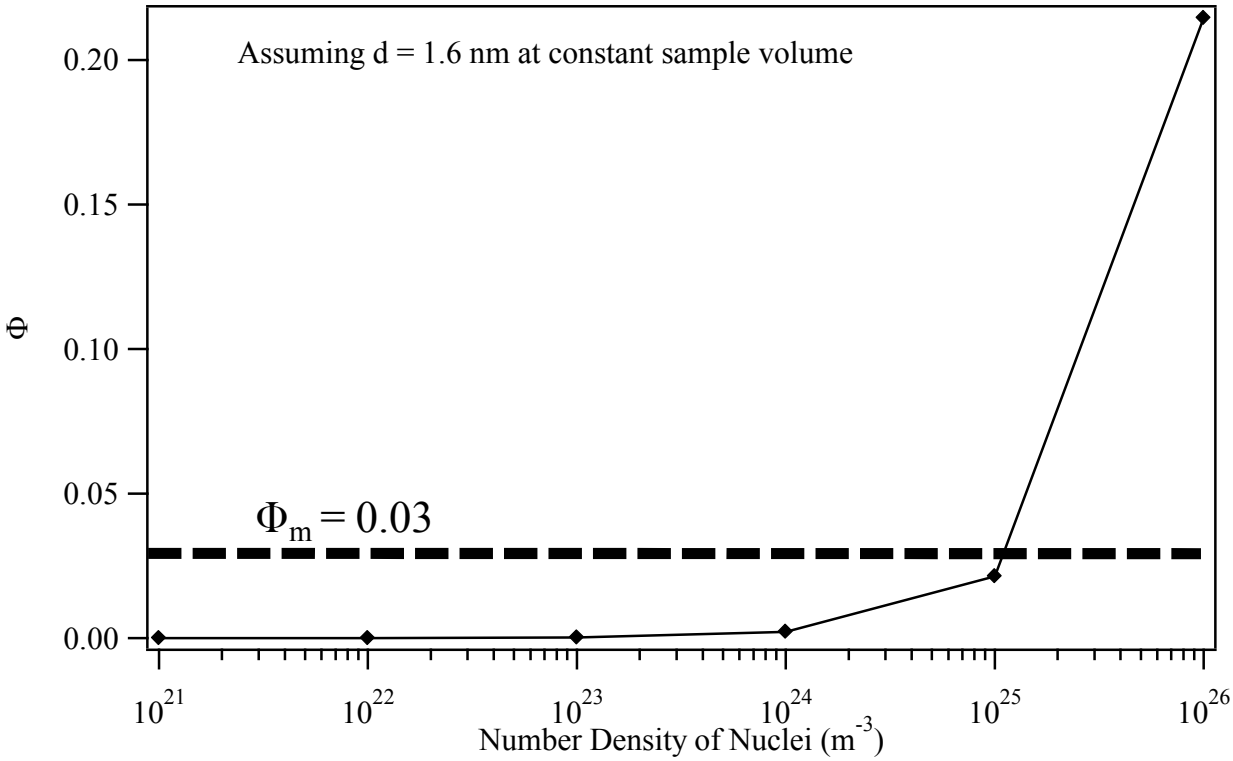

Figure 4.9 Plot of Φ versus number density of quenched-in nuclei assuming a sample volume of $(300\ nm)^2$ by 70 nm thick.

possible to separate these effects using the type of analysis presented n Section 5.04, although this has not been done.

As stated in Chapter 1 other hypotheses, besides quenched-in nuclei have been advanced to explain primary crystallization. Based on the bright field TEM images of the areas used in FEM, we see no evidence for amorphous phase separation [116]. Xing *et al.* have suggested that some high Al-content amorphous alloys amorphous / nanocrystal composites, and that primary

crystallization is grain coarsening, not a phase transition [45], implying a constant Φ upon annealing.

Our observation of nanoscale Al order in the as-spun ribbon is consistent with both grain coarsening and quenched-in nuclei. Unfortunately, even with application of the FEM theory, we cannot distinguish between which of these two mechanisms are responsible for primary crystallization. With the biasing of the measurements, which decreases d and Φ regardless if the overall Φ is constant, we would still see a decrease in V.

4.05 Summary

The FEM experiments showed a *drastically* different type of MRO in the melt-spun versus the cold-rolled material. Using computer simulations we identified the MRO in the melt-spun material as Al-like, meaning the MRO had similar atomic pair spacings to FCC Al. The MRO in the cold-rolled material was not Al-like. The decreasing $V(k)$ with annealing was found to be consistent with the quenched-in nuclei hypothesis for devitrification of these materials using our new FEM theory . Based on these results, FEM is sensitive to the structural precursor responsible for the devitrification behavior in high Al-content amorphous alloys.

Chapter 5.

$Al_{88}Y_7Fe_5$ and $Al_{88}Y_7Fe_4Cu_1$

This section contains material to be submitted for publication as
W.G. Stratton et al., Acta Materialla, to be submitted

The characterization of Al-like MRO associated with the devitrification reaction in $Al_{92}Sm_8$ implied the presence of a structural precursor to crystallization formed by the rapid quench processing. To understand if this type of MRO is a universal feature in this class of materials, we investigated the MRO the high Al-content amorphous alloy, $Al_{88}Y_7Fe_5$. This composition is considered a better glass former, mainly because it is easier to make the amorphous ribbon in the lab.

$V(k)$ for $Al_{88}Y_7Fe_5$ in Figure 5.1 is different than $V(k)$ for $Al_{92}Sm_8$. $Al_{88}Y_7Fe_5$ shows peaks at the {200} and {220} reflections like $Al_{92}Sm_8$ – but it also shows the {111} reflection. Why does one high Al-content amorphous alloy have a different type of MRO than another, especially when the two alloys are so close in composition to pure Al? The structural picture we see occurring is that the MRO within the $Al_{88}Y_7Fe_5$ is closer to a true Al crystal structure than $Al_{92}Sm_8$.

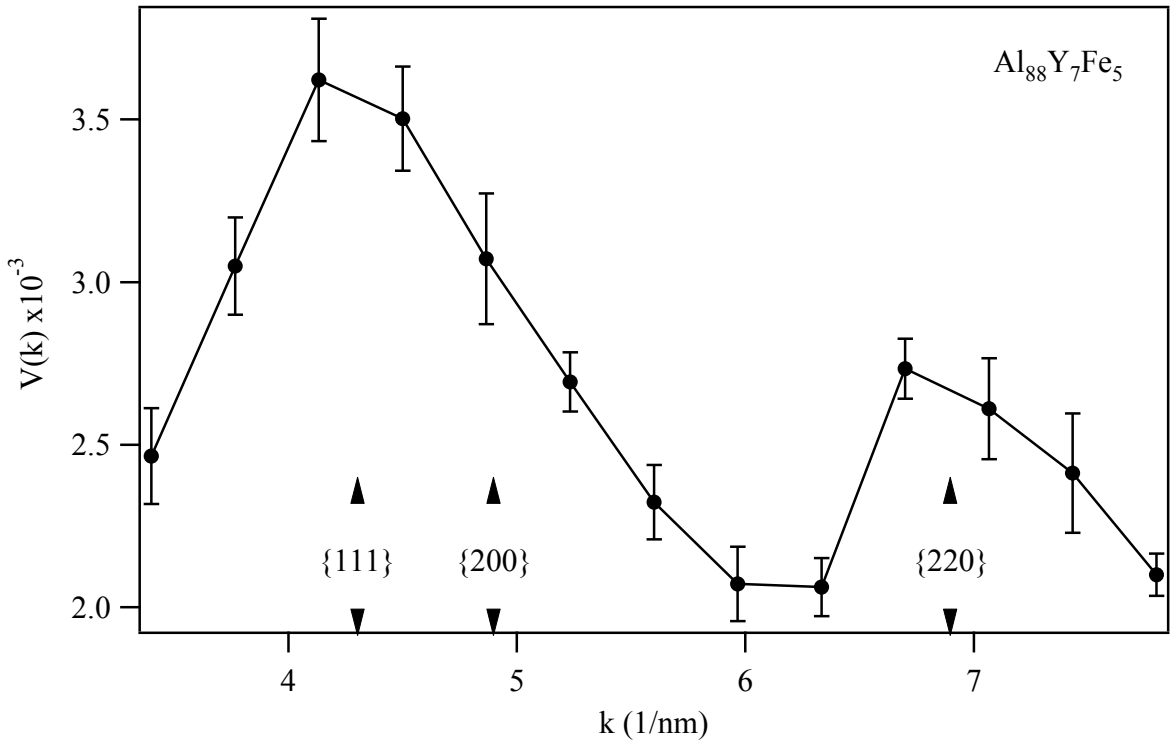

Figure 5.1: $V(k)$ for $Al_{88}Y_7Fe_5$ with Al Bragg reflections noted as arrows.

When FCC Al begins forming from the melt, the first neighbors formed are the nearest neighbor distance, or the cross face of the FCC unit cell, the [220] direction. As the crystal grows, the next neighbor distance will be in the [200] direction. For two neighboring {200} distances, there will be 24 {220} neighbor distances. This trend continues as the number of atoms reaches the size needed to find {111} neighbor distances. Therefore until the crystal reaches a size where multiple {111} planes are formed, the most prevalent atomic spacing will be the {220} spacing. Once the crystal gets large enough so that close packed {111} planes become the dominant

diffracting condition through the multiplicity and the atomic scattering factor (see the diffracted intensity equation in Chapter 2), then it will become obvious in both the diffraction and *V* data. This effect is shown schematically in Figure 5.2. Starting with a single 1 nm FCC Al crystal shown at the {111} and {220} reflections, we compare how removal of atoms changes these atomic planes. As more atoms are randomly removed (simulating the transition from crystal to MRO), the {111} planes are much more sensitive to the disorder/removal of planes than the {220}. After 30% of the atoms are removed the {220} planes appear to barely be modified, while the {111} planes are almost unrecognizable. Therefore, we conclude that $Al_{92}Sm_8$ has less complete Al-like order because of the strong {220} reflection, while $Al_{88}Y_7Fe_5$ has more complete Al-like order because of the presence of the {111} reflection. This arrangement relates only to the pseudo-atomic plane spacing, and makes no claim about on changes to the relative size of the MRO.

5.01 Microalloying $Al_{88}Y_7Fe_5$ with Cu

$Al_{92}Sm_8$ and $Al_{88}Y_7Fe_5$ both have Al-like MRO that we associate with the devitrification reaction of the rapidly quenched material. What happens to the structure with subtle chemical additions? As discussed in Chapter 1, substitution of 0.5 atomic % Ti for Al in $Al_{88}Y_7Fe_5$ changes the amorphous structure, drastically reducing the density of Al nanocrystals after devitrification and increasing the onset temperature of primary crystallization [45]. Substitution of 1 atomic % Cu for Ni in $Al_{88}N_7Sm_5$ [47] and 1% Cu for Al or Ni in $Al_{88}Y_4Ni_8$ [48], drastically

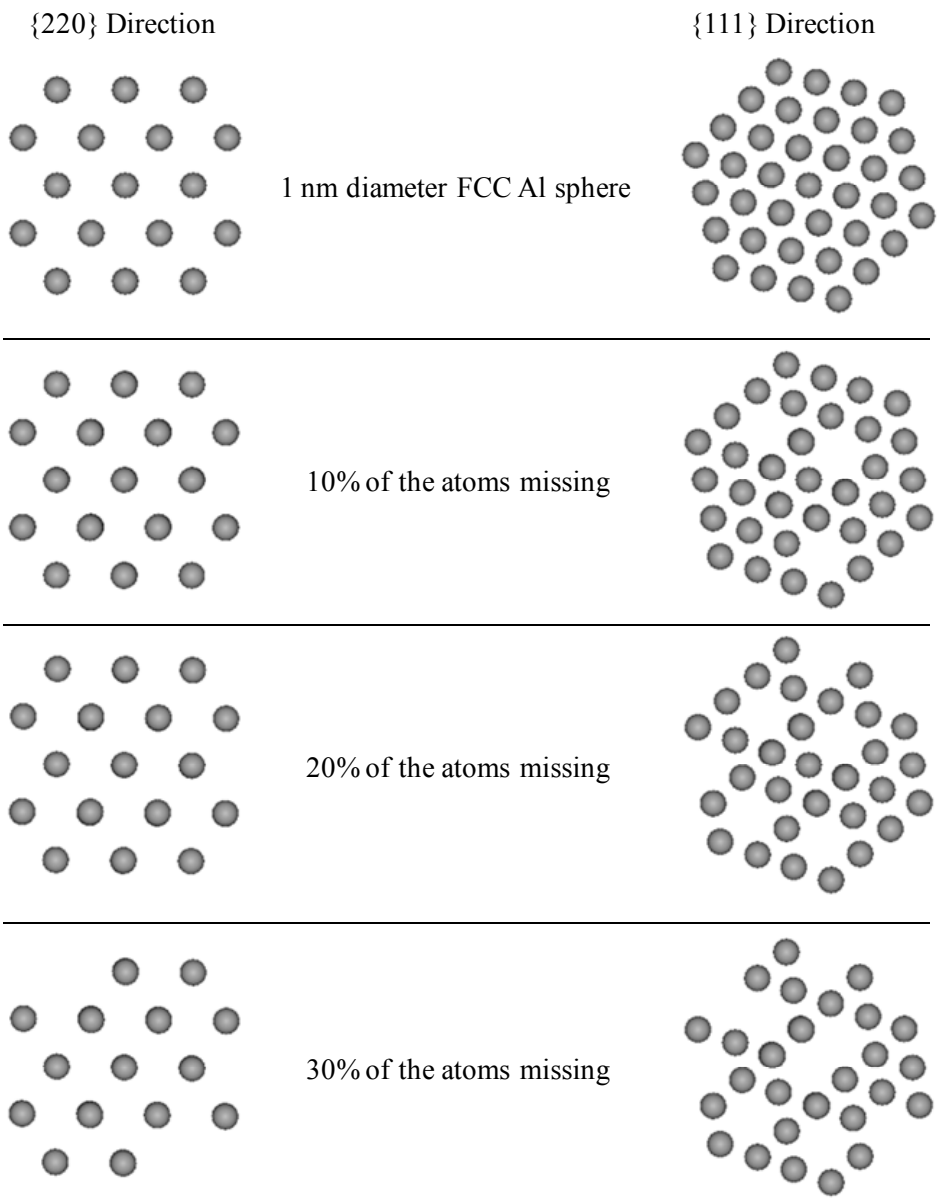

Figure 5.2: Schematic representation of a 1 nm FCC Al crystal at different orientations, showing how $Al_{92}Sm_8$ and $Al_{88}Y_7Fe_5$ can both have Al-like MRO while having different $V(k)$. As atoms are removed from the 1 nm FCC Al crystal, the {111} planes becomes less distinct, while the {220} planes basically remain intact. This shows how {220} planes are more 'robust' to small changes in the crystal, compared to {111} planes.

increases the number of Al nanocrystals, decreases their size, and depresses the onset of primary crystallization. Is this change due to the initial structure or some other mechanism?

Microalloying induced changes to the onset of primary crystallization (T_x) are measured by DSC and are usually due to a change in the nucleation rate *J*. In classical nucleation theory [6],

$$J = \omega C_0 \exp\left[-\frac{\Delta G^* + \Delta G_m}{kT}\right], \tag{5.1}$$

where ω is a factor that includes the vibration frequency of the atoms and the area of the critical nucleus, C_o is the number density of quenched-in nuclei, ΔG^* is the activation energy barrier for crystallization, ΔG_m is the activation energy for atomic migration per atom, k is the Boltzmann constant, and T is the temperature. To change the nucleation rate without major changes in structure or composition, one of two factors must change: C_o or ΔG^*. C_o is the number density of precursors to nucleation, so microalloying that changes the density and size of these precursors will affect *J* and therefore the DSC trace. Control of the devitrified structure therefore requires control and understanding of the nanoscale structure and thus the precursors to crystallization.

Comparing $Al_{88}Y_7Fe_5$ and $Al_{88}Y_7Fe_4Cu_1$ using DSC, the devitrified microstructure, and FEM, gives complimentary information telling us what is occurring to the structure of the material with the addition of Cu. Taken together, these thermokinetic, microstructural, and nanostructural results show that the increase in nanocrystal density in $Al_{88}Y_7Fe_5$ with the 1% addition of Cu for Fe is due to an increased number of nanoscale precursor nucleation sites (C_o) within the structure of the rapidly quenched materials.

5.02 Experimental Addendum

DSC measurements were done in a Perkin-Elmer Powercompensator DSC 7 at a heating rate of 20 ^{o}C/min. Partially crystallized samples were made by annealing the material in air for 1 hour; $Al_{88}Y_7Fe_5$ samples were annealed at 245 ^{o}C; $Al_{88}Y_7Fe_4Cu_1$ at 170 ^{o}C. These temperatures were chosen so that the resulting devitrified nanocrystals were circular and had no dendritic growth. Nanocrystal size measurements were done by tilted dark-field TEM on a CM200 at 200 kV. The $Al_{88}Y_7Fe_4Cu_1$ nanocrystal data comes from an estimated volume of 0.05 μm^3, while $Al_{88}Y_7Fe_5$ nanocrystal data comes from an estimated volume of 0.1 μm^3 to get better counting statistics, due to the low number of devitrified crystals. We assumed a 70 nm sample thickness as typical [117], as it is not possible to measure it by bright field transmittance due to strong crystal diffraction. For each area, four dark field images at different azimuths on the Al diffraction ring were acquired. For thinned amorphous specimens, bulk x-ray diffraction and thinned sample transmission electron diffraction showed peaks at the same momentum transfer indicating little, if any, change in the SRO on thinning for the TEM.

Particle size analysis was done using Image Pro-Plus software. We did not use the normalized histogram (seen in Figure 5.3) to analyze the particle size distributions, since there is ambiguity recording the proper bin size is required to construct the histogram [32]. One can bias the data by choosing a bin size that is too large or too small. Bin sizes that are

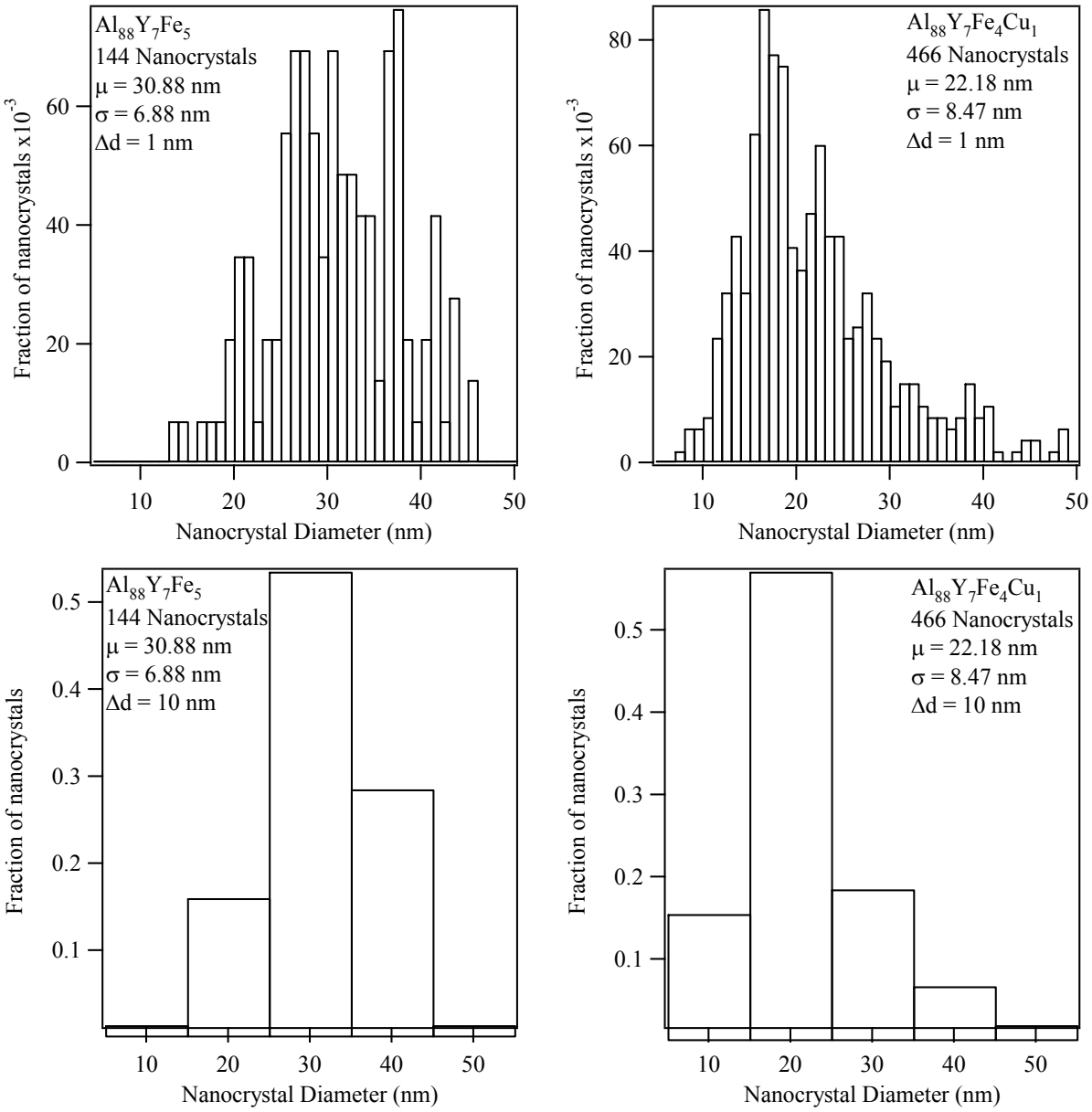

Figure 5.3: Normalized histograms for the nanocrystallization distributions in $Al_{88}Y_7Fe_5$ (1 hour at 245 ^oC) and $Al_{88}Y_7Fe_4Cu_1$ (1 hour at 170 ^oC). The each data set shows multiple peaks in the small bin size, while the large bin size shows only one. This ambiguity is resolved by using the CDF and PDF.

too large may miss fine features in the distribution, while bin sizes that are too small may give create peaks in the histogram that are statistically insignificant. To eliminate this problem, we use the raw data to calculate the cumulative distribution function (CDF) which describes the probability distribution of a real-valued random variable, which in our case is the probability of finding a nanocrystal of a certain size or smaller, versus the nanocrystal size [32]. The derivative of the CDF is the probability density function (PDF), which gives the probability of a crystal having a certain diameter. This is a continuous function that provides the same information as a normalized histogram, but is not subject to binning problems [32]. To calculate the PDF from our data, we fit our raw CDF data to a Boltzmann sigmoidal curve,

$$y = G_2 + \frac{G_1 - G_2}{1 + \exp\left\{\frac{x - x_o}{dx}\right\}}, \tag{5.1}$$

where G_1 and G_2 are the asymptotic values to the left and right respectively, x_o is the point of inflection, and dx controls the curvature term. The PDF is found by taking the derivative of our fit CDF data. The mean and standard deviations were estimated directly from the measured sizes using conventional formulas.

5.03 $Al_{88}Y_7Fe_4Cu_1$ Results

The DSC results for $Al_{88}Y_7Fe_5$ and $Al_{88}Y_7Fe_4Cu_1$ in Figure 5.4 show that the addition of Cu depresses the onset of primary crystallization by approximately 60 ^oC, from 280 ^oC to 220 ^oC.

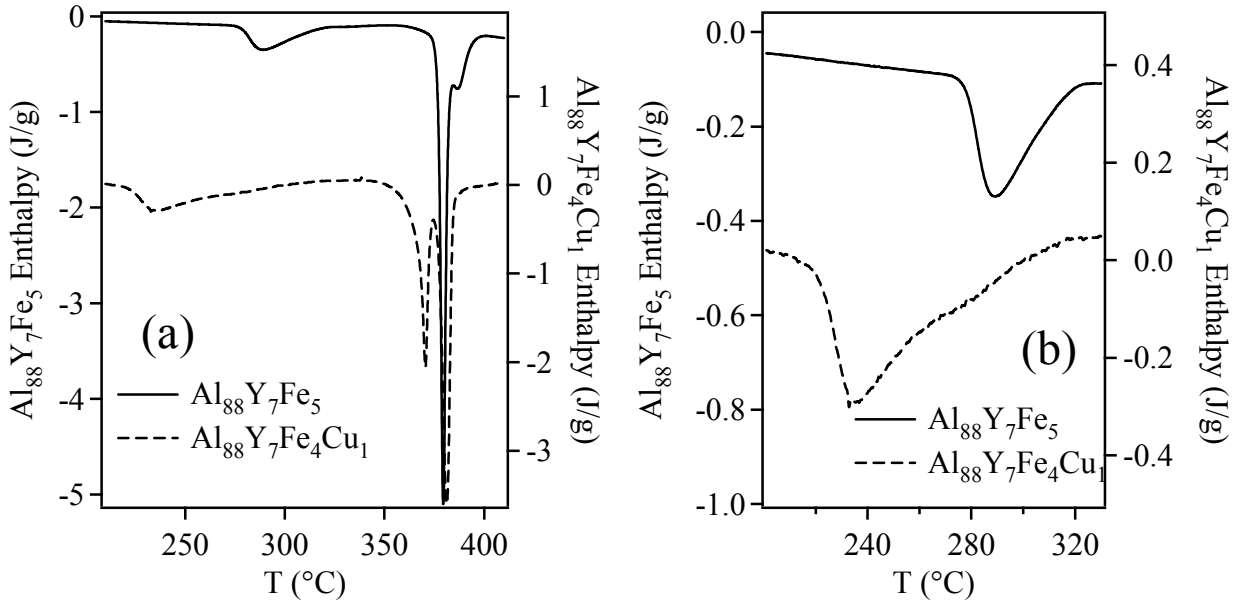

Figure 5.4: DSC data for $Al_{88}Y_7Fe_5$ and $Al_{88}Y_7Fe_4Cu_1$. The small substitution of Cu depresses the onset of primary crystallization by 58 ^oC. Plot (b) is an inset of plot (a) showing Tx. Data courtesy of Dr. Hamann, UW graduate.

The CDF and PDF of the devitrified nanocrystal distribution are shown in Figure 5.5. The fit parameters for the Boltzmann sigmodial fit and crystallization statistics are summarized in Table 1. Cu microalloying increases the density of nanocrystals fourfold and decreases their average size by 50%. $Al_{88}Y_7Fe_4Cu_1$ has roughly 1.5 times more crystal volume fraction than $Al_{88}Y_7Fe_5$, assuming that the thicknesses of the two samples were similar and ignoring any effects of the 2-D projection inherent to TEM imaging.

The results in Figure 5.5 should be relatively insensitive to the details of the annealing. This is because the nanocrystals in Figure 5.6 are compact and nearly spherical with no

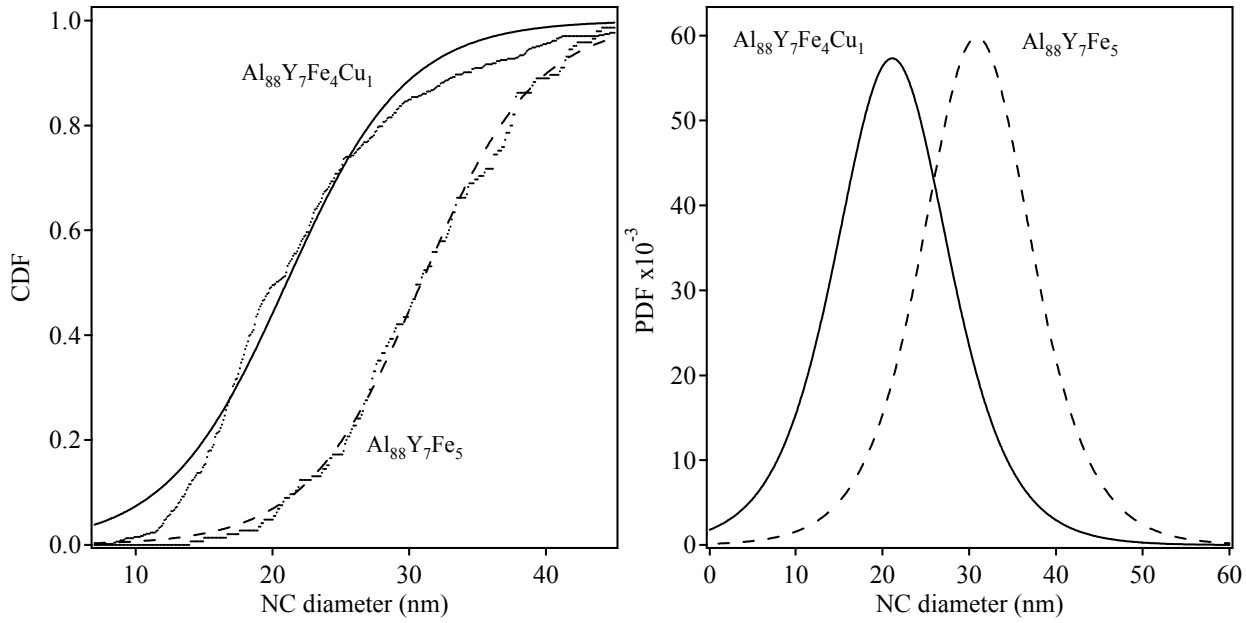

Figure 5.5: CDF and PDF for $Al_{88}Y_7Fe_5$ annealed for 1 hour in air at 170 ^oC and $Al_{88}Y_7Fe_4Cu_1$ annealed for 1 hour in air at 245 ^oC. $Al_{88}Y_7Fe_4Cu_1$ had approximately four times as many nanocrystals as $Al_{88}Y_7Fe_5$. Data for the CDF calculation is seen as points, fits to both sets of data are seen as solid or broken lines.

Boltzmann Sigmoidal Values

	$Al_{88}Y_7Fe_5$	$Al_{88}Y_7Fe_4Cu_1$
G1	1.4×10^{-9}	1.8×10^{-9}
G2	1	1
xo	30.9	21.0
dx	4.2	4.4
χ^2 value	0.13	0.72

Table 5.1: Boltzmann sigmoidal equation constants for data in Figure 5.5.

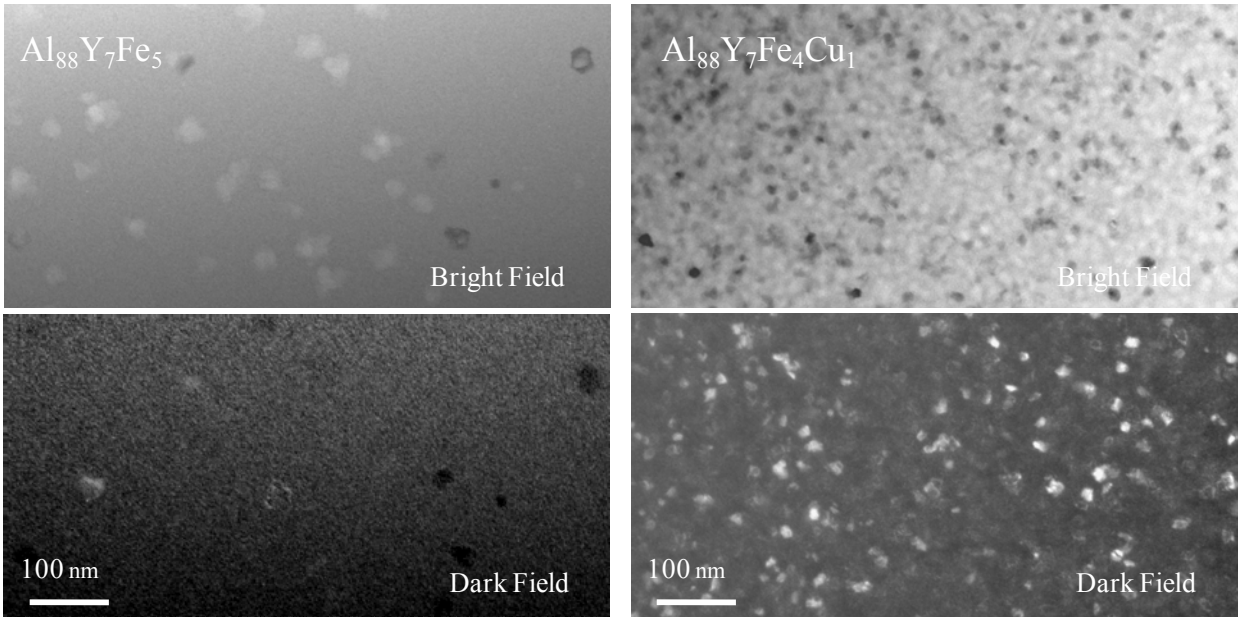

Figure 5.6: Bright field and matching dark field micrographs of devitrified $Al_{88}Y_7Fe_5$ (170 ^oC for 1 hour) and $Al_{88}Y_7Fe_4Cu_1$ (245 ^oC for 1 hour).

dendrites, therefore we have we halted crystallization at an initial growth stage where Al is moving into the nanocrystal and solute elements are being ejected from the growing nanocrystal. This stage continues until a layer of the solute elements surrounds the nanocrystal, arresting the initial growth stage. The first crystallization step is quick, and will preserve the number density of supercritical nuclei as grown nanocrystals. Since we think these amorphous alloys crystallize by a growth mechanism alone [25], and since we see basically spherical nanocrystals, we conclude that these results are a reflection of the increased number of supercritical nucleation sites (similar to C_o) in the rapidly quenched amorphous alloy with the addition of Cu.

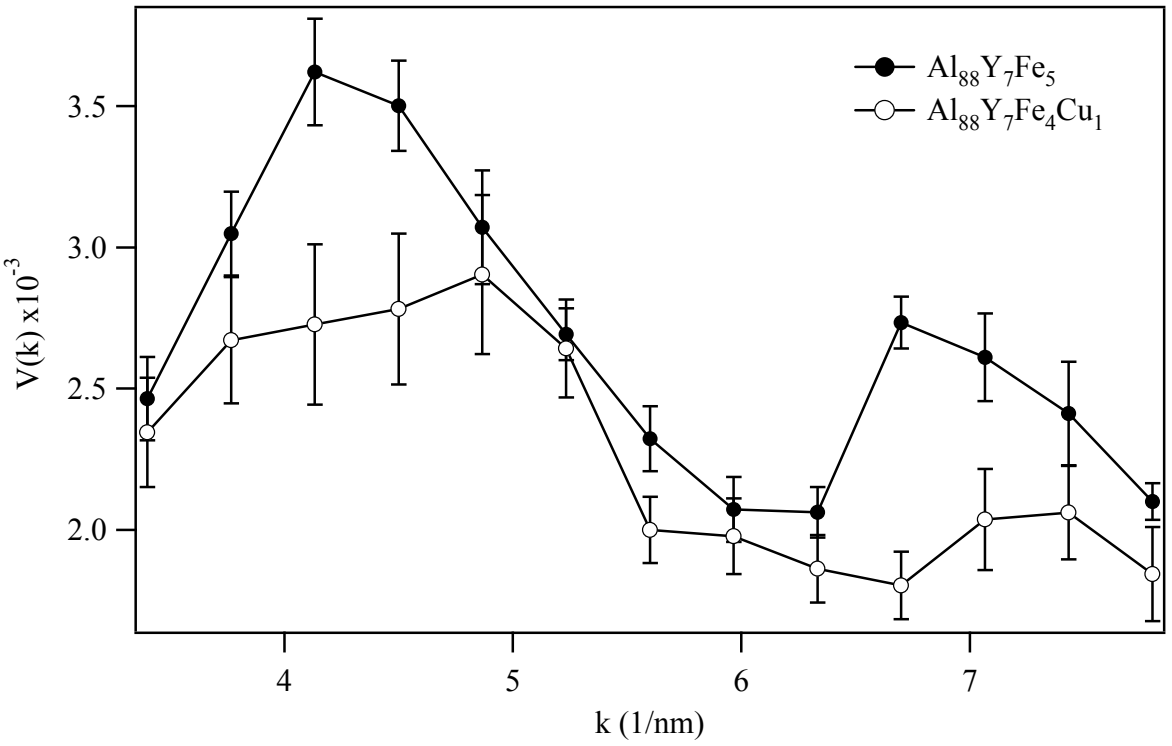

Figure 5.7: FEM data for $Al_{88}Y_7Fe_5$ and $Al_{88}Y_7Fe_4Cu_1$ at 1.6 nm spatial resolution. The peak positions occur at the listed Al Bragg reflections. The lower peaks in $Al_{88}Y_7Fe_4Cu_1$ indicate a more spatially homogeneous structure at a length scale of 1.6 nm.

The FEM results in Figure 5.7 show that peaks in $V(k)$ for $Al_{88}Y_7Fe_5$ and $Al_{88}Y_7Fe_4Cu_1$ occur at Al Bragg reflections, again indicating we are measuring a form of Al-like MRO. $Al_{88}Y_7Fe_4Cu_1$ has a decreased $V(k)$at $\langle 111 \rangle$ and $\langle 220 \rangle$ positions, but not the $\langle 200 \rangle$ position compared to $Al_{88}Y_7Fe_5$, indicating that Cu substitutions make the amorphous structure more homogeneous.

5.04 $Al_{88}Y_7Fe_4Cu_1$ Discussion

The devitrified microstructure, DSC, and FEM measurements form a consistent picture of the changes induced by Cu substitution. The DSC results show an increase in the nucleation rate. This results in a higher density of nanocrystals after devitrification, as shown by the distributions in Figure 5.5. Those distributions also show that the nanocrystals are smaller. These results are connected by the FEM structural data on the as-quenched material, which is consistent with an increased density of quenched-in nuclei.

The FEM results of Figure 5.7 and FEM theory from Chapter 2 can give insight to the initial structure of these materials. The FEM data in Figure 5.7 covers 3 Al Bragg peaks ({111}, {200}, and {220}) with different C_{hkl}'s: C_{111} = 0.47 nm, C_{200} = 0.30 nm and C_{220} = 0.43 nm. Assuming a constant thickness of 70 nm for all samples all the other factors are known, so this gives us 3 equations with two unknowns, d and Φ. These equations are solved graphically in Figure 5.8, which shows plot d and Φ contours for the experimental V at each Al Bragg reflection. For the {111} and {220} Al Bragg reflections, there is a relatively constant shift to smaller d and larger Φ with the addition of Cu. This almost identical shifting of the d, Φ curve for {111} and {220} is certainly due to those reflections having a similar Bragg active fraction constants, and a similar change in V with the Cu addition. If we look at this shift alone, it corresponds to a decrease in d and an increase in Φ.

The {200} and {220} reflections have significantly different C_{hkl}, and those contours intersect for both compositions, enabling us to extract an estimate for d and Φ. We estimate that

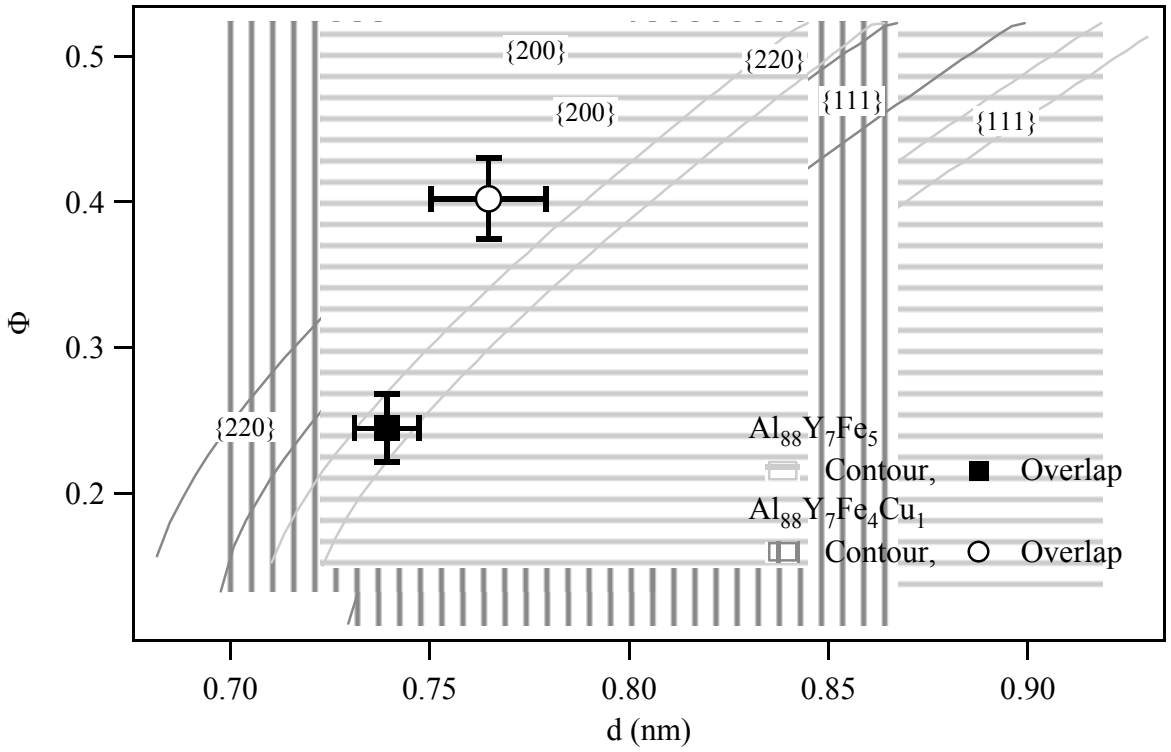

Figure 5.8: Φ versus d for $V_{experiment}$ for $Al_{88}Y_7Fe_5$ (horizontal line fill) and $Al_{88}Y_7Fe_4Cu_1$ (vertical line fill). Contours at Al {200} and {220} intersect, allowing us to extract an estimate for Φ and d. The addition of Cu increases Φ by 60% with no statistical change to d.

$Al_{88}Y_7Fe_5$ has $d = 0.74 \pm 0.01$ nm, $\Phi = 0.25$ +/- 0.02 while $Al_{88}Y_7Fe_4Cu_1$ has $d = 0.77$ +/- 0.02 nm, $\Phi = 0.41$ +/- 0.03. The uncertainties are calculated from the error bars of V, but are too small (especially for d) to have any real physical meaning. These calculated sample parameters lead to a number density of Al-like MRO regions of 1.2×10^{26} m^{-3} for $Al_{88}Y_7Fe_5$ and 1.7×10^{27} m^{-3} for and $Al_{88}Y_7Fe_4Cu_1$. These values are larger than values in devitrified measurements, since

FEM is sensitive to both critical and subcritical nuclei, while the devitrified measurements are only sensitive to the sized quenched-in nuclei greater than the critical size. Overall, there is no statistical difference in d for $Al_{88}Y_7Fe_5$ and $Al_{88}Y_7Fe_4Cu_1$, but we see a 60% increase in Φ with Cu microalloying, consistent with the devitrification results.

The FEM theory predicts that a single combination of d, Φ that would create the $V(k)$ peaks, so why don't all the curves in Figure 5.8 cross at a single point? There are a number of possibilities. First, C_{111} and C_{220} are very similar, so there is only a small difference in the slope of the contours. Second, there may be some difficulty separating the contributions from the {111} and {200} Bragg reflections. The reciprocal space resolution of $V(k)$ is necessarily limited by the objective aperture size. We attempted to fit Gaussian peaks centered on the reflections, as has been done previously [67,118], but the fit had too many free parameters compared to the number of data points to be useful, and the number of data points is limited by electron beam exposure time. Finally, as discussed in Chapter 1, when FEM is done in a TEM as in this experiment it suffers from a partially coherent imaging mode, which decreases our sensitivity to the diffracted intensity from MRO, therefore producing a lower V when compared to V from FEM done more coherently (with a STEM or in computer simulations) [84]. A higher V value would shift the contours to higher d and slightly lower Φ. Coherence is an instrument issue, not a sample issue, so relative peak heights in V are conserved regardless of the electron beam coherence [84]. As a result, we conclude that the changes in V between $Al_{88}Y_7Fe_5$ and $Al_{88}Y_7Fe_4Cu_1$ are real and that Cu microalloying increases the Φ of the system.

The two hypotheses for the devitrification of high Al-content amorphous alloys make different predications for the behavior of Φ with crystallization, so we compared the calculated

Φ from the FEM theory and the Φ from the micrographs in Figure 5.6 to figure out which mechanism is occurring. Taking into account the C_{hkl} values of the devitrified nanocrystals (where the dominating factor is the size of the large objective aperture, rather than the shape function of the crystals) and that the method to acquire the dark field images only captured ~ 70% of the diffraction pattern, we calculate a devitrified volume fraction Φ_d of approximately 0.3 and 0.70 for $Al_{88}Y_7Fe_5$ and $Al_{88}Y_7Fe_4Cu_1$, respectively from images like Figure 5.6. These values are both larger than the FEM values, Φ = 0.25 +/- 0.02 and Φ = 0.41 +/- 0.03 $Al_{88}Y_7Fe_5$ and $Al_{88}Y_7Fe_4Cu_1$ respectively. Given the high density of nanocrystals there has to be some overlap that is not taken into account with this calculation, so the calculated Φ_d must be an underestimate. This means that since our calculated Φ *is less than* Φ_d there *must* be an increase in Φ upon devitrification. Since grain coarsening requires that the volume fraction stay constant through Al nanocrystal devitrification, we conclude that the mechanism for devitrification is growth of quenched-in nuclei.

The structural story we see occurring in this system is microalloying of Cu with the Al, Y, and Fe to increase the number of quenched-in nuclei, while perhaps decreasing their size. The devitrification results point to an increase in the number and a decrease in the size of the quenched-in nuclei given the devitrified crystals decreased average size. Our FEM data supports the increase in the number but shows no change in the size of quenched-in nuclei outside the experimental uncertainty. So at this point we can only conclude that Cu microalloying increases the number of precursor nucleation sites in the as quenched $Al_{88}Y_7Fe_4Cu_1$ material compared to $Al_{88}Y_7Fe_5$. Given that the devitrified microstructure in other high Al-content amorphous alloys are not all the same[45,47,48], we suggest that microalloying with an element that alters the

devitrified structure has the possibility of changing both the amorphous nanoscale structure and the thermodynamics of the material.

5.05 Summary

The addition of 1% Cu for Fe in $Al_{88}Y_7Fe_5$ changes the amorphous structure by increasing the number of quenched-in nuclei in the as quenched state. DSC results show a 60 ^oC depression in T_x of $Al_{88}Y_7Fe_4Cu_1$ compared to $Al_{88}Y_7Fe_4Cu_1$, indicative of an enhanced J caused by an increased C_o. The devitrified structure of $Al_{88}Y_7Fe_4Cu_1$ shows a drastic increase in the number density of Al nanocrystals, with a decrease in their average size compared to $Al_{88}Y_7Fe_5$ implying an increased number of precursor sites to crystal growth. FEM results confirm this result by showing that the type of MRO is preserved with the addition of Cu, but the overall V decreases with this addition. Using our FEM theory, we see this change in V is consistent with an increase of 60% of the volume fraction of MRO in the rapidly quenched amorphous material. We see an *increase* in Φ upon crystallization, indicating that the devitrification mechanism is growth of quenched-in nuclei.

Chapter 6.

Conclusions

Taken together, the results in Chapters 4 and 5, interpreted according to the theory in Chapter 2, imply the formation of Al-like nanoscale structural precursors to crystallization during the rapid quench of high Al-content amorphous alloys. Processing experiments on $Al_{92}Sm_8$ showed Al-like medium-range structure associated with the rapidly quenched amorphous material, and a different structure with the deformation induced amorphous material (Sections 4.02 and 4.03). Rapidly quenched $Al_{88}Y_7Fe_5$ and $Al_{88}Y_7Fe_4Cu_1$ have a similar type of Al-like MRO (Sections 5.01 and 5.03). Since the rapidly quenched material devitrifies to a high density of pure Al nanocrystals while the deformation induced amorphous material does not, we conclude the MRO measured with FEM in rapidly quenched $Al_{92}Sm_8$ is associated with the devitrification reaction (Section 4.02).

The results that FEM measured Al-like MRO is associated with the devitrification reaction is not enough by itself to distinguish between growth of quenched-in nuclei grain coarsening in primary crystallization. The evidence for quenched-in nuclei is the change in the volume fraction with devitrification. Chapter 5 shows an increase in the crystalline volume

fraction between the as quenched material and the partially devitrified material of $Al_{88}Y_7Fe_5$ and $Al_{88}Y_7Fe_4Cu_1$ (Section 5.04). Grain coarsening requires a constant crystalline volume fraction of throughout primary crystallization, while quenched-in nuclei assumes that the crystalline volume fraction of must increase upon devitrification.

The results presented here support the quenched-in nuclei hypothesis for high Al-content amorphous alloy formation and devitrification. FEM measurements on $Al_{88}Y_7Fe_5$ alloyed with Cu (Section 5.03) and annealing experiments on $Al_{92}Sm_8$ (Section 4.04) showed structural changes in the as quenched material (as modeled using our FEM theory in Chapter 2) that are consistent with the associated devitrification reaction changes. We draw two conclusions from these results; first that FEM is sensitive enough to note subtle changes in the amorphous structure of these materials. Second, and more importantly, it shows the value of the new FEM theory (Chapter 2). This research has provided a means to connect changes in V to changes in the amorphous structure.

This work found Al-like MRO in multiple high Al-content amorphous alloys. Plus Al-like MRO measured by FEM has been found in other compositions by other researchers [119,120]. Given that each high Al-content amorphous alloy characterized by FEM to date has found Al-like MRO, we conclude that Al-like MRO may be a universal feature in the rapidly quenched high Al-content amorphous alloys. Further work on characterization of high Al-content amorphous alloys should help support this finding.

6.01 Future Work

With the addition of the new STEM to the University of Wisconsin, there is an excellent opportunity for future work on the characterization of high Al-content amorphous alloys. First, the problems with electropolishing of Ni containing high Al-content amorphous alloys (Chapter 3) should be explored using high resolution EELS and EDS. By tracking changes in the SRO with chemical changes we can determine if electropolishing preferentially removes Al, pushing the composition of the alloy toward an intermetallic composition like Al_3Ni, or if something else happening. Once we understand what is taking place structurally, we can tailor the sample preparation technique accordingly in order to make samples appropriate for FEM. This would increase the number of compositions available for FEM analysis to fully determine if Al-like MRO is truly a universal feature in these materials.

Furthermore, the new STEM will have the capability for VR FEM with a coherent probe. The TEM FEM experiments were done with a partially coherent probe, which depresses V. Application of the FEM theory to V obtained under coherent conditions will provide more accurate results on the calculated size and volume fraction of MRO in Chapter 5. Also, VR FEM experiments provide structural information at varying length scales, which would be another check to determine the characteristic size of the MRO in the material.

Lastly, more computer simulations could be preformed to give insight beyond "Al-like" to describe the medium-range structure. Reverse Monte Carlo simulations [61-63] on high Al-content amorphous alloys using V along with other constraints (structure factor, coordination

number, etc.) can give insight to the MRO structure and how it changes with processing or microalloying.

References

1. Ossi, P. M. *Disordered Materials An Introduction* (Springer, Berlin, 2003).
2. Frank, F. C. Supercooling of liquids. *Proc. Roy. Soc. Lond. A* **215**, 43-46 (1952).
3. Cahn, R. W. in *Materials Science and Technology* (ed. Zarzycki, J.) 495-548 (VCH, Weinheim, 1991).
4. Callister, W. D. *Materials Science and Engineering: An Introduction* (John Wiley and Sons, New York, 2000).
5. Zarzycki, J. (ed.) *Glasses and Amorphous Materials* (VCH, New York, 1991).
6. Porter, D. A. & Easterling, K. E. *Phase Transformations in Metals and Alloys* (CRC Press, Boca Raton, FL, 2004).
7. Wu, R. I. in *Materials Science and Engineering* (University of Wisconsin, Madison, 2001).
8. Luborsky, F. E. (ed.) *Amorphous Metallic Alloys* (Buytterworth and Co. Ltd., London, 1983).
9. Chiang, Y., Birnie, D. & Kingery, W. D. *Physical Ceramics: Principles for Ceramic Science and Engineering* (John Wiley and Sons, New York, 1997).
10. Angell, C. A. Formation of Glasses from Liquids and Biopolymers. *Science* **267** (1995).
11. Wilde, G. et al. Early stages of Al-nanocrystal formation in $Al_{92}Sm_8$. *Mat. Res. Symp. Pro.* **806**, 33-38 (2003).
12. Wilde, G., Sieber, H. & Perepezko, J. H. Glass Formation Versus Nanocrystallization in an $Al_{92}Sm_8$ Alloy. *Scripta Mat.* **40**, 779 (1999).
13. Klement, W., Willens, R. H. & Duwez, P. Non-crystalline structure in solidified gold-silicon alloys. *Nature* **187**, 869-870 (1960).
14. Inoue, A. Stabilization of metallic supercooled liquid and bulk amorphous alloys. *Acta Mater.* **48**, 279-306 (2000).
15. Inoue, A. Amorphous, nanoquasicrystalline and nanocrystalline alloys in Al-based systems. *Prog. Mat. Sci.* **43**, 365-520 (1998).
16. Inoue, A., Ohtera, K., Tsai, A. P. & Masumoto, T. Aluminum-based amorphous alloys with tensile strength above 980 MPa (100 kg / mm^2). *Jpn. J. Appl. Phys.* **27**, L479-L482 (1988).
17. Koster, U. & Herold, U. Crystallization of amorphous $Fe_{80}B_{20}$. *Scripta Metall.* **12** (1978).
18. Wu, R. I., Wilde, G. & Perepezko, J. H. Glass formation and primary nanocrystallization in metallic glasses. *Mat. Sci. Eng. A* **A301**, 12-17 (2001).
19. Foley, J. C., Allen, D. R. & Perepezko, J. H. Analysis of nanocrystal development in Al-Y-Fe and Al-Sm glasses. *Scripta Mat.* **35**, 655-660 (1996).
20. Turnbull, D. Under What Conditions Can a Glass be Formed. *Contemp. Physics* **10** (1969).
21. Cao, H. et al. Computational thermodynamics to identify Zr-Ti-Ni-Cu-Al alloys with high glass forming ability. *Acta Mater.* **54** (2006).
22. Lu, Z. P. & Liu, C. T. A new glass-forming ability criterion for bulk metallic glasses. *Acta Mater.* **50**, 3501-3512 (2002).
23. Duan, R. G., Liang, K. M. & Gu, S. R. A new criterion fo rthe stability of glasses. *J. European Ceramic Soc.* **18** (1998).

24. *Liquid Metals Website, http://www.liquidmetal.com/.*
25. Perepezko, J. H. & Hebert, R. J. Amorphous Aluminum Alloys - Synthesis and Stability. *JOM* **54**, 34-39 (2002).
26. Davis, L. A., Ray, R., Chou, C. P. & O'Handley, R. C. Mechanical and thermal properties of Fe80B20 glass. *Scripta Metall.* **10** (1976).
27. Metglass. http://www.metglas.com/.
28. DeCristofaro, N. Amorphous Metals in Electric-Power Distribution Applications. *MRS Proceedings* **23** (1998).
29. Donovan, E. P., Spaepen, F., Turnbull, D., Poate, J. M. & Jacobson, D. C. Calorimetric studies of crystallization and relaxation of amorphous Si and Ge prepared by ion implantation. *J. Appl. Phys.* **57** (1985).
30. Chen, L. C. & Spaepen, F. Calorimetric evidence for the micro-quasicrystalline structure 'amorphous' Al/transition metal alloys. *Nature* **336**, 366-368 (1988).
31. Perepezko, J. H., Hebert, R. J., Wu, R. I. & Wilde, G. Primary crystallization in amorphous Al-based alloys. *J. Non-Cryst. Sol.* **317**, 52-61 (2003).
32. Perepezko, J. H. et al. Nanocrystallization reactions in amorphous aluminum alloys. *Mat. Trans.* **44**, 1982 - 1992 (2003).
33. Perepezko, J. H. et al. in *Supercooled Liquids, Glass Transition, and Bulk Metallic Glasses* (eds. Egami, T., Greer, A. L., Inoue, A. & Ranganathan, S.) CC10.3.1-CC10.3.6 (Materials Research Society, Boston, 2002).
34. He, Y., Poon, S. J. & Shiflet, G. J. Synthesis and properties of metallic glasses that contain aluminum. *Science* **241**, 1640-1642 (1988).
35. N. P. Kovaleno, Y. P. Krasny & Krey, U. *Physics of Amorphous Metals* (Wiley-VCH, Berlin, Germany, 2001).
36. Ossi, P. M. *Disordered Materials; An Introduction* (Springer-Verlag, Heidelberg, Germany, 2003).
37. Inoue, A., Ohtera, K., Tsai, A. P., Kimura, H. & Masumoto, T. Glass transition behavior of Al-Y-Ni and Al-Ce-Ni amorphous alloys. *Jpn. J. Appl. Phys.* **27**, L1579-L1582 (1988).
38. Greer, A. L. Metallic Glasses. *Science* **267**, 1947-1953 (1995).
39. Bordeaux, F., Yavari, A. R. & Desre, P. Formation of amorphous phase by solid state reaction in elemental composites prepared by cold rolling. *Mater. Sci. Eng.* **97**, 129-132 (1988).
40. Stratton, W. G., Hamann, J., Perepezko, J. H. & Voyles, P. M. Aluminum nanoscale order in amorphous $Al_{92}Sm_8$ measured by fluctuation electron microscopy. *Appl. Phys. Lett.* **86** (2005).
41. Eckert, J., Schultz, L. & Urban, K. Synthesis of Ni-Ti alloys by mechanical alloying - formation of amorphous phases and extended solid-solutions. (1991).
42. Nakazato, K., Kawamura, Y., Tsai, A. P. & Inoue, A. On the growth of nanocrystalline grains in an aluminum-based amorphous alloy. *Appl. Phys. Lett.* **63**, 2644-2646 (1993).
43. Das, S. K., Perepezko, J. H., Wu, R. I. & Wilde, G. *Mater. Sci. Eng. A* **304** (2001).
44. Kelton, K. F. A new model for nucleation in bulk metallic glasses. *Phil. Mag. Lett.* **77**, 337-343 (1998).
45. Xing, L. Q., Mukhopadhyay, A., Buhro, W. E. & Kelton, K. F. Improved Al-Y-Fe glass formation by microalloying with Ti. *Phil. Mag. Lett.* **84**, 293-302 (2004).

46. Sadoc, A. et al. Local order and nanostructure induced by microalloying in Al-Y-Fe amorphous alloys. *J. Non-Cryst. Sol.* **353** (2007).
47. Zhang, Y., Warren, P. J. & Cerezo, A. Effect of Cu addition on nanocrystallisation of Al-Ni-Sm amorphous alloy. *Mat. Sci. Eng. A* **A327**, 109-115 (2002).
48. Hong, S. J., Warren, P. J. & Chun, B. S. Nanocrystallization behaviour of Al-Y-Ni with Cu additions. *Mat. Sci. Eng. A* **A304-306**, 362-366 (2001).
49. Cusack, N. *The Physics of Structurally Disordered Matter* (IOP Publishing Ltd, Bristol, England, 1987).
50. Kovaleno, N. P., Krasny, Y. P. & Krey, U. *Physics of Amorphous Metals* (Wiley-VCH, Berlin, 2001).
51. Waseda, Y. & Matsubara, E. Structural investigation of amorphous and quasicrystalline Al-based alloys by the anomalous x-ray scattering (AXS) method. *Sci. Rep. Res. Inst. Tohoku Univ. A* **35**, 48-64 (1990).
52. Matsubara, E. et al. X-ray diffraction study of amorphous $Al_{77.5}Mn_{22.5}$ and $Al_{56}Si_{30}Mn_{14}$ alloys. *J. Mat. Sci.* **23** (1988).
53. Matsubara, E. et al. Structural study of $Zr_{60}Al_{15}Ni_{25}$ Amorphous Alloys with a Wide Supercooled Liquid Region by the Anomalous X-ray Scattering (AXS) Method. *Mat. Trans. JIM* **33**, 873-878 (1992).
54. Matsubara, E., Waseda, Y., Inoue, A., Ohtera, H. & Masumoto, T. Anomalous x-ray scattering on amorphous $Al_{87}Y_8Ni_5$ and $Al_{90}Y_{10}$ alloys. *Z. Naturforsch.* **44a**, 814-820 (1989).
55. Miracle, D. B. & Senkov, O. N. Topological criterion for metallic glass formation. *Mat. Sci. Eng. A* **347**, 50-58 (2003).
56. Hsieh, H. Y., Egami, T., He, Y., Poon, S. J. & Shiflet, G. J. Short range ordering in amorphous $Al_{90}Fe_xCe_{10-x}$. *J. Non-Cryst. Sol.* **135**, 248-254 (1991).
57. Miracle, D. B. & Senkov, O. N. in *Proc. 4th Pacific Rim International Conference on Advanced Materials and Processing* (eds. Hanada, S. & Masahashi, N.) 2893-2896 (JIM, Tokyo, Japan, 2001).
58. Holloway, K., Moine, P., Delage, J. & Sinclair, R. Structure of an amorphous Ti-Si alloy formed by thermal-reaction. *J. Non-Cryst. Sol.* **134** (1991).
59. Hirotsu, Y., Matsubara, E., Hara, N. & Ohkubo, T. Structure analysis of amorphous alloys by modern electron diffraction techniques. *Nanostructured Materials* **8** (1997).
60. Fan, C. et al. Pair distribution function study and mechanical behavior of as-cast and structurally relaxed Zr-based bulk metallic glasses. *Appl. Phys. Lett.* **89** (2006).
61. Kramer, E. J. & Sordelet, D. J. Polymorphism in the short-range order of Zr70Pd30 metallic glasses. *J. Non-Cryst. Sol.* **351** (2005).
62. Keen, D. A. & Mcgreevy, R. L. Structural modeling of glasses using reverse monte-carlo simulation. *Nature* **344** (1990).
63. Hirata, A., Hirotsu, Y. & Matsubara, E. Local atomic structures of amorphous Fe80B20 and Fe70Nb10B20 alloys studied by electron diffraction. (2005).
64. Cervinka, L. Modeling of medium-range order in metallic glasses: calculation of X-ray scattering in a $Ti_{61}Cu_{16}Ni_{23}$ glass. *J. Non-Cryst. Sol.* **156-158**, 94-97 (1993).
65. Treacy, M. M. J. When structural noise is the signal: Speckle statistics in fluctuation electron microscopy. *Ultramicroscopy* **107** (2007).

66. Voyles, P. M., Gibson, J. M. & Treacy, M. M. J. Fluctuation microscopy: a probe atomic correlations in disordered materials. *J. Electron Microsc.* **49**, 259-266 (2000).
67. Voyles, P. M. & Muller, D. A. Fluctuation microscopy in the STEM. *Ultramicroscopy* **93**, 147-159 (2002).
68. Nakhmanson, S. M., Voyles, P. M., Mousseau, N., Barkema, G. T. & Drabold, D. A. Realistic models of paracrystalline silicon. *Phys. Rev. B* **63**, 235207 (2001).
69. Fortner, J. & Lannin, J. S. *Phys. Rev. B* **37**, 10154 (1988).
70. Falk, M. L. Molecular-dynamics study of ductile and brittle fracture in model noncrystalline solids. *Phys. Rev. B* **60**, 7062-7070 (1999).
71. Hufnagel, T. C., Fan, C., Ott, R. T., Li, J. & Brennan, S. Controlling shear band behavior in metallic glass through microstructural design. *Intermetallics* **10**, 1163-1166 (2002).
72. Treacy, M. M. J., Gibson, J. M. & Keblinski, P. J. Paracrystallites found in evaporated amorphous tetrahedral semiconductors. *J. Non-Cryst. Sol.* **231**, 99-110 (1998).
73. Voyles, P. M. & Abelson, J. R. Medium-range order in amorphous silicon measured by fluctuation electron microscopy. *Solar Energy Materials and Solar Cells* **78**, 85-113 (2003).
74. Treacy, M. M. J. & Gibson, J. M. Variable coherence microscopy: a rich source of structural information from disordered systems. *Acta Cryst. A* **52**, 212-220 (1996).
75. Voyles, P. M., Gerbi, J. E., Treacy, M. M. J., Gibson, J. M. & Abelson, J. R. Increased medium-range order in amorphous silicon with increased substrate temperature. *J. Non-Cryst. Sol.* **293-295**, 45-52 (2001).
76. Ho, M.-Y. et al. Morphology and crystallization kinetics in HfO_2 thin films grown by atomic layer deposition. *J. Appl. Phys.* **93**, 1477-1481 (2003).
77. Chen, X. et al. Fluctuation Mricoscopy Studies of Aluminum Oxides Exposed to Cl Ions. *Mat. Res. Symp. Pro.* **738** (2002).
78. Chen, X., Sullivan, J., Friedman, T. & Gibson, J. M. Fluctuation microscopy studies of medium-range ordering in amorphous diamond-like carbon films. *Appl. Phys. Lett.* **84**, 2823 (2004).
79. Li, J., Gu, X. & Hufnagel, T. C. Using Fluctuation Microscopy to Characterize Structural Order in Metallic Glasses. *Microsc. Microanal.* **9**, 509 (2003).
80. Gibson, J. M., Treacy, M. M. J. & Voyles, P. M. Atom pair persistence in disordered materials from fluctuation microscopy. *Ultramicroscopy* **83**, 169-178 (2000).
81. Khare, S. V., Nakhmanson, S. M., Voyles, P. M., Keblinski, P. & Abelson, J. R. Evidence from atomistic simulations of fluctuation electron microscopy for preferred local orientations in amorphous silicon. *Appl. Phys. Lett.* **85**, 745-747 (2004).
82. Reimer, L. *Transmission Electron Microscopy; Physics of Image Formation and Microanalysis* (ed. Lotsch, H.) (Springer-Verlag, Berlin, 1997).
83. Kirkland, E. J. *Advanced Computing in Electron Microscopy* (Plenum Press, New York, NY, 1998).
84. Stratton, W. G. & Voyles, P. M. Comparison of fluctuation electron microscopy theories and experimental methods. *J. Phys: Cond. Mat.* **19** (2007).
85. Dash, R. K., Voyles, P. M., Gibson, J. M., Treacy, M. M. J. & Keblinski, P. A quantitative measure of medium-range order in amorphous materials from transmission electron micrographs. *J. Phys: Cond. Mat.* **15** (2003).

86. Stratton, W. G., Hamann, J., Perepezko, J. H. & Voyles, P. M. Electron beam induced crystallization of amorphous Al-based alloys in the TEM. *Intermetallics* **14** (2006).
87. Stratton, W. G. & Voyles, P. M. A phenomenological theory of fluctuation electron microscopy for a nanocrystal / amorphous composite. *Ultramicroscopy* **accepted for publication** (2007).
88. Treacy, M. M. J., Voyles, P. M. & Gibson, J. M. Schläfli cluster topological analysis of medium range order in paracrystalline amorphous semiconductor models. *J. Non-Cryst. Sol.* **266**, 150-155 (2000).
89. Cheng, J.-Y., Gibson, J. M., Baldo, P. M. & Kestel, B. J. Quantitative analysis of annealing-induced structure disordering in ion-implanted amorphous silicon. *J. Vac. Sci. Tech. A* **20**, 1855-1859 (2002).
90. Gerbi, J. E., Voyles, P. M., Treacy, M. M. J., Gibson, J. M. & Abelson, J. R. Control of medium-range order in amorphous silicon via ion and neutral bombardment. *Appl. Phys. Lett.* **82**, 3665-3667 (2003).
91. Li, J., Gu, X. & Hufnagel, T. C. Using fluctuation microscopy to characterize structural order in metallic glass. *Microsc. Microanal.* **9**, 509 (2003).
92. Voyles, P. M., Gerbi, J. E., Treacy, M. M. J., Gibson, J. M. & Abelson, J. R. Absence of an abrupt phase change from polycrystalline to amorphous in silicon with deposition temperature. *Phys. Rev. Lett.* **86**, 5514-5517 (2001).
93. Voyles, P. M., Treacy, M. M. J. & Gibson, J. M. in *New Methods, Mechanisms, and Models of Vapor Deposition* (eds. Wadley, H. N. G., Gilmer, G. & Barker, W.) 47-52 (Materials Research Society, 2000).
94. Voyles, P. M. et al. Structure and physical properties of paracrystalline atomistic models of amorphous silicon. *J. Appl. Phys.* **90**, 4437-4451 (2001).
95. Kwon, M. H. et al. Nanometer-scale order in amorphous $Ge_2Sb_2Te_5$ analyzed by fluctuation electron microscopy. *Appl. Phys. Lett.* **90**, 021923 (2007).
96. Howie, A. & Basinski, Z. S. Approximations of the Dynamical Theory of Diffraction Contrast. *Phil. Mag.* **17** (1967).
97. Treacy, M. M. J. & Gibson, J. M. Coherence and multiple scattering in "Z-contrast" images. *Ultramicroscopy* **52**, 31-53 (1993).
98. Voyles, P. M. in *Physics* (University of Illinois at Urbana-Champaign, Urbana-Champaign, 2001).
99. Taylor, J. R. *An introduction to error analysis, the study of uncertainties in physical measurements* (University Science Books, Sausalito, CA, 1997).
100. Freeman, L. A., Howie, A. & Treacy, M. M. J. Bright field and hollow cone dark field electron microscopy of palladium catalysts. *J. of Microscopy* **111**, 165-178 (1977).
101. Voyles, P. M., Treacy, M. M. J., Gibson, J. M., Jin, H.-C. & Abelson, J. R. in *Advances in Materials Problem Solving with the Electron Microscope* (eds. Bentley, J., Dahmen, U., Allen, C. & Petrov, I.) 155-160 (Materials Research Society, 1999).
102. Freeman, L. A., Howie, A., Mistry, A. B. & Gaskell, P. H. *The Structure of Non-Crystalline Materials* (ed. Gaskell, P. H.) (Taylor and Francis, London, 1976).
103. Kanter, H. Electron Mean Free Path near 2keV in Aluminum. *Phys. Rev. B* **1** (1970).
104. Barrett, H. H. & Myers, K. J. *Foundations of Image Science* (John Wiley and Sons, Hoboken, NJ, 2004).

105. Zuo, J. M. Electron detection characteristics of slow-scan CCD camera. *Ultramicroscopy* **66** (1996).
106. WaveMetrics. (Lake Oswego, OR, 1988-2004).
107. Tegart, W. J. M. *Electrolytic and Chemical Polishing of Metals in Research and Industry* (London Pergamon Press LTD, London, 1956).
108. Gangopadhyay, A. K., Croat, T. K. & Kelton, K. F. The effect of phase separation on the subsequent crystallization in $Al_{88}Gd_6La_2Ni_4$. *Acta Mater.* **48**, 4035-4043 (2000).
109. Wang, Y. B. et al. Evidence of phase separation correlated with nanocrystallization in $Al_{85}Ni_5Y_6Fe_2Co_2$ metallic glass. *Scripta Mat.* **55**, 469-472 (2006).
110. Geankopolis, C. J. *Transport Process and Unit Operations* (Englewood Cliffs, New Jersey, 1993).
111. Neeley, H. H. & Bauer, W. Electron-irradiation damage-rate measurments in aluminum. *Phys. Rev.* **149** (1966).
112. Hobbs, L. W. *Introduction to Analytical Electron Microscopy* (eds. Hren, J. J., Goldstein, J. I. & Joy, D. C.) (Plenum Press, New York, 1979).
113. Cohen, M. H. & Turnbull, D. *J. Chem. Phys* **31**, 1164 (1959).
114. Das, S. K., Perepezko, J. H., Wu, R. I. & Wilde, G. Undercooling and glass formation in Al-based alloys. *Mat. Sci. Eng. A* **A304-306**, 159-165 (2001).
115. Gibson, J. M. & Treacy, M. M. J. Diminished medium-range order observed in annealed amorphous germanium. *Phys. Rev. Lett.* **78**, 1074-1077 (1997).
116. Kelton, K. F. et al. Mechanisms for nanocrystal formation in metallic glass. *J. Non-Cryst. Sol.* **317**, 71-77 (2003).
117. Hebert, R. in *Materials Science and Engineering* (University of Wisconsin, Madison, WI, 2003).
118. Voyles, P. M. et al. in *Amorphous and Heterogeneous Silicon Thin Films 2000* (eds. Branz, H. M., Collins, R. W., Guha, S., Okamoto, H. & Stutzman, M.) A2.4.1-A2.4.6 (Materials Research Society, 2000).
119. Kelton, K. F. (eds. Voyles, P. M. & Stratton, W. G.) (2007).
120. Wen, J. et al. Fluctuation electron microscopy of Al-based metallic glasses: effects of minor alloying addition and structural relaxation on medium-range structural homogeneity. *J. Phys: Cond. Mat.* **19** (2007).